FREE SURFACE FLOW FOCUSING

IVO PETERS

Free surface flow focusing

Ivo R. Peters

Samenstelling promotiecommissie:

Prof. dr. G. van der Steenhoven (voorzitter)	Universiteit Twente
Prof. dr. D. Lohse (promotor)	Universiteit Twente
Dr. D. van der Meer (assistent-promotor)	Universiteit Twente
Prof. dr. A.P. Mosk	Universiteit Twente
Prof. dr. C. Clanet	LadHyX, France
Dr. R. Hagmeijer	Universiteit Twente
Prof. dr. J.J.W. van der Vegt	Universiteit Twente
Prof. dr. J.M. Gordillo	Universidad de Sevilla, Spain

The work in this thesis was carried out at the Physics of Fluids group of the Faculty of Science and Technology of the University of Twente. Financial support for this work was provided by the Dutch Organization for Scientific Research (NWO).

Nederlandse titel:
Convergerende stromingen en vrije oppervlakken

Publisher:
Ivo R. Peters, Physics of Fluids, University of Twente,
P.O. Box 217, 7500 AE Enschede, The Netherlands
pof.tnw.utwente.nl
ivo.r.peters@gmail.com

Cover design:
Ineke Koene

ISBN: 978-90-365-3376-8
DOI: 10.3990/1.9789036533768

FREE SURFACE FLOW FOCUSING

PROEFSCHRIFT

ter verkrijging van
de graad van doctor aan de Universiteit Twente,
op gezag van de rector magnificus,
Prof. dr. H. Brinksma,
volgens besluit van het College voor Promoties
in het openbaar te verdedigen
op vrijdag 29 juni 2012 om 16.45 uur

door

Ivo Remco Peters
geboren op 10 februari 1984
te Zevenaar

Dit proefschrift is goedgekeurd door de promotor:

Prof. dr. rer. nat. Detlef Lohse

en de assistent-promotor:

Dr. Devaraj van der Meer

Contents

1 Introduction

Many physical and chemical processes require a high energy density to run, or to keep running. An efficient way to achieve high energy densities is to start with a low energy density and to focus this into a small volume. According to legend the Greek scientist Archimedes used this principle during the siege of Syracuse, by focusing sunlight onto Roman ships in an attempt to set them to fire. In modern science, we are still trying to push the limits to which we can focus energy. A prime example is the development of nuclear fusion reactors, where the key ingredient is to confine a plasma at such a high energy density that nuclear fusion reactions take place. A possible way to achieve this, is to generate a focusing flow of plasma [1, 2]. The most extreme examples of flow focusing are actually happening naturally and are found many lightyears away, for example in the gravitational collapse of stars. These two examples are just a few of many others that require thorough understanding of focusing flows, which is the main subject of this thesis.

Incompressible flows that are dominated by inertia have the property that focusing of the flow results in an increase of the velocity. This property is very commonly applied, for example in the summer by children narrowing the end of a garden-hose to convert the rather weak stream that flows out usually, into a strong jet that reaches much further. To describe these flows, one has to recognize that the flow rate (volume per unit of time) in these flows remains constant. This constant flow rate condition then tells us that the smaller the area A trough which a fluid has to flow, the larger the velocity U becomes:

$$U \propto A^{-1}. \tag{1.1}$$

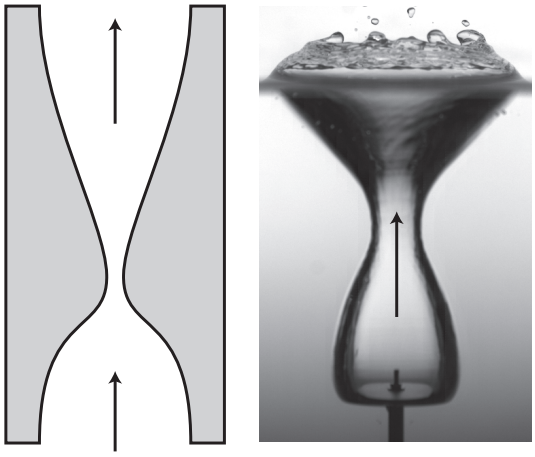

Figure 1.1: (*a*) a converging-diverging "de Laval" nozzle, where gas is accelerated to supersonic speeds. (*b*) after the impact of a disc on a water surface, a surface cavity is formed which acts as a liquid nozzle that accelerates the gas flow inside the cavity. The arrows in both images indicate the direction of the gas flow.

This principle is not only used by people trying to clean their car or motorcycle with a garden hose, but also in rocket engines where exhaust gasses are accelerated to speeds well above the speed of sound by a converging-diverging nozzle [3] as shown in Fig. 1.1(*a*). In the latter example however, one has to be aware that the speeds become too high for Eq. (1.1) to hold due to compressibility*.

In the examples mentioned above, a fluid flow is focused by means of a solid nozzle, that decreases in surface area downstream. In the case of a gas stream however, it is also possible to create a similar focusing nozzle from a liquid. Fig. 1.1(*b*) shows that such a nozzle is formed naturally after the impact of a solid on a liquid surface, where hydrostatic pressure is driving the gas flow, and the shape of the free surface is converging the flow through a small area. One becomes aware of the complexity of this system, when realizing that the liquid is not only influencing the gas stream, but the gas also starts to have its effect on the liquid: The result is a system with a subtle interplay between the dynamics of the gas and the liquid phase.

The free surface of a liquid can act as a boundary to focus a second fluid, but can also become the subject of flow focusing itself. A particular example is the pinch-off of an air bubble in a liquid, for example from an underwater nozzle [4–7] or after the impact of a liquid or a solid on a liquid surface [8–10]. In these cases, a void is

*Compressibility needs to be taken into account for $Ma > 0.3$, where Ma is the Mach number. After reaching $Ma = 1$ at the neck of the nozzle, the diverging exit leads to a further acceleration of the flow.

created inside a liquid, which shrinks due to capillary forces or hydrostatic pressure. Eventually, the void pinches off, where velocities diverge as the moment of pinch-off is approached, and the collapse becomes inertia-dominated. This divergence of velocities is the result of focusing the liquid flow towards a single point: the area A through which the liquid can escape approaches zero, which, according to Eq. (1.1) leads to $U \to \infty$.

A collapse driven by inertia is of interest for many applications because it can be a very violent phenomenon: The jets that are formed after the collapse of cavitation bubbles are responsible for the damage of ship propellers [11, 12], but can also be used to pulverize kidney stones [13, 14] or to remove dentine debris from root canals [15, 16]. The approach to a singularity is of great fundamental interest, especially because after recent experiments it was thought that, unlike the pinch-off of a liquid drop which is very well described by a universal law [17, 18], the pinch-off of an axisymmetric air bubble was non-universal [10, 19, 20]. These systems are different because the liquid drop pinch-off is governed by surface tension, where the bubble pinch-off is inertia-driven. The discussion was settled thereafter by showing that the axisymmetric pinch-off of an air bubble asymptotically approaches universality, but that this universal behavior often is hidden: something like self-similarity is there much earlier, but converges slowly to the real self-similar regime [21–23]. Thus, in the case of an axisymmetric pinch-off, the collapse can be described by scaling laws independent of the specific system, which means that the system has no memory of its initial state. A slight deviation from axisymmetry however, again changes the whole picture: it was found that even the smallest deviation from axisymmetry is remembered until the pinch-off [24–26]. A peculiar aspect of this memory of the initial state is that the absolute amplitude of the perturbation is remembered: the relative amplitude therefore grows towards the pinch-off, which results in the fact that eventually the perturbation dominates the shape of the free surface, and also determines the way the bubble pinches off.

In industrial applications flow focusing can be both your enemy or your friend, which we illustrate below with a few examples of both cases.

Situations where a free surface is driven to very small areas can sometimes be limiting in applications, like e.g. immersion lithography [27–29]. In immersion lithography a droplet is placed between a lens and a wafer to increase optical resolution, and this droplet stays attached to the lens as it moves over the wafer surface. Above a certain speed a sharp corner is formed at the tail of the droplet, which eventually leads to detachment of small droplets if the speed is increased further [30, 31]. To prevent the undesired deposition of small droplets on a wafer, one would like to avoid the formation of strongly curved interfaces. The first step for this would be to understand exactly *why* such a sharp corner is formed, and how the size and shape of the corner can be predicted.

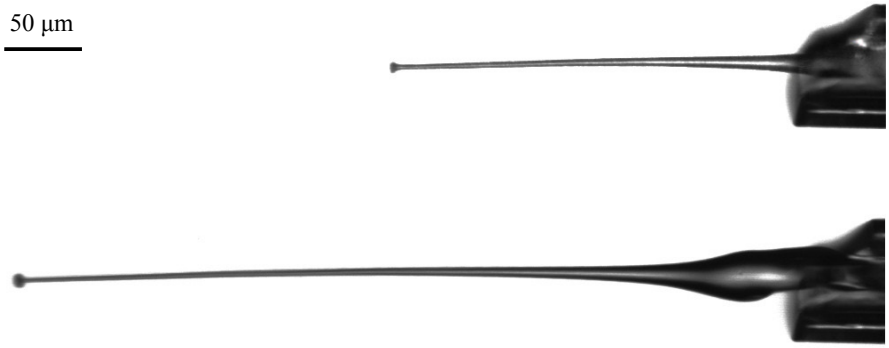

Figure 1.2: A jet with a typical diameter of 5 μm, traveling at a speed of 490 m/s. Time between the images is 500 ns. Courtesy of A. van der Bos, N. Oudalov, Y. Tagawa and C.W. Visser.

Strongly curved surfaces can however also be very useful in applications. For needle-free injectors, it is necessary to create a fast, thin jet [32]. Making use of the strongly curved meniscus that is naturally formed in a capillary, an ultrafast jet can be generated by shooting a laser in the liquid [33], see Fig. 1.2. In this case, the curved free surface acts as a focusing mechanism for the flow that was created by laser-induced cavitation [34, 35]. The formation of jets from a meniscus is also widely applied in ink-jet printing [36, 37], where the flow is driven by a piezo-electric element.

The objective of this thesis is to obtain a better understanding of the subjects described above. We will do so by investigating the topics described in the following chapters:

In Chapter 2 and 3 we investigate the role of air inside a collapsing cavity created by the impact of a round disc on a water surface. For this we apply three different methods to measure the air flow. In Chapter 2 we first experimentally determine the contour of the cavity during formation and collapse, from which we derive the cavity volume. Secondly, we introduce smoke particles inside the cavity which we illuminate using a laser sheet. Using particle image velocimetry (PIV) techniques, we determine the velocity of the air in the cavity. Both direct and indirect measurements agree very well and comparing our measurements with boundary integral (BI) simulations gives excellent agreement. We find that, just before pinch-off, compressibility of the air plays an important role in the dynamics of the cavity. In Chapter 3 we show that the air inside the cavity can even reach supersonic speeds.

In Chapter 4 we replace the circular disc that was used in Chapters 2 and 3 by one that has a non-axisymmetric shape similar to the petals of a flower. For small harmonic disturbances we closely follow how these disturbances grow and oscillate

during the collapse of the cavity. Our experimental results compare excellently to theoretical predictions, and ultimately, by solving the collapse of the cavity in (uncoupled) horizontal layers, were able to completely reconstruct the three-dimensional shape of a cavity that was created by the impact of a disc with a mode-20 harmonic disturbance. Increasing the amplitude of the perturbations, we depart from the linear theory, and find astonishing non-linear effects like the formation of sub-cavities and secondary jets.

In Chapter 5 we study the shape of a splash that is created in the very first instances of the impact of a circular disc. Using experimental observations and boundary integral simulations we show that the splash exhibits a self-similar behavior for any value of the Weber number, the dimensionless quantity that compares inertia with surface tension. We show that there exists a critical Weber number, above which small droplets are ejected from the rim of the splash, we show that a Rayleigh-Taylor instability is responsible for this transition.

In Chapter 6 we introduce a second liquid phase in our system by creating an experimental setup with three flowing components: Water, oil and air. By impacting the disc on a layer of oil that is floating on a deep layer of water, we obtain a deep understanding of the jet formation and the bulk flow after cavity collapse, which also applies for the single-liquid case. Specifically, we experimentally prove that the jet is created from the surface of the cavity, confirming earlier theoretical predictions [38]. By using a deep layer of oil and starting the disc at the oil-water interface, we create a two-fluid system without air, where the role of gravity has been greatly reduced. Pulling the disc down entrains a column of oil into the water; we show that the shape of the entrained oil becomes universal for high disc velocities.

In Chapter 7 we numerically investigate the formation of micro-jets created by laser induced cavitation. We perform boundary-integral simulations that closely reproduce experimentally obtained results. Using the insight obtained with numerical simulations, we develop a simple analytical model that accurately predicts the jet velocity dependence on the relevant parameters.

In Chapter 8 we investigate millimeter-sized silicone-oil drops that are sliding down an inclined surface. Drops that are sliding faster, tend to obtain a cornered shape at their tail. We experimentally show that the curvature at the corner increases exponentially with sliding speed. We explain this exponential increase by showing that the nanometric cut-off length, related to the classical viscous singularity at a moving contact line, plays an essential role in the selection of the curvature at the tail of a sliding drop.

We conclude in Chapter 9 with final remarks and an outlook for further research.

References

[1] A. Taylor, M. Dunne, S. Bennington, S. Ansell, I. Gardner, P. Norreys, T. Broome, D. Findlay, and R. Nelmes, *A route to the brightest possible neutron source?*, Science **315**, 1092 (2007).

[2] J. Nuckolls, L. Wood, A. Thiessen, and G. Zimmerman, *Laser Compression of Matter to Super-High Densities: Thermonuclear (CTR) Applications*, Nature **239**, 139–142 (1972).

[3] P. K. Kundu and I. M. Cohen, *Fluid Mechanics*, third edition (Elsevier) (2004).

[4] M. S. Longuet-Higgins, B. R. Kerman, and K. Lunde, *The release of air bubbles from an underwater nozzle*, J. Fluid Mech. **230**, 365–390 (1991).

[5] H. N. Oguz and A. Prosperetti, *Dynamics of bubble growth and detachment from a needle*, J. Fluid Mech. **257**, 111–145 (1993).

[6] J. M. Gordillo, *Axisymmetric bubble collapse in a quiescent liquid pool. I. Theory and numerical simulations*, Phys. Fluids **20**, 112103 (2008).

[7] R. Bolanos-Jimenez, A. Sevilla, C. Martinez-Bazan, and J. M. Gordillo, *Axisymmetric bubble collapse in a quiescent liquid pool. II. Experimental study*, Phys. Fluids **20**, 112104 (2008).

[8] E. G. Richardson, *The Impact of a Solid on a Liquid Surface*, Proc. Phys. Soc. **61**, 352–367 (1948).

[9] H. N. Oguz and A. Prosperetti, *Bubble entrainment by the impact of drops on liquid surfaces*, J. Fluid Mech. **219**, 143–179 (1990).

[10] R. Bergmann, D. van der Meer, M. Stijnman, M. Sandtke, A. Prosperetti, and D. Lohse, *Giant Bubble Pinch-Off*, Phys. Rev. Lett. **96**, 154505 (2006).

[11] S. S. Cook, *Erosion by Water-hammer*, Proc. R. Soc. A **119**, 481–488 (1928).

[12] a. Philipp and W. Lauterborn, *Cavitation erosion by single laser-produced bubbles*, J. Fluid Mech. **361**, 75–116 (1998).

[13] A. J. Coleman, J. E. Saunders, L. A. Crum, and M. Dyson, *Acoustic cavitation generated by an extracorporeal shockwave lithotripter*, Ultrasound in Med. & Biol. **13**, 69–76 (1987).

[14] Y. A. Pishchalnikov, O. A. Sapozhnikov, M. R. Bailey, J. C. Williams, R. O. Cleveland, T. Colonius, L. A. Crum, A. P. Evan, and J. A. McAteer, *Cavitation bubble cluster activity in the breakage of kidney stones by lithotripter shockwaves.*, J. Endourology **17**, 435–446 (2003).

[15] L. W. M. van der Sluis, M. Versluis, M. K. Wu, and P. R. Wesselink, *Passive ultrasonic irrigation of the root canal: a review of the literature.*, Int. Endod. J. **40**, 415–26 (2007).

[16] S. D. de Groot, B. Verhaagen, M. Versluis, M.-K. Wu, P. R. Wesselink, and L. W. M. van der Sluis, *Laser-activated irrigation within root canals: cleaning efficacy and flow visualization.*, Int. Endod. J. **42**, 1077–1083 (2009).

[17] X. D. Shi, M. P. Brenner, and S. R. Nagel, *A cascade of structure in a drop falling from a faucet.*, Science **265**, 219–22 (1994).

[18] J. Eggers, *Nonlinear dynamics and breakup of free-surface flows*, Rev. Mod. Phys. **69**, 865–930 (1997).

[19] J. C. Burton, R. Waldrep, and P. Taborek, *Scaling and Instabilities in Bubble Pinch-Off*, Phys. Rev. Lett. **94**, 184502 (2005).

[20] J. M. Gordillo, A. Sevilla, J. Rodríguez-Rodríguez, and C. Martínez-Bazán, *Axisymmetric Bubble Pinch-Off at High Reynolds Numbers*, Phys. Rev. Lett. **95**, 194501 (2005).

[21] J. Eggers, M. A. Fontelos, D. Leppinen, and J. H. Snoeijer, *Theory of the Collapsing Axisymmetric Cavity*, Phys. Rev. Lett. **98**, 94502 (2007).

[22] S. Gekle, J. H. Snoeijer, D. Lohse, and D. van der Meer, *Approach to universality in axisymmetric bubble pinch-off*, Phys. Rev. E **80**, 036305 (2009).

[23] J. M. Gordillo and M. Pérez-Saborid, *Axisymmetric breakup of bubbles at high Reynolds numbers*, J. Fluid Mech. **562**, 303–312 (2006).

[24] N. C. Keim, P. Mø ller, W. W. Zhang, and S. R. Nagel, *Breakup of Air Bubbles in Water: Memory and Breakdown of Cylindrical Symmetry*, Phys. Rev. Lett. **97**, 144503 (2006).

[25] L. E. Schmidt, N. C. Keim, W. W. Zhang, and S. R. Nagel, *Memory-encoding vibrations in a disconnecting air bubble*, Nature Phys. **5**, 343–346 (2009).

[26] K. S. Turitsyn, L. Lai, and W. W. Zhang, *Asymmetric Disconnection of an Underwater Air Bubble: Persistent Neck Vibrations Evolve into a Smooth Contact*, Phys. Rev. Lett. **103**, 124501 (2009).

[27] J. H. Burnett, S. G. Kaplan, E. L. Shirley, P. J. Tompkins, and J. E. Webb, "High-index materials for 193 nm immersion lithography", in *Proc. of SPIE*, volume 5754, 611–621 (SPIE) (2004).

[28] M. Riepen, F. Evangelista, and S. Donders, "Contact line dynamics in immersion lithography - dynamic contact angle analysis", in *Proceedings of the 1st European Conference on Microfluidics*, Figure 1 (Bologna) (2008).

[29] K. Winkels, I. Peters, F. Evangelista, M. Riepen, A. Daerr, L. Limat, and J. Snoeijer, *Receding contact lines: From sliding drops to immersion lithography*, Eur. Phys. J. Special Topics **192**, 195–205 (2011).

[30] T. Podgorski, J.-M. Flesselles, and L. Limat, *Corners, Cusps, and Pearls in Running Drops*, Phys. Rev. Lett. **87**, 036102 (2001).

[31] N. Le Grand, A. Daerr, and L. Limat, *Shape and motion of drops sliding down an inclined plane*, J. Fluid Mech. **541**, 293 (2005).

[32] S. Mitragotri, *Current status and future prospects of needle-free liquid jet injectors*, Nat. Rev. Drug Discov. **5**, 543–8 (2006).

[33] Y. Tagawa, N. Oudalov, C. W. Visser, I. R. Peters, D. van der Meer, C. Sun, A. Prosperetti, and D. Lohse, *Highly focused supersonic microjets* (2012), 1112.2517.

[34] C. E. Bell and J. A. Landt, *Laser-induced high-pressure shock waves in water*, Appl. Phys. Lett. **10**, 46–48 (1967).

[35] C. Sun, E. Can, R. Dijkink, D. Lohse, and A. Prosperetti, *Growth and collapse of a vapour bubble in a microtube: the role of thermal effects*, J. Fluid Mech. **632**, 5 (2009).

[36] B. Beulen, J. D. Jong, H. Reinten, M. V. D. Berg, H. Wijshoff, and R. van Dongen, *Flows on the nozzle plate of an inkjet printhead*, Exp. Fluids **42**, 217–224 (2007).

[37] A. U. Chen and O. A. Basaran, *A new method for significantly reducing drop radius without reducing nozzle radius in drop-on-demand drop production*, Phys. Fluids **14**, L1 (2002).

[38] S. Gekle, J. M. Gordillo, D. van der Meer, and D. Lohse, *High-Speed Jet Formation after Solid Object Impact*, Phys. Rev. Lett. **102**, 034502 (2009).

2

Air flow in a collapsing cavity *

We experimentally study the airflow in a collapsing cavity created by the impact of a circular disk on a water surface. We measure the air velocity in the collapsing neck in two ways: Directly, by means of employing particle image velocimetry of smoke injected into the cavity and indirectly, by determining the time rate of change of the volume of the cavity at pinch-off and deducing the air flow in the neck under the assumption that the air is incompressible. We compare our experiments to boundary integral simulations and show that close to the moment of pinch-off, compressibility of the air starts to play a crucial role in the behavior of the cavity. Finally, we measure how the air flow rate at pinch-off depends on the Froude number and explain the observed dependence using a theoretical model of the cavity collapse.

2.1 Introduction

The impact of a solid body on a water surface triggers a series of spectacular events: After a splash, if the impact speed is high enough, a surface cavity is formed which pinches off such that a bubble is entrained [1–3]. Right after pinch-off two strong thin jets are formed [4], one shooting upwards and one shooting downwards.

An aspect in the impact on liquids that has drawn particularly very little attention is the influence of the accompanying gas phase. When we take into account the inner gas in the detaching air bubble, we find a singularity in the velocity of the inner

*Ivo R. Peters, Stephan Gekle, Detlef Lohse, and Devaraj van der Meer, *Air flow in a collapsing cavity*, Preprint (2012)

gas. Assuming any finite flow rate for the gas, the velocity of the gas will diverge because the area that the gas has to flow through goes to zero. Nature has found a way to avoid a true singularity by letting compressibility limit the speed of the air, but nonetheless the air plays an important role in the final shape of the cavity just before pinch-off [5, 6], and can even reach supersonic speeds (see Chapter 3).

The main objective of this chapter is to understand what determines the gas flow rate in the case of an impacting disc and to obtain insight in the role of compressibility effects in the air. To this end we apply two different approaches: First we perform volume measurements to determine the flow rate based on continuity, and second we measure the air flow directly by seeding the air with smoke and laser sheet illumination. We compare and extend our experiments with numerical simulations, where we use one- and two-phase boundary integral simulations, sometimes coupled to compressible Euler equations [7], to determine the air flow, with and without taking the dynamics of the gas phase into account.

We have structured this chapter as follows: We first give a brief description of the experimental setup in Section 2.2. Section 2.3 explains the method of volume measurements, and the results are combined with numerical simulations. More specifically, we measure how the air flow rate at pinch-off depends on the Froude number and explain the observed dependence using a theoretical model of the cavity collapse. In Section 2.4 we perform a direct determination of the air flow velocity by seeding the air with smoke and illuminating with a laser sheet. Subsequently, we compare the results with the velocities that we determined using volume measurements. Finally, in Section 2.5 we discuss in detail when and how compressibility becomes important.

2.2 Experimental setup

The experimental setup consists of a water tank with a bottom area of 50 cm by 50 cm and 100 cm in height. A linear motor that is located below the tank pulls a disc through the water surface at a constant speed. This disc is connected to the linear motor by a thin rod. The events are recorded with a Photron SA1.1 high speed camera at frame rates up to to 20 kHz. Our main control parameter is the Froude number, which is defined as the square of the impact speed U_0, nondimensionalized by the disc radius R_0 and the gravitational acceleration g:

$$Fr = \frac{U_0^2}{gR_0} \tag{2.1}$$

Two snapshots of the experiment are shown in Fig. 2.1. The left image shows the situation right after the impact. where the cavity is being formed. A downward flow of air is required to fill in the space that is created by the downward moving disk and the expanding cavity. On the right a later stage in time is shown, some moments

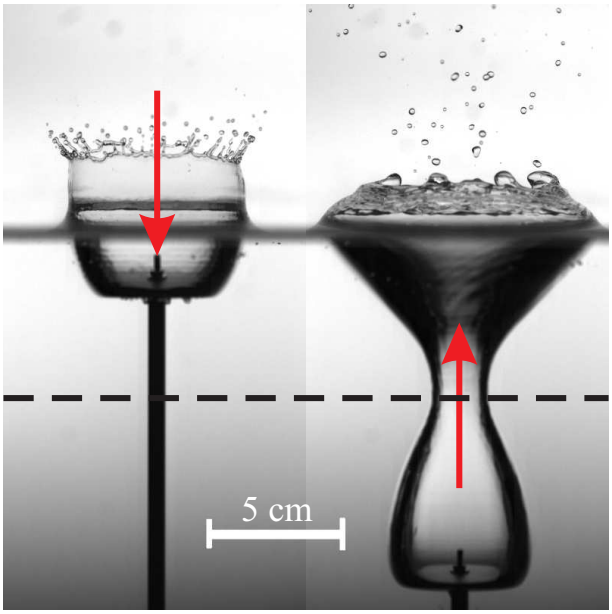

Figure 2.1: Two snapshots of an experiment in which a disk with a radius of 2 cm hits the water surface and moves down at a constant speed of 1 m/s. A surface cavity is created that subsequently collapses under the influence of hydrostatic pressure. Eventually, the cavity pinches off at the depth indicated by the dashed line, and a large air bubble is entrained. The red arrows indicate the direction of the air flow: On the left, volume is being created, resulting in a downward air flow. On the right the bubble volume below the pinch-off depth is decreasing, and therefore air is pushed upwards.

before the pinch-off. Here, there is a competition between the downward moving disc and the expanding part of the cavity on the one hand, and the collapsing part, i.e., the region above the maximum, on the other. The former tends to increase the cavity volume below the pinch-off depth (dashed line), whereas the latter decreases it. We always observe that close to pinch-off, the violent collapse is dominant and the bubble volume below the pinch-off point decreases, pushing air out through the neck. As the neck becomes thinner towards the moment of pinch-off, the gas speed increases rapidly. The remaining part of this chapter is devoted to measuring this air flow and comparing with numerical simulations.

2.3 Geometric approach

The first way in which we will quantify the air flow through the neck of the cavity is an indirect one: We will measure the time evolution of the volume of the cavity below the pinch-off point and calculate its first derivative with respect to time. This will be identified with the air flow rate through the neck. This involves the following assumptions: (i) The air flow is incompressible, (ii) the air flow profile is one-dimensional (i.e., a plug flow) and only directed in the vertical direction, and (iii) the cavity shape is axisymmetric. The first assumption is only violated close to the moment of pinch-off, when the air speed diverges. Compressibility effects at this stage are investigated in Chapter 3 and its effects will be discussed in section 2.5. We will justify the second assumption partially by visualizing the air flow inside the cavity and measuring the velocity directly; in addition it is known from two-fluid boundary-integral simulations that the flow profile is very close to one dimensional [7]. The third assumption only breaks down in the neck-region very close to pinch-off because very small disturbances are remembered during the collapse (see Chapter 4 and Refs. [8–13]). Here, this effect is only relevant locally on a very small scale and can therefore be neglected on the large scale where we measure the volume.

2.3.1 Cavity volume

We measure the volume of the cavity below the pinch-off depth as illustrated in Fig. 2.2: By tracing the contour for every frame in a movie and invoking axisymmetry we are able to determine the volume of the bubble below the pinch-off depth as a function of time. One such a measurement for a disk with radius 20 mm and impact speed of 1 m/s is shown in Fig. 2.3. In the beginning ($t \lesssim 0.022$ s) the volume is increasing (positive slope), which means that the air at the pinch-off depth is flowing downwards. At the maximum ($t \approx 0.022$ s) the flux through the pinch-off depth is zero, indicating a local stagnation of the flow at this depth. We will study this stagnation point later, in section 2.5. After this maximum the volume starts

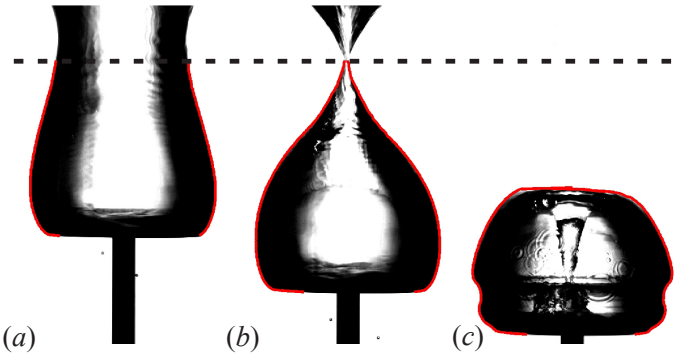

Figure 2.2: (a) The volume of the cavity below the pinch-off depth (dashed line) is determined by tracing the boundary (red line) and assuming symmetry around the central axis. (b) The volume decreases as the neck becomes thinner until the cavity closes. (c) After pinch-off a downward jet enters into the entrapped bubble, and the bubble shows volume-oscillations and cavity ripples.

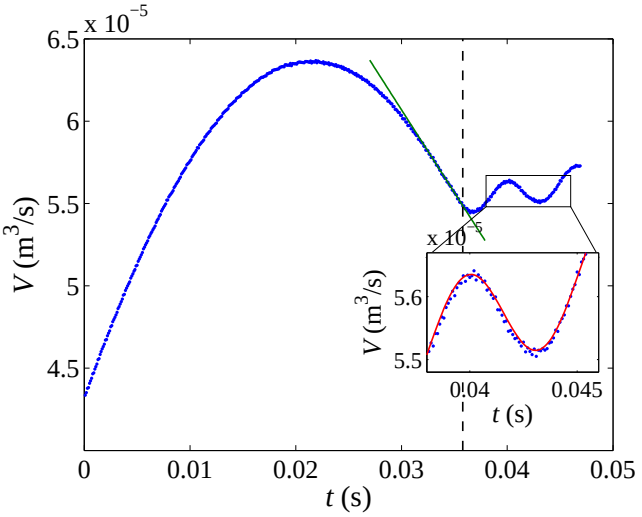

Figure 2.3: Volume below the pinch-off depth as a function of time (blue dots), determined from an experiment with $Fr = 5.1$. The vertical dashed line indicates the moment of pinch-off. Close to pinch-off the volume decrease is well approximated by a linear fit (green line), after pinch-off the bubble oscillates with its resonance frequency (red line: fit with sine function). The steady growth in volume after the pinch-off is caused by the jet entering the bubble.

to decrease and the flow is directed upwards. This continues until the moment of pinch-off which is indicated by the vertical dashed line in Fig. 2.3. A linear fit (green line) reveals that the flow rate is approximately constant towards the pinch-off moment. More precisely, the linear fit is the time rate of change of the cavity volume at pinch-off, which is equal to minus the maximum value of volume-based flow rate, $\Phi_V \equiv -dV/dt$, under the assumption of incompressibility of the air. We will use this maximum flow rate Φ_V to compare the flow rates through the neck at different Froude numbers.

After the pinch-off there is a clear oscillation of the volume together with a slow apparent growth of the bubble. The growth is caused by the liquid jet that is entering the bubble (Fig. 2.2c), as the amount of air is fixed after the pinch-off. Since our focus is on the behavior before pinch-off, we chose not to correct the bubble volume by subtracting this jet volume. Also, making such a correction would be complicated by the fact that the jet is imaged through the refracting, curved interface of the air bubble. Nevertheless we determined the frequency of the oscillation by fitting a sine function (red line) after correcting for the slightly positive slope. For the conditions of Fig. 2.3 the measured frequency is 143 Hz.

We compare this result with the resonance –or Minnaert– frequency f of a spherical bubble in water [14]: $f = 3.26/r$ where r is the bubble radius (in meters) and the value of 3.26 m/s is based on the material properties of water. Taking the bubble volume at pinch-off, which equals $5.49 \cdot 10^{-5}$ m^3 and adopting a spherical shape to calculate the radius, we find $f = 138$ Hz, which is very close to the frequency of the experimentally measured volume oscillation. Note that our bubble is far from spherical, but it was shown that deformation of bubbles only has a small influence on its resonance frequency [15]. The agreement of the volume oscillations after pinch-off with the Minnaert frequency was also noted by [16] for the impact of freely falling objects in water.

2.3.2 Air flow rate

A characteristic quantity concerning the gas dynamics in a collapsing cavity is the air flow rate, defined as the volume of air that is being displaced per unit time close to pinch-off. From Fig. 2.3 we infer that in approach of the pinch-off point this flow rate becomes constant and can be determined as the maximum slope of the volume as a function of time (green line, Fig. 2.3), i.e., the air flow rate through the neck equals the rate of change of the volume of the cavity below the pinch-off depth, of course under the assumption that the gas flow remains in the incompressible limit. This air flow rate $\Phi_V \equiv -dV/dt$ we subsequently non-dimensionalize dividing by the disk radius squared and the impact speed ($\Phi_V^* \equiv \Phi_V/(R_0^2 U_0)$), where the asterisk denotes a dimensionless value. We determined the flow rate for a number of different disk radii (ranging from 15 to 30 mm) and impact speeds (0.45-1.30 m/s), the results of

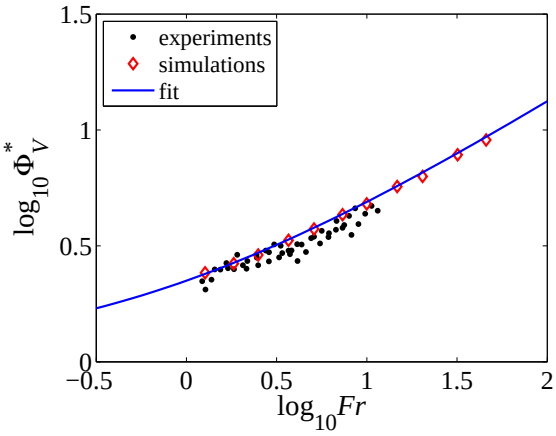

Figure 2.4: Volume based flow rate as a function of the Froude number in a double logarithmic plot. Both the experimental data (black dots) and the numerical data (red diamonds) correspond to the maximum value of Φ_V^*. The range of experimental data is limited to $Fr \approx 12$ by the appearance of a surface seal. The blue line represents the fit $\Phi_V^* = 1.23Fr^{1/2} + 1.01$.

which are shown in Fig. 2.4 where we plot the dimensionless flow rate Φ_V^* versus the Froude number Fr on a double-logarithmic scale (black dots). The experimental range is limited by the appearance of a surface seal at high impact speeds, where the crown splash is pulled inwards due to the air flow induced by the disc and closes the cavity at the surface. This surface seal usually has a significant influence on the cavity shape and dynamics [17] as well as the gas flow rate in the neck, so all of the experiments reported here are without surface seal. In the experimentally accessible regime we find an apparent power-law relation of $\Phi_V^* \propto Fr^{0.3}$. When we extend the experimental range by performing numerical simulations with our boundary integral code [7, 17], we find that the results do not lie on a straight line (Fig. 2.4, open red diamonds), which suggests that there does not exist a pure power-law.

An analytical argument - Using the assumption that the cavity expansion and collapse take place in horizontal non-interacting layers of fluid, an assumption that was successfully used in Bergmann *et al.* [17], we will now shed light onto the behavior of the air flow rate through the neck as a function of the Froude number. We will provide an approximate argument in this subsection, and present a more detailed account based on the model of Bergmann *et al.* [17] in the appendix. For convenience from hereon we will take the z to mean the depth below the undisturbed water surface, i.e., $z = 0$ at the latter and increases with depth.

The quantity that we aim to calculate is the time rate of change of the cavity

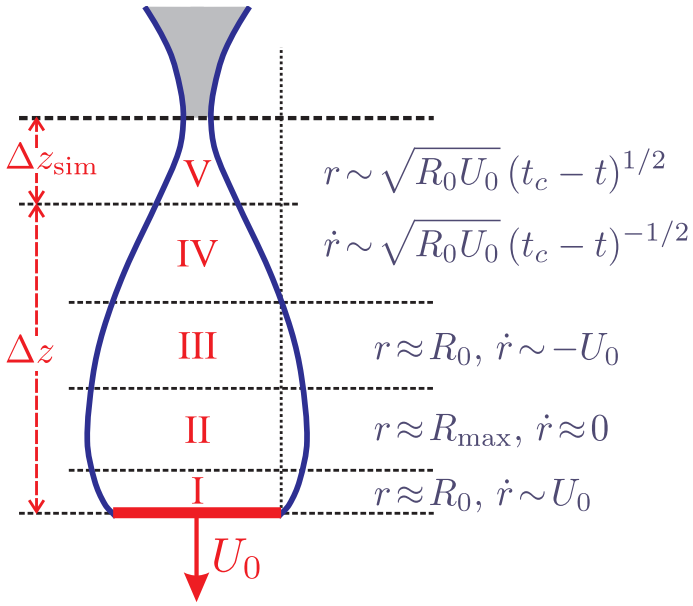

Figure 2.5: The partly collapsing partly expanding cavity close to the pinch-off moment can be divided in five different regions: In region I the cavity expands against hydrostatic pressure; region II is the hardly expanding/collapsing region around the maximum; in region III the hydrostatic pressure drives the collapse of the cavity, and in region IV/V continuity takes over as the driving mechanism behind the collapse. The difference between region IV and V is that the latter has a self-similar shape which is independent of the Froude number [18].

volume $\dot{V} = dV/dt$, i.e.,

$$\Phi_V \equiv -\frac{dV}{dt} = -\frac{d}{dt}\int_{z_c}^{z_{\rm disc}} \pi\,[r(z,t)]^2 dz\,, \tag{2.2}$$

where it is understood that the expression needs to be evaluated at the pinch-off time. Here, $r(z,t)$ is the cavity profile, $z_{\rm disc}(t)$ is the vertical position of the disc and z_c is the pinch-off depth. Using Leibniz's rule we obtain

$$\Phi_V = -\int_{z_c}^{z_{\rm disc}} 2\pi\, r(z,t)\,\dot{r}(z,t,)dz \;-\; \pi R_0^2 U_0\,, \tag{2.3}$$

where the last term is due to the downward moving disc and $\dot{r} \equiv \partial r/\partial t$ denotes the radial velocity of the cavity wall.

To approximate the integral in Eq. (2.3) we subdivide the expanding and collapsing cavity –at times close to the collapse– into the regions of Fig. 2.5: In region I, just above the disc, the cavity has a radius close to the disc radius, $r \approx R_0$, and is expanding against hydrostatic pressure with a horizontal velocity that is proportional to the disc velocity $\dot{r} \sim U_0$. The contribution of Region I to the integral of Eq. (2.3) can therefore be approximated as $\Phi_{V,\rm I} \sim -R_0 U_0 \Delta z_I$, where $\Delta z_{\rm I}$ is the height of region I. The second region is an approximately symmetric region, where $r \approx R_{max}$, the maximum cavity radius at pinch off, and the velocity is close to zero, $\dot{r} \approx 0$. For this reason, and also because of the symmetry above and below the vertical position of the maximum which contribute with sign change to the integral of Eq. (2.3), the contribution of region II is negligible, $\Phi_{V,\rm II} \approx 0$. In the third region the magnitudes of cavity radius and velocity are similar to those in region I, but the cavity is collapsing rather than expanding, i.e., $r \approx R_0$ and $\dot{r} \sim -U_0$, leading to $\Phi_{V,\rm III} \sim R_0 U_0 \Delta z_{\rm III}$. Incidentally, due to the asymmetry between regions I and III their respective contributions are not expected to cancel. The fact that $\Delta z_{\rm III} > \Delta z_{\rm I}$ leads to a positive contribution to the air flow rate. Finally, regions IV and V are the regions where the cavity collapses inertially, i.e., the cavity wall accelerates predominantly as a consequence of continuity

$$r\dot{r} = \text{constant} \sim R_0 U_0 \;\Rightarrow\; r \sim \sqrt{R_0 U_0 (t_c - t)}, \tag{2.4}$$

where t_c is the pinch-off time. The time derivative of Eq. (2.4) gives $\dot{r} \sim -\sqrt{R_0 U_0}(t_c - t)^{-1/2}$ such that $r\dot{r} \sim -R_0 U_0$, independent of z. This now leads to $\Phi_{V,\rm IV} \sim R_0 U_0 \Delta z_{\rm IV}$ and $\Phi_{V,\rm V} \sim R_0 U_0 \Delta z_{\rm V}$ respectively. Combining all of the above we can approximate Eq. (2.3) as

$$\begin{aligned} \Phi_V &= \Phi_{V,\rm I} + \Phi_{V,\rm II} + \Phi_{V,\rm III} + \Phi_{V,\rm IV} + \Phi_{V,\rm V} - \pi R_0^2 U_0 \\ &= R_0 U_0 (-A_{\rm I}\Delta z_{\rm I} + A_{\rm III}\Delta z_{\rm III} + A_{\rm IV}\Delta z_{\rm IV}) \\ &+ A_{\rm V} R_0 U_0 \Delta z_{\rm V} - \pi R_0^2 U_0\,, \end{aligned} \tag{2.5}$$

with A_{I}, A_{III}, A_{IV}, and A_{V} numerical constants.

The difference between region I to IV and region V lies in the way the vertical length scale scales with the impact speed, i.e., with the Froude number. As demonstrated in [19] and [17], the cavity as a whole, i.e., the pinch-off depth z_{pinch} and the depth of the disc at the moment of pinch-off z_{disc}, scale as $R_0 Fr^{1/2}$. So the same scaling can also be expected for the vertical length scales Δz_{I} to Δz_{IV} introduced above. Things are different for region V, close to the pinch off, where there exists a local self-similar coupling between the vertical and the radial cavity dimensions [2, 18, 20]. For this reason Δz_{V} is expected to be independent of the Froude number, i.e., $\Delta z_{\mathrm{V}} \sim R_0$. Inserting the scaling of the vertical length scales into Eq. (2.5) leads to the expected $R_0^2 U_0$-dependence in all terms and an additional $Fr^{1/2}$-dependence for the first three terms only

$$\Phi_V = R_0^2 U_0 \left[A\, Fr^{1/2} + B \right] \;\Rightarrow\; \Phi_V^* = A\, Fr^{1/2} + B\,, \tag{2.6}$$

with A and B numerical constants. To test this relation we extended the experiments of Fig. 2.4 by performing boundary integral numerical simulations in order to cover a wide range of Froude numbers [†]. The obtained results are added to Fig. 2.4 using red diamonds. There is a good agreement with the experimental data, and the non-constant slope is clearly visible. A fit to the simulation data confirms Eq. (2.6) and gives $A \approx 1.23$ and $B \approx 1.01$.

2.4 Flow visualization

In this Section we perform a direct determination of the air flow velocity by seeding the air with smoke and illuminating with a laser sheet, the results of which we will subsequently compare to the velocities that were determined indirectly and independently using volume measurements. We will first describe the method and results of the flow visualization that we used to measure the air flow inside the cavity. Before doing the impact experiment we fill the atmosphere above the water surface with small smoke particles. When subsequently the disk is moved down through the water surface, the smoke is dragged along, and fills the cavity created below the surface. We illuminate a thin sheet of the smoke using a 1500 mW diode laser line generator (Magnum II) and record the experiment at a recording rate up to 15 kHz by placing the high speed camera perpendicular to the laser sheet (Fig. 2.6). The smoke consists of small glycerine-based droplets (diameter $\sim 3\ \mu$m), produced by a commercially available smoke machine built for light effects in discotheques. A simple analysis shows that the particles are light enough to neglect all inertial effects at least in the

[†] The simulations in Fig. 2.4 are two-phase boundary integral simulations, where close to pinch off the compressibility of the gas is taken into account using the one-dimensional compressible Euler equations (briefly discussed in Section 2.5 as type (iii) simulations). More details about these simulations can be found in [7] and in Chapter 3.

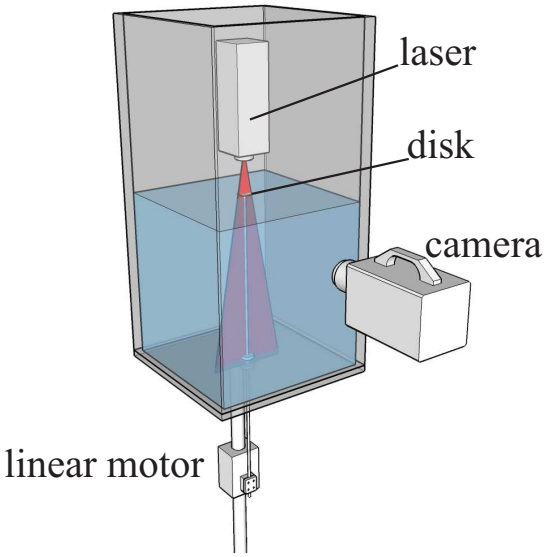

Figure 2.6: A schematic view of the setup. A laser sheet shines from above on the disk, illuminating the interior of the cavity after the disk has impacted the water surface. We insert smoke in the top part of the container and when the linear motor pulls the disk through the water surface at a constant speed, the smoke is entrained into the cavity.

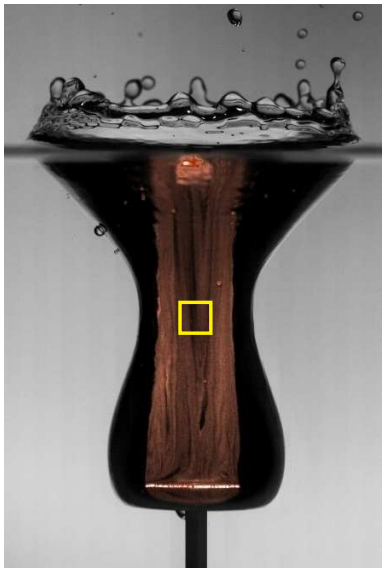

Figure 2.7: A snapshot of the cavity with an overlay of a recording of the illuminated smoke. The smoke particles are artificially colored orange in this figure. The size and position of correlation window is indicated by the yellow square.

range of accelerations that we can measure experimentally: At a velocity difference of 10 m/s the Reynolds number is ~ 2, meaning we can assume Stokes drag. Knowing the force on the particle as a function of the velocity difference and the mass of the particles, we can calculate the movement of the droplets in an accelerating flow. We find that the particles follow the flow up to 25 m/s with a velocity lag less than 2%.

Correlation technique - We determine the speed of the air in the neck by applying an image correlation velocimetry (ICV) technique [21]. ICV differs from Particle Image Velocimetry (PIV) in the sense that we do not resolve discrete particles in our images, but we correlate smoke patterns instead of smoke particles. Figure 2.7 shows the cavity with the illuminated smoke as an overlay, where the smoke is colored orange artificially for clarity. The actual measurements are done on a closer view of the cavity. The correlation is performed on a square correlation window, indicated by the yellow square. The width of the correlation window is 160 pixels, corresponding to 8.8 mm. In the latest stages we switch to a correlation window of 96 pixels (5.3 mm) wide, anticipating on the smaller neck radius. The measurements are insensitive to small changes in the shape, size or position of the correlation window. The size of the window is optimized for quality of the cross correlation.

Mainly due to reflections from and refraction at the free surface, there are struc-

tures visible in the correlation window that move slowly compared to the typical gas velocities that we want to measure. A correlation between two unprocessed images gives a strong correlation peak close to zero because these structures are dominating the image, and thereupon also the cross-correlation. Standard background subtraction is not able to remove these features since, because of their refractive and reflective nature they appear and disappear at unpredictable instances in time and are not stationary. Instead we use the difference between subsequent images, in the following way. We start with three images I_n, I_{n+1}, and I_{n+2}. After applying a low pass filter we create from these three images two new images by subtraction: $J_n = I_{n+1} - I_n$ and $J_{n+1} = I_{n+2} - I_{n+1}$. After this we apply a min-max filter [22] to both images, followed by the cross correlation of J_n and J_{n+1}. On the result of the correlation we apply a multiple peak detection to find the highest peak p_1 and the second-highest peak p_2. We determine the position of the highest peak with sub-pixel accuracy by a gaussian fitting routine.

A subtraction technique similar to the one that we use here has been used previously for double-frame PIV images [23], where it was found that if the displacement of the particles is too small between a pair of images, the displacement peak in the correlation is biased. This bias is related to the particle size in pixels and the displacement in pixels. In our case this length scale does not exist because we do not resolve separate smoke particles in our experimental setup. Instead of calculating the expected bias, we identify biased values by their departure from the global trend of the data (Fig. 2.8, inset). As a remedy for the bias, we artificially increase the displacement by skipping frames. The smaller the velocity, the larger the number of frames we skip. In addition to this we note that the bias is less pronounced compared to the case in [23] because we construct the image pair from three images in stead of two.

The biased data and other spurious data is removed by making an objective selection based on the peak-to-peak ratio of the correlation. This ratio is defined as the ratio between the two highest peaks in the correlation: $\lambda = p_1/p_2$. The inset of Figure 2.8 shows the effectiveness of this selection method. We set λ to values between 3.5 and 5.0, depending on the specific measurement, so that almost all spurious data is removed. Taking higher values for λ removes too much valid data points; lower values allow for too many biased data points.

In Fig. 2.8 we compare the air speed that we measured directly using smoke particles with the air velocity that we calculated indirectly using the change in volume of the cavity, as discussed in the previous Section. The air speeds are plotted versus the neck radius $R(t)$ at pinch-off depth instead of time; time increases from right to left in the Figure, i.e., towards smaller values of R. The blue line is obtained using a polynomial (smoothing) fit to the volume-time data of Fig 2.3, determining the flow rate $\Phi_V(t)$ from the time derivative of this fit [Eq. (2.2)], and finally dividing

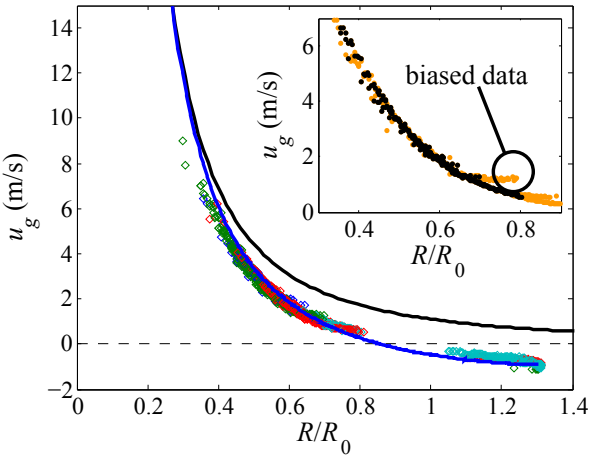

Figure 2.8: The vertical air velocity through the neck as a function of the neck radius R, measured in an experiment with $Fr = 5.1$ in three different ways: (i) Directly, using smoke particles (diamonds), (ii) Indirectly, using a smoothing polynomial fit to bubble volume of Fig. 2.3 (blue line) , and (iii) Indirectly, using a constant flow rate approximation, determined at pinch off (cf. Fig 2.3, black line). The different colors of the diamonds correspond to different numbers of frames that are skipped in the cross-correlation (see main text). The inset shows the same vertical velocity data measured using method (i) for two different values for the peak-to-peak ratio λ: For $\lambda > 1.5$ (orange dots) we find strongly biased data, which are eliminated using a higher threshold ($\lambda > 3.5$, black dots).

by $\pi R(t)^2$ to obtain the velocity. We find a very good agreement between the direct (smoke) and the indirect (volume) measurements.

Finally, the black line in Fig. 2.8 is obtained by setting the flow rate to a constant value, namely to that corresponding to the time derivative of the volume curve just before pinch off (the green line in Fig. 2.3). We observe that at early times (large R) there are large deviations from the other two datasets. This stands to reason, since at these times we are still far away from the pinch-off moment, and the gas flow rate in the neck has not yet become (approximately) constant. Close to pinch off however, for $R/R_0 \lesssim 0.4$, we find that the constant flow rate approximation and the smoothing fit both provide the same air speed.

2.5 The role of compressibility

The fact that the air flow rate becomes constant together with the surface area of the neck becoming vanishingly small suggests that the velocity in the neck diverges towards pinch off. However, as was mentioned in the introduction, a real singularity of the air flow velocity is prevented by compressibility effects. In a previous publication we presented a directly visible effect of the compressed gas flow, namely the upwards motion of the position of the minimum neck radius (Chapter 3). This upwards motion was seen both in experiments and in simulations that take into account the compressibility, and is absent in simulations that neglect compressibility. In the same paper we reported that, next to this upward motion of the neck, the extremely fast airflow affects the smoothness of the neck. Especially this last effect is important, since it is in contradiction with the assumptions in theoretical pinch-off models where the neck is assumed to be slender [18, 20].

The question that we intend to answer in the present Section is how the effects of compressibility show up in the measurement of the cavity volume and the air flow rate that can be deduced from it, as was presented in Section 2.3 of this work. More specifically we will investigate the position of the stagnation point of the flow in the cavity (see below) and the air flow rate towards the pinch-off moment. Following the method we used in Chapter 3, we will compare our experimental results with three different types of boundary integral simulations: (i) a single phase version, in which only the water phase is resolved, (ii) a two-phase version where both the liquid and the gas flow are resolved as incompressible inviscid media, and (iii) a compressible gas version where the compressibility of the gas phase is taken into account by substituting the incompressible axisymmetric gas phase equations by one-dimensional compressible Euler equations at that moment during the collapse when compressibility effects start to become significant. More details about the numerical method can be found in [7] and in Chapter 3.

Stagnation point - Just above the disc the air must move downwards at approxi-

mately the same speed as the disc, whereas simultaneously, towards closure, the air in the neck is moving upwards. This implies that somewhere in between there will be a stagnation point. We will estimate the location of this stagnation point as follows: The first step is to extend the analysis of Section 2.3, where we tracked the volume below the pinch-off depth in time, to any depth z below the pinch-off point. For every depth z this will provide us with a curve similar to that in Fig. 2.3 and by determining the time coordinate of the maximum we find the time t_{stag} at which the averaged [‡] flow rate ($\sim \dot{V}$) at that depth $z \equiv z_{\text{stag}}$ is zero. This point we then interpret as the location of the stagnation point $z_{\text{stag}}(t_{\text{stag}})$, which involves the assumption that close to the pinch-off moment the flow in the neck region becomes predominantly homogeneous and vertical. In Fig. 2.9 we plot the measured location of z_{stag} for three different realizations of an experiment with a radius of 2 cm and an impact speed of 1 m/s. A difference with the actual location of the stagnation point is therefore expected for high gas velocities (i.e., small neck radii). When we compare the experiments to a two-phase incompressible boundary integral simulation [type (ii)] (red line in Fig. 2.9, we find a considerable discrepancy between the two for small values of the neck radius R. If we however use the compressible version of the simulation [type (iii)], the agreement becomes much better (red line in Fig. 2.9, confirming the importance of compressibility in this limit. Note that experiments and both simulations do converge for larger values of R, where compressibility effects play no role.

The agreement is not perfect however, which can partly be traced back to the technical difficulty of obtaining reliable values for z_{stag} from the experiment (which reflects in the large spread between the three different realizations) and partly to the fact that its determination neglects compressibility in a subtle way: Although in the experimental data compressibility is of course necessarily reflected in the shape of the cavity, the method of obtaining the air flow rate from it (namely by determining the time rate of change of the cavity volume) neglects compressibility in the air phase.

Air flow rate - As explained in the introduction of this Section, we can compare the air flow rate in the neck in experiment and simulation directly, by comparing the experimental velocities (cf. Section 2.4) as was done in Chapter 3, but also indirectly, by using the volume analysis of Section 2.3 both in experiment and simulation. This second method, the results of which will be presented now, enables us to distinguish the effect the compressibility of the air has on the cavity wall (which is included in the analysis) from the pure compressibility of the flow (which is not included).

To do so it is convenient to from now on distinguish the true air flow rate from the derived air flow rate, i.e., the one obtained from the time rate of change of the cavity volume. In Fig. 2.10a we plot the non-dimensionalized experimental derived air flow

[‡] Averaged over the cross-sectional area of the cavity at that depth.

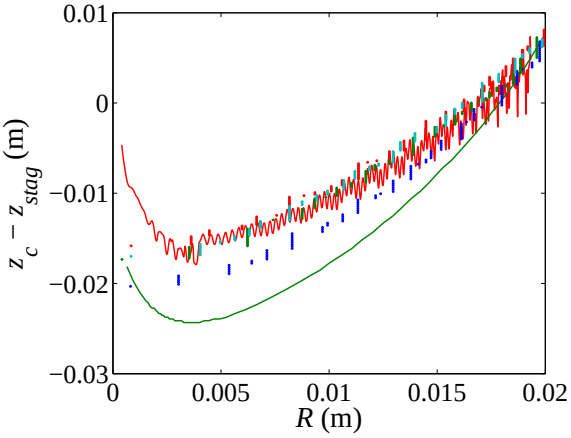

Figure 2.9: The location of the stagnation point z_{stag} with respect to that of the pinch-off point z_c as a function of the neck radius R. Note that when that the stagnation point lies below the pinch-off point $z_c - z_{\text{stag}}$ is negative. Time increases from right to left (decreasing R). The dots are experimental data, obtained by volume measurements of four different experiments, where each color corresponds to a different experiment. All experiments were performed with disk radius $R_0 = 2.0$ cm and impact speed $U_0 = 1.0$ m/s, i.e., $Fr = 5.1$. The green line is the result of a two-phase boundary integral simulation without taking compressibility into account [type (ii)]. The red line is obtained by a two-phase boundary integral simulation which includes a compressible gas phase [type (iii)].

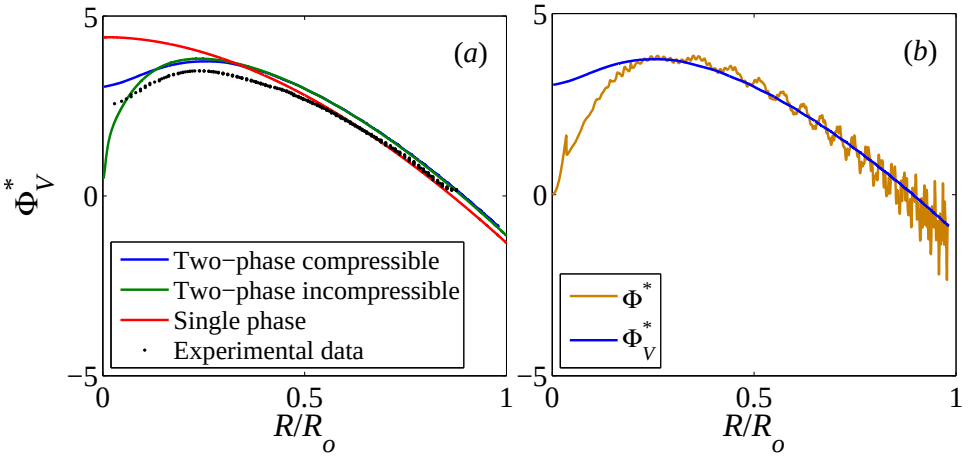

Figure 2.10: (a) The dimensionless derived air flow rate $\Phi_V^* = \Phi_V/(R_0^2 U_0)$ (from the time rate of change of the cavity volume) as a function of the dimensionless neck radius R/R_0 in an impact experiment with disc radius $R_0 = 2$ cm and impact speed $U_0 = 1$ m/s ($Fr = 5.1$). The black dots represent experimental data. The red line is obtained using a one-phase simulation [type(i)], which excludes the air phase. The green line is a two-phase boundary integral simulation without compressibility [type (ii)]. Finally, the blue line is the result of a two-phase boundary integral simulation which includes a compressible gas phase [type (iii)]. (b) Comparison of the dimensionless derived air flow rate Φ_V^* [blue line; the same curve as in (a)] and the true air flow rate Φ^*, both plotted versus R/R_0. The two curves diverge from each other below $R/R_0 \approx 0.2$.

rate in the neck,

$$\Phi_V^* \equiv \frac{\Phi_V}{R_0^2 U_0} \equiv -\frac{1}{R_0^2 U_0}\frac{dV}{dt}\,, \tag{2.7}$$

as a function of the dimensionless neck radius $R(t)/R_0$ (black dots), again for $Fr = 5.1$. Repeating the experiment results in an uncertainty in the magnitude of Φ_V^* (corresponding to the spread of the experimental data in Fig. 2.4), but the behavior as a function of time is always the same: The derived air flow rate in the neck reaches a maximum, and approaches a finite value towards the moment of pinch-off. We compare this result with those of the three different types of boundary integral simulations:

The one-phase code [type (i)] predicts a steadily increasing derived air flow rate, which seems to level off to a constant value towards pinch off ($R/R_0 \to 0$). This is the red line in Fig. 2.10(a).

The two-phase incompressible version [type (ii)] predicts a maximum at a location which is reasonably comparable to the experimental one, but after that decreases toward zero at the pinch-off moment (the green curve in Fig. 2.10(a)). Since both phases are incompressible, this stands to reason: The pressure in the cavity rises instantly because of the divergence of the air velocity u_g in the shrinking neck. This pressure decelerates the cavity wall, which in turn decreases the derived air flow rate, which should go to zero in the $R/R_0 \to 0$-limit: In the context of incompressible flow, a finite derived air flow rate would result in an infinite air velocity in the neck and consequently an infinite pressure within the cavity. Here it is good to note that for this two-phase incompressible code the derived and true air flow rates are actually identical, due to the incompressibility of the air phase.

The two-phase compressible simulation [type (iii)] also predicts a maximum for Φ_V^*, at a location similar to the two-phase incompressible code and the experiment, but then decreases to a finite value for $R/R_0 \to 0$, just like the experiment. Clearly, and in contrast with the other two versions of the simulation which behave poorly, the agreement with the experiments is qualitatively very good and quantitatively satisfactory. All three types of simulations and the experiments all converge for larger $R/R_0 \approx \mathcal{O}(1)$, which is expected since airflow effects (let alone compressibility of the air phase) are small or even negligible in that regime.

The final question that we want to address is the difference between the true air flow rate (which incorporates all compressibility effects) and the derived one (which only includes the effects of compressibility on the cavity wall). In experiment it is impossible to obtain the first quantity at the required precision, because its determination includes measurement errors in both air velocity u_g and neck radius R. The two-phase compressible simulation technique however does offer a way to look at this difference: In Fig. 2.10(b) we compare the derived air flow rate Φ_V^* (the same

curve as the blue one in Fig. 2.10(a)) to the true air flow rate Φ^* (green curve), which is calculated from $u_g(t)$ and $R(t)$ as

$$\Phi^* \equiv \frac{\Phi}{R_0^2 U_0} = \frac{1}{R_0^2 U_0} \frac{u_g(t)}{\pi R(t)^2}, \tag{2.8}$$

both as a function of the dimensionless cavity radius $R(t)/R_0$. Clearly the two curves coincide above $R/R_0 \approx 0.2$, but start to depart from one another below this value, indicating that here the compressibility of the air itself becomes significant, in good agreement with what we concluded from the previous plot (Fig. 2.10(a)). We observe that the true air flow rate goes to zero for $R/R_0 \to 0$ (and incidentally not quite unlike the two-phase incompressible curve (green) in Fig. 2.10(a)). This is of course what should happen, since the gas velocity in the neck needs to remain finite at all times. The difference between the two curves is the rate at which the gas in the cavity is compressed.

2.6 Conclusions

We have measured the air flow inside the neck of a collapsing cavity that was created by the impact of a circular disc on a water surface. More specifically we have performed and compared two types of experiments: First we did indirect measurements, using the time rate of change of the cavity volume as a measure for the air flow rate in the neck, thereby neglecting compressibility of the air inside the cavity. Secondly we performed direct measurements of the velocity in the neck of the cavity using image correlation velocimetry. Numerical boundary integral simulations of three different types have been used to evaluate and discuss our experimental findings.

For the complete experimentally available range of Froude numbers we showed that there is a very good agreement between the indirectly measured air flow rate and the boundary integral simulations. With the simulations we were able to extend the range of experimentally attainable Froude numbers, which revealed that the air flow rate is not a pure power-law of the Froude number. We formulated an analytical argument revealing that the dimensionless air flow rate should scale as $AFr^{1/2} + B$. Such a scaling compares well with experiments and simulations for $A \approx 1.23$ and $B \approx 1.01$.

By performing careful image correlation velocimetry experiments with a smoke-filled cavity we have been able to directly measure the air flow for relatively low air speeds, corresponding to $R/R_0 \geq 0.3$. In this region we found excellent agreement with the gas velocities that we calculated from the indirect measurements of the air flow rate and the neck radius $R(t)$.

Due to the very high air speed close to the moment of pinch-off ($R/R_0 \leq 0.2$) compressibility of the air can not be neglected anymore. We have demonstrated this

by comparing experimental results to three types of numerical simulations: (i) one-phase boundary integral simulations, (ii) two-phase boundary integral simulations with an incompressible gas-phase, and (iii) a compressible gas version of the second type of simulations that include the gas phase as a compressible fluid. We analyze the time evolution of both the location of the stagnation point in the gas flow and the derived air flow rate and explain our experimental observations in terms of the three types of simulations. The main conclusion is that the behavior that we observe in the experiments can only be reproduced by the simulations if compressibility is taken into account.

Appendix: Derivation of the scaling law for Φ_V^*

In this Appendix we show that the main result of § 2.3.2 can also be derived in a slightly more rigorous manner, starting from the description of the cavity proposed in [17]. The starting point is the two-dimensional Rayleigh equation for the cavity wall $r(z,t)$, which originates from integrating the Euler equations in uncoupled horizontal layers of flow from some far away point R_∞ to the cavity wall

$$\log(r/R_\infty)\frac{d}{dt}(r\dot{r}) + \tfrac{1}{2}\dot{r}^2 = gz \tag{2.9}$$

in which $\dot{r} = \partial r/\partial t$ and g is the acceleration of gravity.

This equation is solved in two different limits to describe the different regions in Fig. 2.11. The first one is to describe region A and B, taking for every depth z the moment $t_M(z)$ of maximum expansion as a reference point. With $r(t_M) = R_M(z)$, $\dot{r}(t_M) = 0$, we can neglect the second term in Eq. (2.9) and replace the slowly varying logarithm in the first term by a constant [§] $\beta \equiv \log(R_M/R_\infty)$ [¶] and solve

$$r(z,t)^2 = R_M(z)^2 - \frac{gz}{\beta}(t - t_M(z))^2 . \tag{2.10}$$

In [17] it was shown that

$$t_M(z) = \frac{z}{U_0} + \alpha_{expa}\beta_{expa}\frac{R_0 U_0}{gz}, \tag{2.11}$$

in which the first term represents the time span needed to arrive at depth z and the second the amount of time to expand to the maximum radius. Here $\alpha_{expa}\beta_{expa}$ is a constant [‖].

[§] Although strictly speaking $R_M(z)$ is a function of z, it is slowly varying and can approximated by a constant when the logarithm of this quantity is taken.

[¶] The constant β is different in the expansion β_{expa} and the contraction phase (β_{ctra}.

[‖] The nomenclature of the constants is chosen such as to be consistent with [17].

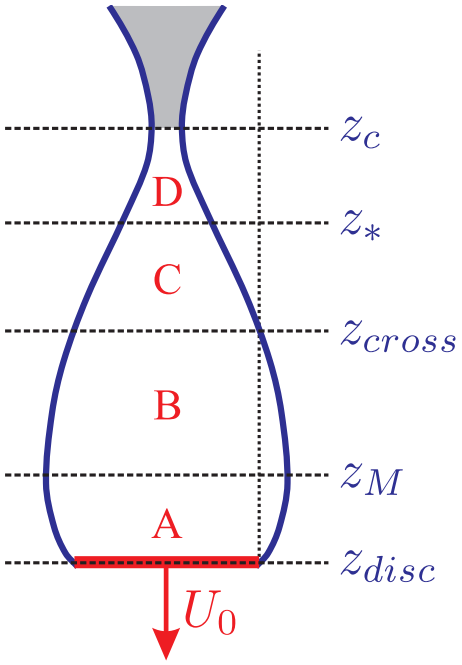

Figure 2.11: For the more rigorous derivation in this Appendix, the cavity close to the pinch-off moment which was divided in five different regions in Fig. 2.5 needs be redivided into four regions: The expansion region (A), between the location of the disc z_{disc} and the location of the maximum z_M, where the cavity expands against hydrostatic pressure; the contraction region (B), between z_M and the point z_{cross} where the cavity reaches the disc radius again where the hydrostatic pressure approximation [Eq. (2.10)] is matched to the inertial approximation [Eq. (2.12)]; the collapse region (C) between z_{cross} and z_*, characterized by continuity; and the self-similarity region (D), between z_* and the pinch off location z_c, which is in addition characterized by a coupling between the vertical and horizontal coordinates.

The second approximate solution corresponds to the small R limit in the collapse regions C and D of Fig. 2.11, in which both the driving pressure gz and the inertial term $\dot{r}^2/2$ can be considered small when $|\log(r/R_\infty)| \gg 1/2$. This then leads to $\frac{d}{dt}(r\dot{r}) = 0$ which is readily solved to give:

$$r(z,t)^2 = 2\alpha_{ctra} R_0 U_0 \left(t_{coll}(z) - t\right) , \tag{2.12}$$

in which α_{ctra} is a constant and $t_{coll}(z)$ is the (virtual) closure time of the cavity at depth z. At any depth z the approximate solutions are tied together at the maximum (where a solution Eq. (2.10) with $\beta = \beta_{expa}$ is matched to a solution with $\beta = \beta_{ctra}$) and at the moment $t_{cross}(z)$ when $r(z,t) = R_0$ again. Here, the solution Eq. (2.10) with $\beta = \beta_{ctra}$ is matched to Eq. (2.12). More details can be found in [17].

The quantity we want to calculate is Eq. (2.3), which contains the time derivatives of Eqs. (2.10) and (2.12), which are:

$$\begin{aligned} \frac{d}{dt}\left(r(z,t)^2\right) &= -2\frac{gz}{\beta}\left(t - t_M(z)\right) \ \ (\text{regionA, B}) \\ \frac{d}{dt}\left(r(z,t)^2\right) &= -2\alpha_{ctra} R_0 U_0 \ \ (\text{regionC, D}) . \end{aligned} \tag{2.13}$$

which subsequently need to be evaluated at the moment of pinch-off $t = t_c$, for which it was derived in [17] that it is independent of the impact speed: $t_c = C_2\sqrt{R_0/g}$ **. Inserting this expression together with Eq. (2.11) into the first Eq. (2.13) gives

$$\begin{aligned} &\frac{d}{dt}\left(r(z,t_c)^2\right) = \\ &-2\frac{gz}{\beta}\left(C_2\sqrt{\frac{R_0}{g}} - \frac{z}{U_0} - \alpha_{expa}\beta_{expa}\frac{R_0 U_0}{gz}\right) . \end{aligned} \tag{2.14}$$

Finally we need to integrate the second Eq. (2.13) and Eq. (2.14) over z between z_{disc} and z_c. This is a straightforward calculation which gives the following lengthy result

$$\begin{aligned} &\int_{z_c}^{z_{\text{disc}}} \frac{d}{dt}\left(r(z,t_c)^2\right) dz = \\ &-\frac{C_2}{\beta_{expa}}\sqrt{R_0 g}\left(z_{\text{disc}}^2 - z_M^2\right) + \frac{2}{3\beta_{expa}}\left(z_{\text{disc}}^3 - z_M^3\right) + \\ &2\alpha_{expa} R_0 U_0 (z_{\text{disc}} - z_M) - \frac{C_2}{\beta_{ctra}}\sqrt{R_0 g}\left(z_M^2 - z_{\text{cross}}^2\right) + \\ &\frac{2}{3\beta_{ctra}}\left(z_M^3 - z_{\text{cross}}^3\right) + 2\alpha_{expa} R_0 U_0 (z_M - z_{\text{cross}}) - \\ &2\alpha_{ctra}(z_{cross} - z_*) - 2\alpha_{ctra}(z_* - z_c) . \end{aligned} \tag{2.15}$$

**The constant C_2 is not independent of the α's and β's: $C_2 = 2(\alpha_{expa}\beta_{expa} + \alpha_{ctra}\beta_{ctra})^{1/2}$.

We now use that all length scales z_{disc}, z_M, z_{cross}, and z_* scale as $R_0 Fr^{1/2}$, except for the difference $(z_* - z_c)$, which due to the self-similarity in the neck radius scales as R_0. This means that the above Eq. (2.15) has the folowing form

$$\int_{z_c}^{z_{\rm disc}} \frac{d}{dt}\left(r(z,t_c)^2\right) dz = \\ -\kappa_1 \sqrt{R_0 g}\, R_0^2 Fr + \kappa_2 g R_0^3 Fr^{3/2} + \kappa_3 R_0^2 U_0 Fr^{1/2} - \kappa_4 R_0^2 U_0 \,, \tag{2.16}$$

in which κ_1-κ_4 are positive numerical constants, which depend on the α's, β's and the proportionality constants in the scaling laws for the length scales z_{disc}, z_M, z_{cross}, z_*, and $(z_* - z_c)$. By writing $\sqrt{R_0 g} = U_0 Fr^{-1/2}$ in the first two terms we finally obtain:

$$\int_{z_c}^{z_{\rm disc}} \frac{d}{dt}\left(r(z,t_c)^2\right) dz = \\ (-\kappa_1 + \kappa_2 + \kappa_3)\, R_0^2 U_0\, Fr^{1/2} \;-\; \kappa_4 R_0^2 U_0 \,. \tag{2.17}$$

If we now insert the above result in Eq. (2.3) we obtain

$$\begin{aligned} \Phi_V &= -\int_{z_c}^{z_{\rm disc}} 2\pi\, r(z,t)\, \dot{r}(z,t,) dz \;-\; \pi R_0^2 U_0 \\ &= \pi(\kappa_1 - \kappa_2 - \kappa_3)\, R_0^2 U_0\, Fr^{1/2} + \pi(\kappa_4 - 1) R_0^2 U_0 \end{aligned} \tag{2.18}$$

which then leads to

$$\Phi_V^* \equiv \frac{\Phi_V}{R_0^2 U_0} = A\, Fr^{1/2} + B \,, \tag{2.19}$$

with $A \equiv \pi(\kappa_1 - \kappa_2 - \kappa_3)$ and $B \equiv \pi(\kappa_4 - 1)$. The shape of this equation is identical to Eq. (2.6) we derived in a more heuristic manner in Subsection 2.3.2.

References

[1] A. M. Worthington and R. S. Cole, *Impact with a Liquid Surface Studied by the Aid of Instantaneous Photography. Paper II*, Phil. Trans. R. Soc. Lond. A **194**, 175–199 (1900).

[2] R. Bergmann, D. van der Meer, M. Stijnman, M. Sandtke, A. Prosperetti, and D. Lohse, *Giant Bubble Pinch-Off*, Phys. Rev. Lett. **96**, 154505 (2006).

[3] C. Duez, C. Ybert, C. Clanet, and L. Bocquet, *Making a splash with water repellency*, Nature Phys. **3**, 180–183 (2007).

[4] S. Gekle, J. M. Gordillo, D. van der Meer, and D. Lohse, *High-Speed Jet Formation after Solid Object Impact*, Phys. Rev. Lett. **102**, 034502 (2009).

[5] J. M. Gordillo, *Axisymmetric Bubble Pinch-Off at High Reynolds Numbers*, Phys. Rev. Lett. **95**, 194501 (2005).

[6] J. M. Gordillo and M. Pérez-Saborid, *Axisymmetric breakup of bubbles at high Reynolds numbers*, J. Fluid Mech. **562**, 303 (2006).

[7] S. Gekle and J. M. Gordillo, *Compressible air flow through a collapsing liquid cavity*, Int. J. Numer. Meth. Fluids (2010).

[8] P. Doshi, I. Cohen, W. W. Zhang, M. Siegel, P. Howell, O. A. Basaran, and S. R. Nagel, *Persistence of Memory in Drop Breakup: The Breakdown of Universality*, Science **302**, 1185–1188 (2003).

[9] N. C. Keim, P. Mø ller, W. W. Zhang, and S. R. Nagel, *Breakup of Air Bubbles in Water: Memory and Breakdown of Cylindrical Symmetry*, Phys. Rev. Lett. **97**, 144503 (2006).

[10] L. E. Schmidt, N. C. Keim, W. W. Zhang, and S. R. Nagel, *Memory-encoding vibrations in a disconnecting air bubble*, Nature Phys. **5**, 343–346 (2009).

[11] K. S. Turitsyn, L. Lai, and W. W. Zhang, *Asymmetric Disconnection of an Underwater Air Bubble: Persistent Neck Vibrations Evolve into a Smooth Contact*, Phys. Rev. Lett. **103**, 124501 (2009).

[12] O. R. Enríquez, I. R. Peters, S. Gekle, L. E. Schmidt, M. Versluis, D. van der Meer, and D. Lohse, *Collapse of nonaxisymmetric cavities*, Phys. Fluids **22**, 091104 (2010).

[13] O. R. Enríquez, I. R. Peters, S. Gekle, L. E. Schmidt, D. van der Meer, and D. Lohse, *Non-axisymmetric impact creates pineapple-shaped cavity*, Phys. Fluids **23**, 091106 (2011).

[14] M. Minnaert, *On musical air-bubbles and the sounds of running water*, Philos. Mag. **16**, 235–248 (1933).

[15] M. Strasberg, *The Pulsation Frequency of Nonspherical Gas Bubbles in Liquids*, The Journal of the Acoustical Society of America **25**, 536–537 (1953).

[16] T. Grumstrup, J. B. Keller, and A. Belmonte, *Cavity Ripples Observed during the Impact of Solid Objects into Liquids*, Phys. Rev. Lett. **99**, 114502 (2007).

[17] R. Bergmann, D. van der Meer, S. Gekle, A. van der Bos, and D. Lohse, *Controlled impact of a disk on a water surface: cavity dynamics*, J. Fluid Mech. **633**, 381–409 (2009).

[18] J. Eggers, M. A. Fontelos, D. Leppinen, and J. H. Snoeijer, *Theory of the Collapsing Axisymmetric Cavity*, Phys. Rev. Lett. **98**, 94502 (2007).

[19] V. Duclaux, F. Caillé, C. Duez, C. Ybert, L. Bocquet, and C. Clanet, *Dynamics of transient cavities*, J. Fluid Mech. **591**, 1–19 (2007).

[20] S. Gekle, J. H. Snoeijer, D. Lohse, and D. van der Meer, *Approach to universality in axisymmetric bubble pinch-off*, Phys. Rev. E **80**, 036305 (2009).

[21] P. Tokumaru and P. Dimotakis, *Image correlation velocimetry*, Exp. Fluids **19**, 1–15 (1995).

[22] J. Westerweel, "Digital Particle Image Velocimetry - Theory and Application", (1993).

[23] M. Honkanen and H. Nobach, *Background extraction from double-frame PIV images*, Exp. Fluids **38**, 348–362 (2005).

3

Supersonic Air Flow due to Solid-Liquid Impact * †

A solid object impacting on liquid creates a liquid jet due to the collapse of the impact cavity. Using visualization experiments with smoke particles and multiscale simulations we show that in addition a high-speed air-jet is pushed out of the cavity. Despite an impact velocity of only 1 m/s, this air-jet attains supersonic *speeds already when the cavity is slightly larger than 1 mm in diameter. The structure of the air flow resembles closely that of compressible flow through a nozzle – with the key difference that here the "nozzle" is a* liquid *cavity shrinking rapidly in time.*

3.1 Introduction

Taking a stone and throwing it onto the quiescent surface of a lake triggers a spectacular series of events which has been the subject of scientists' interest for more than a century [1–17]: upon impact a thin sheet of liquid (the "crown splash") is thrown upwards along the rim of the impacting object while below the water surface a large cavity forms in the wake of the impactor. Due to the hydrostatic pressure of the surrounding liquid this cavity immediately starts to collapse and eventually closes in a single point ejecting a thin, almost needle-like liquid jet. Just prior to the ejection of

*Published as: Stephan Gekle, Ivo R. Peters, José Manuel Gordillo, Devaraj van der Meer, and Detlef Lohse, *Supersonic Air Flow due to Solid-Liquid Impact*, Phys. Rev. Lett. **104**, 024501 (2010)

†The experimental work in this chapter is part of the present thesis. The numerical simulations are due to Stephan Gekle.

the liquid jet the cavity possesses a characteristic elongated "hourglass" shape with a large radius at its bottom, a thin neck region in the center, and a widening exit towards the atmosphere.

This shape is very reminiscent of the converging-diverging ("de Laval") nozzles known from aerodynamics as the paradigmatic picture of compressible gas flow through, e.g., supersonic jet engines. In this chapter we use a combination of experiments and numerical simulations to show that in addition to the very similar shape, also the structure of the air flow through the impact cavity resembles closely the high-speed flow of gas through such a nozzle. Not only is the flow to a good approximation one-dimensional, but it even attains supersonic velocities. Nevertheless, the pressure inside the cavity is merely 2% higher than the surrounding atmosphere. The key difference, however, is that in our case the "nozzle" is a liquid cavity whose shape is evolving rapidly in time – a situation for which no equivalent exists in the scientific or engineering literature.

3.2 Experimental setup

Our experimental setup consists of a thin circular disc with radius $R_0 = 2$ cm which is pulled through the liquid surface by a linear motor mounted at the bottom of a large water tank [16] with a constant speed of $V_0 = 1$ m/s. To visualize the air flow we use small glycerin droplets (diameter roughly 3 μm) produced by a commercially available smoke machine (skytec) commonly used for light effects in theaters and discotheques. Before the start of the experiment the atmosphere above the water surface is filled with this smoke which is consequently entrained into the cavity by the impacting disc. A laser sheet (Lasiris Magnum II, 1500mW) shining in from above illuminates a vertical plane containing the axis of symmetry of the system. A high-speed camera (Photron SA1.1) records the motion of the smoke particles at up to 15,000 frames per second. Cross-correlation of subsequent images allows us to extract the velocity of the smoke which faithfully reflects the actual air speed (see Chapter 2). Our setup obeys axisymmetry and we use cylindrical coordinates with $z = 0$ the level of the undisturbed free surface.

In the beginning of the process (see the snapshot in Fig. 3.1(a)) air is drawn into the expanding cavity behind the impacting object with velocities of the order of the impact speed. In a later stage however, this downward flux is overcompensated by the overall shrinking of the cavity volume resulting in a net flux out of the cavity. The cavity shape at the moment when the flow through the neck reverses its direction is illustrated in Fig. 3.1(b). Towards the end of the cavity collapse a thin and fast air stream is pushed out through the cavity neck which is illustrated in Fig. 3.1(c). From images such as those in Fig. 3.1 we can directly measure the air speed u up to about 10 m/s as is shown in the inset of Fig. 3.2.

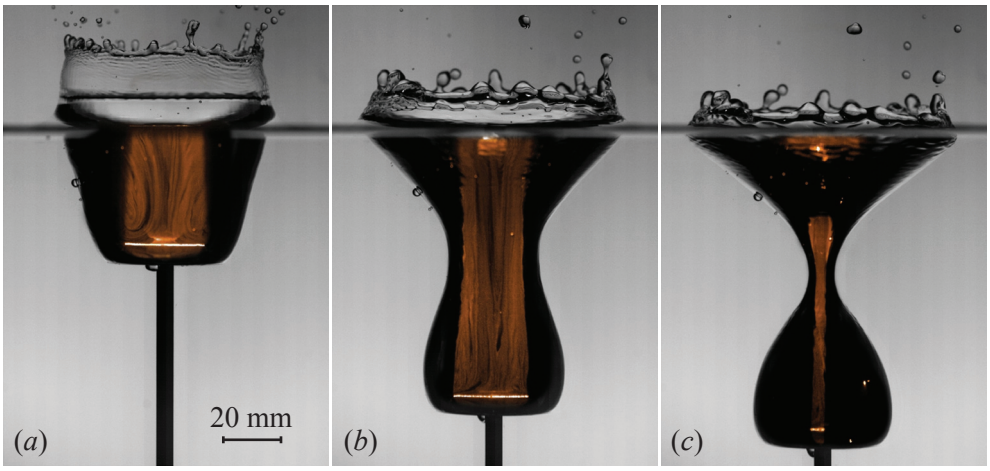

Figure 3.1: (*a*) After the impact of the disc an axisymmetric cavity is formed in its wake and air is entrained into this cavity. (*b*) Due to hydrostatic pressure from the surrounding liquid the cavity starts to collapse and the air flow reverses its direction. (*c*) As the collapse proceeds, air is pushed out of the shrinking cavity at very high speeds. In (*a*)–(*c*) we overlaid images of the cavity shape (recorded with backlight) and images of the smoke particles (recorded with the laser sheet and artificially colored in orange). In the latter, the area illuminated by the vertical laser sheet is restricted by the minimum cavity radius.

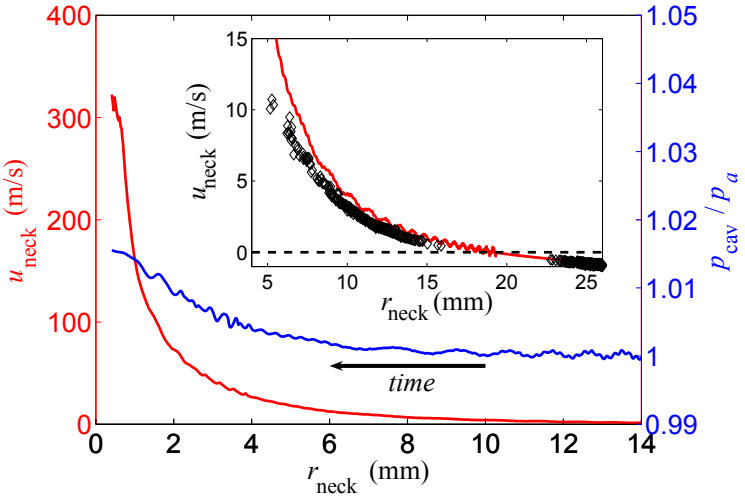

Figure 3.2: The speed of the gas flowing through the neck (red curve) as a function of the shrinking cavity neck taken from the fully compressible simulations. The main plot demonstrates that sonic speeds are attained with the cavity pressure (blue curve) being less than 2% higher than the atmospheric pressure. The enlargement (inset) shows that the numerical scheme (red curve) agrees very well with the experimentally measured velocity (black diamonds; the hole in the data between $r_{neck} = 16$ mm and 22 mm is due to measurement uncertainties at low absolute velocities, see Chapter 2). Slight non-axisymmetric perturbations [18, 19] in the experimental setup may be responsible for the somewhat slower air speed of the experiment as compared to the simulation. One can clearly see the inversion of the flow direction from negative (into the cavity) to positive (out of the cavity) velocities.

3.3 Numerical simulations

In order to determine the flow speed at even higher velocities we revert to multiscale numerical simulations. Our numerical method proceeds in two stages: an incompressible stage at the beginning and a compressible stage towards the end of the impact process. During the first stage both air and liquid are treated as incompressible, irrotational, and inviscid potential fluids. To solve for the flow field and to calculate the motion of the interface we use a boundary integral method (BIM) as described in [16] with extensions to include the gas phase [20]. At the moment that the air flow through the neck reverses, see Fig. 3.1(*b*), the simulation enters into the second, compressible stage: from now on only the liquid motion is computed by the incompressible BIM.

To simulate the air flow in the second stage we need to take compressibility into account meaning that a simple potential flow description is no longer possible. Fortunately, at the end of the incompressible stage the air velocity profile is almost perfectly one-dimensional along the axis of symmetry. We can therefore describe the gas dynamics by the 1D compressible Euler equations [21] in analogy to gas flowing through a converging-diverging nozzle. In the Euler equations we include two additional terms accounting for the variation of the nozzle radius in time and space [22]. For the numerical solution we use a Roe scheme [21, 23] which is highly appreciated for its computational efficiency and ability to accurately capture shock fronts.

The two-way coupling between the gas and the liquid domains is accomplished via (i) the interfacial shape and its instantaneous velocity which is provided by the BIM and serves as an input into the gas solver and (ii) the pressure which is obtained from the solution of the Euler equations and serves as a boundary condition for the BIM. Above the location of the initial free surface the surface pressure of the BIM remains atmospheric.

3.4 Results

Combining our experiments with these numerical simulations leads to the main result of this chapter contained in Fig. 3.2: the collapsing liquid cavity acts as a rapidly deforming nozzle, so violent that the air which is pushed out through the neck attains supersonic velocities (red line). Our simulations show that the pressure inside the cavity which is driving this flow is less than 1.02 atmospheres (blue line). From the inset one can tell that our simulations are in good agreement with the smoke measurements over the entire experimentally accessible range. It is interesting to note that even towards the end of the process (when sonic velocities are reached) there is a net flux of air upwards through the cavity. If the process was governed merely by the collapse of the neck itself one would expect the air to be pushed out of

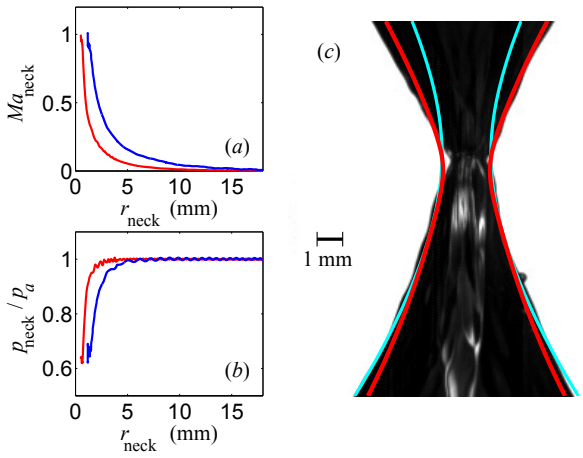

Figure 3.3: (*a*) The evolution of the local Mach number at the cavity neck for different impact speeds (red: 1 m/s, blue: 2 m/s). For the 2 m/s impact speed sonic flow is attained at a cavity radius of 1.2 mm. (*b*) The pressure at the neck diminishes due to Bernoulli suction as the neck radius shrinks and air is forced to flow faster and faster. The minimum pressure lies at about $0.6p_a$ which is attained when the Mach number reaches unity. (*c*) The experimental image shows a pronounced kink at the neck which is not captured by the smoothly rounded curve predicted by the simulation without air (cyan line). Only the inclusion of air effects into the simulations (red line) is able to reproduce the kinked shape caused by the low air pressure at the neck as well as the shape of the cavity above the neck.

the neck region in both vertical directions. This net flow thus underlines the important role of the dynamics of the entire cavity.

To determine more precisely at what point the air flow through the neck becomes sonic we show in Fig. 3.3(*a*) the evolution of the local Mach number, $Ma_{\mathrm{neck}} = u_{\mathrm{neck}}/c$ (with the gas velocity u_{neck} and the speed of sound c), for discs impacting at 1 and 2 m/s. We find that the speed of sound is attained at cavity radii as large as 0.5 mm for the lower impact velocity and 1.2 mm for the higher impact velocity.

In a steady state one could expect from the (compressible) Bernoulli equation that these very high air speeds would cause a greatly diminished air pressure in the neck region. Despite the unsteadiness of our situation, the data presented in Fig. 3.3(*b*) indeed shows that the pressure p_{neck} decreases significantly once the neck has shrunk to a diameter of roughly 4 mm (for the 1 m/s impact) while before that point it is practically atmospheric throughout. Classical steady-state theory [24] for a converging-diverging nozzle predicts that when $Ma_{\mathrm{neck}} = 1$ the pressure at the neck reaches a

minimum value of

$$p_{\text{neck}}/p_a = \left(1+\frac{\gamma-1}{2}\right)^{-\gamma/(\gamma-1)} = 0.53 \tag{3.1}$$

with p_a the atmospheric pressure and $\gamma = 1.4$ the isentropic exponent. As shown in Fig. 3.3(b) our situation – although highly unsteady – exhibits a similar behavior with $p_{\text{neck}} \approx 0.6 p_a$ as the Mach number becomes of order unity.

In Fig. 3.3(c) we illustrate how this low pressure gives us a handle to observe the consequences of the supersonic air speed in our experiments: despite the air being three orders of magnitude less dense than water, it is able to exert a significant influence even on the shape of the liquid cavity provided that its speed is high enough [25, 26]. From the experimental image it is clear that the free surface close to collapse no longer possesses a smoothly rounded shape but instead shows a significant increase in curvature at the minimum (a "kink"). While this feature is not present in a simulation neglecting the influence of air as those in [16], the inclusion of air effects allows us to capture quite accurately the cavity shape observed experimentally. This gives strong evidence that in the experiment the air indeed becomes as fast as predicted by the simulations and produces a Bernoulli suction effect strong enough to deform the cavity.

The positive sign of u_{neck} (see Fig. 3.2) indicates that the gas flow is directed upwards at the neck. At the same time, the air at the bottom of the cavity is pulled downwards by the moving disc. An interesting consequence of this competition between cavity expansion at the bottom and cavity shrinking in the neck is the existence of a stagnation point with $u = 0$ as can readily be observed in Fig. 3.4(a) and its magnification in Fig. 3.4(c).

As can be seen in the inset of Fig. 3.5, the distance between the neck and the stagnation point is no larger than roughly 5 mm prior to cavity closure. Nevertheless, the pressure at the stagnation point equals the overall pressure inside the cavity which is roughly atmospheric during the whole process (see Fig. 3.2). Recalling that $p_{\text{neck}} \approx 0.6 p_a$ this results in a tremendous vertical pressure gradient which of course affects the dynamics of the cavity wall: the flow of air is so strong that it can drag the liquid along resulting in an upward motion of the cavity neck just before the final collapse. That this effect is indeed present in the simulations can be seen from the red line in Fig. 3.5. For comparison, the cyan curve demonstrates that a single fluid simulation neglecting the air dynamics would predict a monotonously decreasing position. The experimental data however is in quantitative agreement with the compressible simulations. Together with the cavity shape shown in Fig. 3.3(c) these results constitute an impressive – albeit indirect – demonstration of the credibility of our numerical predictions despite the fact that, understandably, it is not possible to directly measure (super-)sonic air speeds with our smoke setup. Furthermore they show that the perfectly axisymmetric approach of the simulations is justified and,

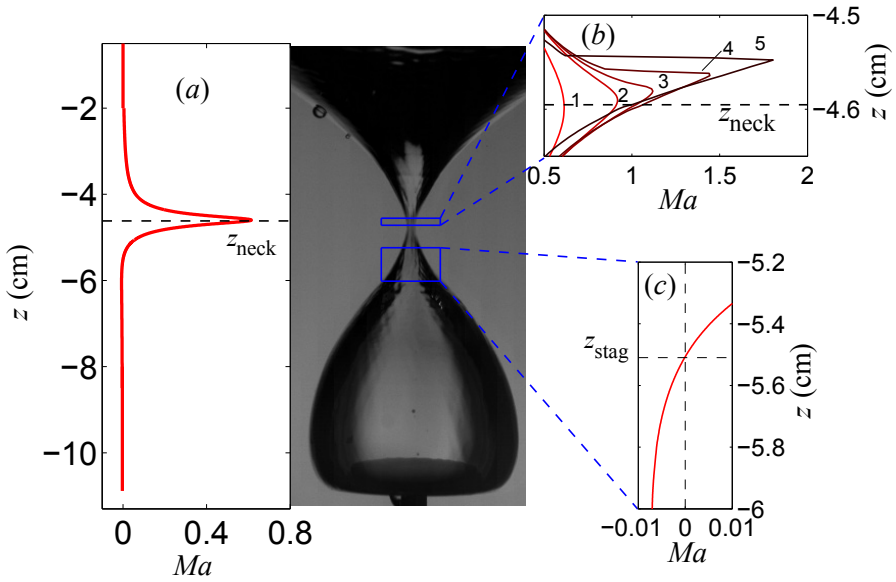

Figure 3.4: (*a*) The vertical air velocity normalized by the local speed of sound $Ma = u/c$ as a function of the vertical position (the corresponding cavity image is shown in the middle) for $r_{neck} = 0.9$ mm: the profile exhibits a sharp peak approximately at the height of the neck. (*b*) A close-up of the zone around the neck illustrates the steepening of the velocity profiles towards pinch-off (numbers 1-5 correspond to neck radii between 0.9 mm (number 1, bright red) and 0.5 mm (number 5, dark brown)) and the development of the shock front at roughly 0.1 ms before pinch-off. The neck position z_{neck} corresponding to curve 5 is shown by the dashed line. (*c*) A close-up of the area below the neck shows the location of the gas flow stagnation point z_{stag} (dashed line).

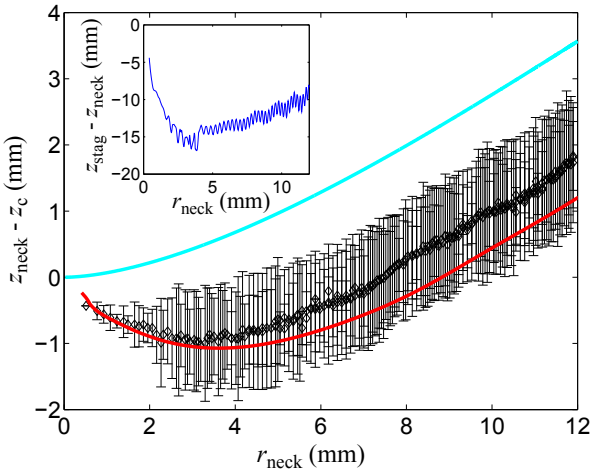

Figure 3.5: The vertical position of the cavity neck relative to the final closure height z_c as a function of the shrinking neck radius from experiment (black diamonds), simulations with (red line) and without (cyan line) air dynamics. The experimental data is in quantitative agreement with the compressible simulations, while clearly the simulation neglecting air fails to capture the upward motion of the minimum induced by the large pressure gradient between the stagnation point and the cavity neck. Experimental error bars are determined by the number of vertically neighboring pixels all sharing the same minimum radius. The inset shows the approach of the stagnation point to the neck.

therefore, that supersonic gas velocities are reached before instabilities [18, 19] inevitably destroy the axisymmetry of the system.

Looking more closely at the velocity profile above the neck (see Fig. 3.4(*b*)) one finds that it possesses a discontinuous jump: the signature of a shock front developing in the air stream. While such a shock front is a common phenomenon in steady supersonic flows, here we are able to illustrate its development even in our highly unsteady situation when the gas velocity passes from sub- to supersonic.

3.5 Conclusions

We showed that the air flow inside the impact cavity formed by a solid object hitting a liquid surface attains supersonic velocities. We found that the very high air speeds can be reached even though the pressure inside the cavity is merely 2% higher than the surrounding atmosphere. This is due to the highly unsteady gas flow created by the rapidly deforming cavity. We illustrated how the air affects the cavity shape close

to the final collapse in two different ways: (i) the initially smoothly curved neck shape acquires a kink which can be attributed to a Bernoulli suction effect and (ii) the initially downward motion of the neck reverses its direction and starts to travel upwards. The quantitatively consistent observation of both effects in numerics and experiment makes us confident that our rather involved numerical procedure truthfully reflects reality.

References

[1] A. M. Worthington, *A study of splashes* (Longmans, Green and Co., London) (1908).

[2] D. Gilbarg and R. A. Anderson, *Influence of atmospheric pressure on the phenomena accompanying the entry of spheres into water*, J. Appl. Phys. **19**, 127–139 (1948).

[3] A. May, *Effect of surface condition of a sphere on its water-entry cavity*, J. Appl. Phys. **22**, 1219–1222 (1951).

[4] A. May, *Vertical entry of missiles into water*, J. Appl. Phys. **23**, 1362–1372 (1952).

[5] H. I. Abelson, *Pressure measurements in the water-entry cavity*, J. Fluid Mech. **44**, 129–144 (1970).

[6] J. W. Glasheen and T. A. McMahon, *Vertical water entry of disks at low Froude numbers*, Phys. Fluids **8**, 2078–2083 (1996).

[7] M. Lee, R. G. Longoria, and D. E. Wilson, *Cavity dynamics in high-speed water entry*, Phys. Fluids **9**, 540–550 (1997).

[8] S. Gaudet, *Numerical simulation of circular disks entering the free surface of a fluid*, Phys. Fluids **10**, 2489–2499 (1998).

[9] R. Bergmann, D. van der Meer, M. Stijnman, M. Sandtke, A. Prosperetti, and D. Lohse, *Giant bubble pinch-off*, Phys. Rev. Lett. **96**, 154505 (2006).

[10] V. Duclaux, F. Caillé, C. Duez, C. Ybert, L. Bocquet, and C. Clanet, *Dynamics of transient cavities*, J. Fluid Mech. **591**, 1–19 (2007).

[11] D. Vella and P. D. Metcalfe, *Surface tension dominated impact*, Phys. Fluids **19**, 072108 (2007).

[12] C. Duez, C. Ybert, C. Clanet, and L. Bocquet, *Making a splash with water repellency*, Nature Physics **3**, 180–183 (2007).

[13] S. Gekle, A. van der Bos, R. Bergmann, D. van der Meer, and D. Lohse, *Non-continuous Froude number scaling for the closure depth of a cylindrical cavity*, Phys. Rev. Lett. **100**, 084502 (2008).

[14] S. Gekle, J. M. Gordillo, D. van der Meer, and D. Lohse, *High-speed jet formation after solid object impact*, Phys. Rev. Lett. **102**, 034502 (2009).

[15] J. M. Aristoff and J. W. M. Bush, *Water entry of small hydrophobic spheres*, J. Fluid Mech. **619**, 45–78 (2009).

[16] R. Bergmann, D. van der Meer, S. Gekle, A. van der Bos, and D. Lohse, *Controlled impact of a disc on a water surface: Cavity dynamics*, J. Fluid Mech. **633**, 381–409 (2009).

[17] M. Do-Quang and G. Amberg, *The splash of a solid sphere impacting on a liquid surface: Numerical simulation of the influence of wetting*, Phys. Fluids **21**, 022102 (2009).

[18] L. E. Schmidt, N. C. Keim, W. W. Zhang, and S. R. Nagel, *Memory-encoding vibrations in a disconnecting air bubble*, Nature physics **5**, 343–346 (2009).

[19] K. S. Turitsyn, L. Lai, and W. W. Zhang, *Asymmetric bubble disconnection: persistent vibration evolves into smooth contact*, Phys. Rev. Lett. **103**, 124501 (2009).

[20] J. Rodríguez-Rodríguez, J. M. Gordillo, and C. Martínez-Bazán, *Breakup time and morphology of drops and bubbles in a high-Reynolds-number flow*, J. Fluid Mech. **548**, 69–86 (2006).

[21] C. Laney, *Computational gasdynamics* (Cambridge University Press) (1998).

[22] S. Gekle and J. M. Gordillo, *Compressible air flow through a collapsing liquid cavity*, Int. J. Numer. Meth. Fluids (2010).

[23] P. L. Roe, *Approximate Riemann solvers, parameter vectors, and difference schemes*, J. Comput. Phys. **43**, 357–372 (1981).

[24] H. W. Liepman and A. Roshko, *Elements of gas dynamics* (Wiley) (1957).

[25] J. M. Gordillo, A. Sevilla, J. Rodríguez-Rodríguez, and C. Martínez-Bazán, *Axisymmetric bubble pinch-off at high Reynolds numbers*, Phys. Rev. Lett. **95**, 194501 (2005).

[26] R. Bergmann, A. Andersen, D. van der Meer, and T. Bohr, *Bubble pinch-off in a rotating flow*, Phys. Rev. Lett. **102**, 204501 (2009).

4

Collapse and pinch-off of a non-axisymmetric impact-created air cavity in water *

The axisymmetric collapse of a cylindrical air cavity in water follows a universal power law with logarithmic corrections. Nonetheless, it has been suggested that the introduction of a small azimuthal disturbance induces a long-term memory effect, reflecting in oscillations which are no longer universal but remember the initial condition. In this chapter, we create non-axisymmetric air cavities by driving a metal disc through an initially quiescent water surface and observe their subsequent gravity-induced collapse. The cavities are characterized by azimuthal harmonic disturbances with a single mode number m and amplitude a_m. For small initial distortion amplitude (1 or 2 % of the mean disc radius), the cavity walls oscillate linearly during collapse, with nearly constant amplitude and increasing frequency. As the amplitude is increased, higher harmonics are triggered in the oscillations and we observe more complex pinch-off modes. For small-amplitude disturbances we compare our experimental results with the model for the amplitude of the oscillations by Schmidt et al. (2009) [1] and the model for the collapse of an axisymmetric impact-created cavity previously proposed by Bergmann et al. (2009) [2]. By combining these two models we can reconstruct the three-dimensional shape of the cavity at any time before pinch-off.

*Published as: O.R. Enriquez, I.R. Peters, S. Gekle, L.E. Schmidt, D. Lohse and D. van der Meer, *Collapse and pinch-off of a non-axisymmetric impact-created air cavity in water* J. Fluid Mech. (2012)

4.1 Introduction

The pinch-off of an axisymmetric air cavity in water is characterized by a finite-time singularity. The kinetic energy of the flow is focused into a vanishing small volume with a velocity whose magnitude diverges as the pinch-off moment is approached. Several experimental and theoretical scenarios have been considered recently in the study of this problem: a bubble rising from a capillary [3–6], bubbles in a co-flowing liquid [7, 8], an initially necked bubble [9], and cavities created through impact [2, 10, 11]. Depending on the case, the collapse might be initiated by surface tension, external flow, or hydrostatic pressure. However, irrespective of the cause, towards the end it is the inertia of the fluid that takes over in every case, and the collapse is accelerated as the radius of the cavity shrinks.

The time it takes each of these systems to reach the inertial collapse regime varies by orders of magnitude [12]. Hence, it was not an easy task to determine whether there was indeed a universal behavior underlying this phenomenon. The first proposed model was a power law where the radius decreased proportionally to the square root of the remaining time until collapse, τ [3, 4]. Subsequent experimental and numerical studies consistently found the behavior deviated slightly from that $\frac{1}{2}$ power law [2, 5–7, 10, 13], generating doubts and starting a controversy about the universality of the phenomenon. [14] and [9] theoretically showed how the power law varies weakly as a function of τ due to a logarithmic correction.

In conclusion, the axisymmetric problem converges to a universal self-similar solution. If axial symmetry is broken by a small azimuthal perturbation, a truly universal system would be expected to converge to the same solution. However, through experiments and simulations of an air bubble disconnecting from an underwater nozzle, it was shown recently that a slight azimuthal asymmetry can trigger vibrations that persist in time [1, 13, 15, 16]. The fact that a small perturbation is not smoothed out indicates that the system possesses memory of its initial conditions. Here we conduct an experimental study of the evolution of azimuthal disturbances in the collapse of an otherwise axisymmetric cavity.

Impact vs. detachment

We study the cavity produced when a round disc with an azimuthal disturbance of its edge is driven downwards through the free surface of a water volume (see Figs. 4.1 and 4.2). This is to be contrasted with the detachment of a bubble from a nozzle with a similar disturbance, which is initially determined by the competition of buoyancy forces with surface tension. The latter effectively smooths out large-amplitude and high-mode-number (short-wavelength) perturbations, making nozzle experiments appropriate only for working with small-amplitude, long-wavelength disturbances. In addition, if the bubble is grown quasi-statically, viscosity can also play a role in

smoothing perturbations due to the small Reynolds number of the water flow induced by the injected air. Therefore, this experiment does not allow much variation of the perturbations' mode number and amplitude.

On the other hand, impact-created cavities are characterized by high Weber and Reynolds numbers from the beginning (provided that the collision speed is high enough). Then, viscosity and surface tension play a marginal role in the formation of the cavity and are given no opportunity to erase features created by large-amplitude or high-mode perturbations. There is no initial surface-tension-driven stage in the implosion; instead, the expansion of the cavity is opposed by hydrostatic pressure, which eventually starts the collapse, and is then quickly taken over by inertia. On top of this, since the cavities are created on a free surface, there is unobstructed optical access from the top, making it possible to track the shape of the horizontal section of the collapsing cavity. Disc impact experiments are consequently ideal for experimenting with the influence of geometry in cavity collapse.

The effects of breaking the axial symmetry are clear (Fig. 4.1). We present experimental results of cavities with disturbances of mode numbers 2 to 20 and amplitudes ranging from 1% to 25% of the mean disc radius. The experimental setup is described in §4.2. We then explain the axisymmetric collapse model and the theory for the evolution of a perturbation in §4.3. Our experimental observations are shown and discussed in §4.4. The collapse of small-amplitude cavities viewed from the top and the side, and the comparison with theory are presented in §4.4.2. Finally, we discuss the collapse of high-amplitude shapes in §4.4.3 and draw general conclusions in §4.5.

4.2 Experimental setup and procedure

4.2.1 Setup

The experimental setup consists of a linear motor that drives a vertical thin steel rod downwards through the bottom of a glass tank containing $50 \times 50 \times 50\,\mathrm{cm}^3$ of water (Fig. 4.2). A disc is attached horizontally to the top end of the rod with a mounting system that ensures that the disc is parallel to the undisturbed water surface and remains so throughout the impact. The motor is capable of a maximal $300\,\mathrm{m/s}^2$ acceleration and its position can be controlled with a resolution of 5 μm over its 1 m long track. Since the objects are not dropped into the water, velocity is a control parameter and not a response of the system. The setup allows for a precise control of the impact velocity in the range $0-5\,\mathrm{m/s}$. A more detailed description of the apparatus can be found in [2].

The shapes of the impacted discs are described by the function $r = S_{disc}(\theta)$, where

$$S_{disc}(\theta) = R_{disc} + a_m \cos(m\theta), \tag{4.1}$$

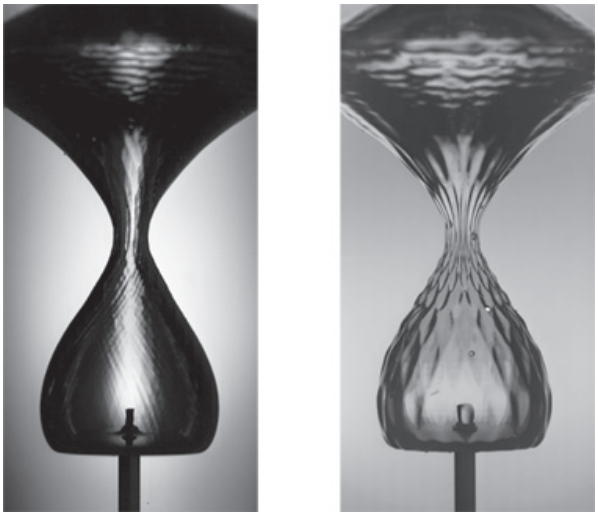

Figure 4.1: Collapse of a cavity created through impact of a round disc (*a*) and another using a disc with an azimuthal disturbance of mode number 20 (*b*) and amplitude of 2% of the mean disc radius. In both cases the mean radius of the disc is 20 mm and the impact speed 1 m/s. The walls of the cavity in (*b*) acquire a structure that resembles the skin of a pineapple. This is explained by the oscillations triggered by the azimuthal disturbance.

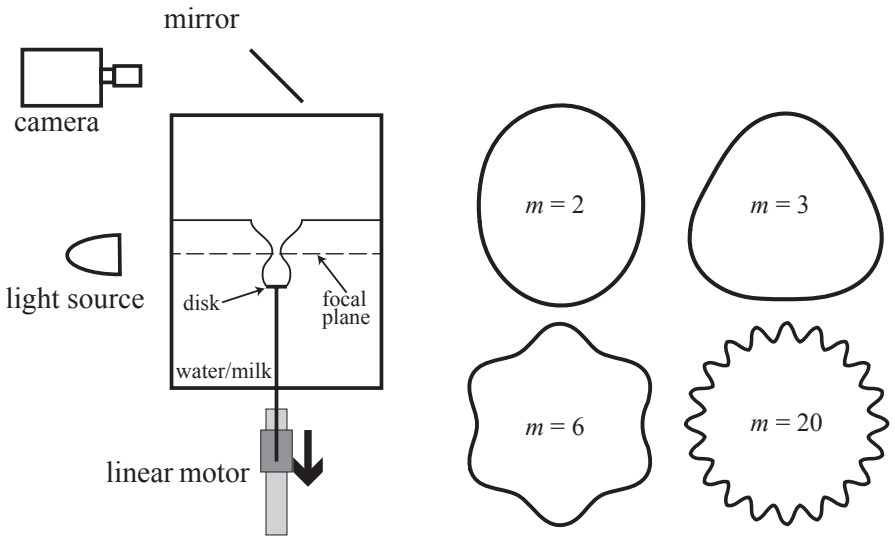

Figure 4.2: Experimental setup and examples of impacting discs. This camera-mirror configuration is used for top views; for side videos we simply move the camera down to the level where the light is. The shown discs have a disturbance amplitude of 10% of the mean radius (R_{disc}).

R_{disc} is the mean radius, a_m the disturbance's amplitude and m its mode number (Fig. 4.2). Discs are machined from a flat stainless-steel plate with a 2 mm thickness. The edges are sharpened to right angles with the intention of pinning the contact line to the lower edge and thus minimize the influence of wetting effects. Great care was taken to ensure that both the disc and the rod were dry before each run, as a single remaining drop on either is enough to noticeably alter the dynamics, especially towards the final instants before pinch-off.

We recorded videos using a Photron SA1.1 high-speed camera at frame rates from $5,400$ to $20,000$ fps with resolutions ranging from 1024×1024 to 512×512 pixels. We image both top views of the collapsing cavity (focusing on the pinch-off plane) and side views to observe its structure. In order to avoid uneven optical reflections from the surface during top-view experiments, in some of the runs we diluted 1 g of milk powder per liter of water and shone light at the liquid, obtaining evenly scattered lighting. In this case the top surface of the disc was covered with black tape for improved contrast. For side views we used water without milk and diffuse illumination from the back. Top view videos were processed to extract the contour of the cavity in every frame and track the amplitude of disturbances as a function of time (§4.4.2). Side views were directly compared with three-dimensional parametric plots of the modeling equations (§4.4.2).

4.2.2 Parameters

The formation of a cavity after impact and its subsequent collapse are determined by the mean radius R_{disc} of the disc, its shape, the impact velocity V_0, and fluid properties such as kinematic viscosity ν, density ρ, and surface tension σ. Hence, the dimensionless parameters of this experiment are the Reynolds number, $Re = V_0 R_{disc}/\nu$, the Froude number $Fr = V_0^2/(R_{disc}g)$, and the Weber number, $We = \rho V_0^2 R_{disc}/\sigma$. The surface tension (and, thus, *We*) is the only property that varies significantly following the addition of milk for some of the experiments. Since we focus on analyzing the influence of the impactor's geometry, the impact speed and the mean disc radius were kept constant in all experiments reported here ($V_0 = 1$ m/s and $R_{disc} = 0.02$ m). In this way, the two variable control parameters –the mode number m and the amplitude a_m– are related exclusively to the shape of the disc. In all of our experiments: $Re \sim 2 \cdot 10^4$, $Fr \sim 5$, and $We \sim 300 - 400$ (with measured surface tension values of [72 mN/m] for water and [47.1 mN/m] for the milk solution, respectively). These values indicate that the dynamics is dominated by inertia from the start of the experiment, and a scaling analysis reveals that this condition prevails throughout the experiment, making it unnecessary to consider their dynamic values. In the end, the only relevant control parameter during the evolution of the cavity is the Froude number since it is the parameter that determines when the cavity enters the inertial collapse regime [12].

4.3 Models of cavity collapse

4.3.1 Axisymmetric radial dynamics

The model for an axisymmetric, impact-created cavity collapse by [2] neglects vertical flow and its derivatives, assuming the collapse at each height z to be entirely decoupled from other heights, following previous works [3, 4]. Since the flow is considered to be exclusively in the radial direction, the only relevant term from the continuity equation in cylindrical coordinates is

$$\frac{1}{r}\frac{\partial}{\partial r} r u_r = 0. \tag{4.2}$$

Integration of this equation, with the boundary condition that at the free surface the velocities of the water and the interface must be the same, i.e., $u_r(R) = \dot{R}$ leads to

$$u_r = \frac{R\dot{R}}{r}, \tag{4.3}$$

which corresponds to a two-dimensional sink flow of strength $Q(t) = R\dot{R}$, where $R(t)$ is the radius of the cavity, and potential

$$\Phi = Q(t)\ln(r). \tag{4.4}$$

Conservation of momentum is expressed by Euler's equation of inviscid motion:

$$-\frac{1}{\rho}\frac{\partial P}{\partial r} = \frac{\partial u_r}{\partial t} + u_r\frac{\partial u_r}{\partial r}, \tag{4.5}$$

which must be integrated from the cavity radius R to R_∞. The upper integration limit is the length scale where the radial flow has decayed ($R_\infty \gg R(t)$); strictly, it should depend on the Froude number and time, but it is possible to determine an approximate constant average value from the experimental conditions and dimensions [2]. With ΔP being the (positive) difference between the hydrostatic pressure at R_∞ and the atmospheric pressure at the free surface of the cavity and accounting for the Laplace pressure jump (σ/R) across the interface at $R(t)$, integration of (4.5) yields:

$$\Delta P + \frac{\sigma}{R} = \rho\left[\frac{1}{2}\dot{R}^2 + \left(\dot{R}^2 + R\ddot{R}\right)\ln\left(\frac{R}{R_\infty}\right)\right], \tag{4.6}$$

where terms of $O(R/R_\infty)$ and smaller were neglected.

In this way, the collapse at each height z is modeled like a two-dimensional Rayleigh-Plesset bubble collapse and the whole cavity is composed of a series of such collapses with different starting times as suggested by [17] in the context of the void collapse in quicksand. The original model does not include surface tension since an analysis of the dimensionless numbers from the problem reveals that surface tension never plays a major role in such a collapse. However, we have included it since disturbing the shape of the cavity creates regions of highly increased curvature where surface tension might play a role.

During the inertial part of the collapse, the logarithmic term in (4.6) diverges as R goes to zero and thus the only way that equation can remain valid is by having the pre-factor of the logarithmic term go to zero. Integration from time t until the collapse time t_{coll} yields a power law $R(t) = \alpha(t_{coll} - t)^{1/2}$.

Experimental studies [2, 5–7, 10, 13] have found that the exponent of the power law is higher than $\frac{1}{2}$ (typical values found are $0.54 - 0.60$) and theoretical studies [9, 12, 14] have shown that the exponent indeed has a weak dependence on the logarithm of the remaining collapse time, approximating to $\frac{1}{2}$ only asymptotically at the end. Nonetheless, the full theoretical result lies remarkably close to a power law fit over many decades in time. Hence, we model the (dimensionless) mean radius $\widetilde{R}$ of our disturbed collapsing cavities as

$$\widetilde{R} = \alpha\left(\widetilde{t}_{coll} - \widetilde{t}\right)^{\beta}, \tag{4.7}$$

where the tilde indicates dimensionless quantities obtained by dividing length scales by R_{disc} and time scales by R_{disc}/V_0, i.e., $\widetilde{R}(\widetilde{t}) = R(t)/R_{disc}$, $\widetilde{t} = tV_0/R_{disc}$ and $\widetilde{t}_{coll} = t_{coll}V_0/R_{disc}$.

4.3.2 Azimuthal disturbance

Memory-encoding vibrations induced by a small geometric disturbance have been predicted theoretically for any mode number m, and observed experimentally for cavities with $m = 2$ and $m = 3$ disturbances, namely bubbles released underwater from a slot-shaped nozzle, by [1] and [16]. The theoretical model was derived through a perturbation analysis of an azimuthal distortion to the geometry of a cavity with the behavior described by (4.6). A brief explanation of the model follows for the sake of clarity. The complete derivation can be found in [18].

Modeling the flow in an axisymmetric collapse as inviscid, irrotational, and incompressible (using Euler's equations) implies that there is no dissipation of energy. If so, the sum of kinetic and potential energies of the system will be conserved and can be expressed using the Hamiltonian:

$$H(R,P_R) = \frac{P_R^2}{2M(R)} + \Delta P \pi R^2 + \sigma 2\pi R. \tag{4.8}$$

The first term on the right is the total kinetic energy of the moving fluid, expressed in terms of the effective mass and its momentum, which are, respectively,

$$M(R) = 2\rho\pi R^2 \ln(\frac{R_\infty}{R}) \tag{4.9}$$

$$P_R = M(R)\frac{dR}{dt}. \tag{4.10}$$

The second term is the potential energy due to the pressure difference between the fluid bulk and the cavity (at ambient pressure), and the third term is the energy cost of creating a free surface with the shape of the void. Applying Hamilton's equations of motion $\dot{R} = \partial H/\partial P_R$ and $\dot{P_R} = -\partial H/\partial R$ we recover (4.6). We are thus faced with a dynamics with one degree of freedom, R, and one constant of motion, namely the total energy. The implications of this are important: the problem is integrable, has a perfect memory, and according to the Kolmogorov-Arnold-Moser theorem if such a system is perturbed the new dynamics should closely follow that of the unperturbed situation, i.e., breaking the axial symmetry of the cavity by introducing a small disturbance of the shape should yield a collapse with the same leading order dynamics and new (approximately) conserved quantities, keeping it nearly integrable.

Although in our experiments the disturbance of the shape of the cavity is characterized by a single mode m, the theoretical analysis considers a perturbation composed of a sum of Fourier modes $\cos(m\theta)$. For a conveniently chosen origin of the θ coordinate, the perturbed shape of the void is

$$S(\theta,t) = R(t) + \sum_m a_m(t)\cos(m\theta), \tag{4.11}$$

where $R(t)$ is the mean cavity radius, which should follow the dynamics of the axisymmetric case, and $a_m(t)$ is the amplitude of each mode, which must be small when compared with the mean radius ($a_m(t)/R(t) \ll 1$) in order for the small perturbation theory to hold. Analysis of how the flow is modified by this shape disturbance [1, 18] gives a linear second order ordinary differential equation (ODE) for the dependence of time evolution of the amplitudes a_m on the mean radial dynamics:

$$\ddot{a}_m + \left(\frac{2\dot{R}}{R}\right)\dot{a}_m + \left(\frac{\ddot{R}}{R}(1-m) + \frac{\sigma m(m^2-1)}{\rho R^3}\right)a_m = 0. \tag{4.12}$$

Eq. (4.12) includes the additional influence of surface tension due to the surface disturbances on the right hand side of (4.11). We can find an approximate solution by substituting $R(t) = \alpha(t_{coll} - t)^{1/2}$, neglecting surface tension, and solving the resulting Cauchy-Euler equation. In dimensionless form this gives

$$\widetilde{a}_m(t) = \widetilde{a}_m(0)\cos\left(\tfrac{1}{2}\sqrt{m-1}\ln\left(\widetilde{t}_{coll} - \widetilde{t}\right)\right). \tag{4.13}$$

We see that the amplitude should oscillate with a constant magnitude and a frequency that diverges as $\widetilde{t}$ approaches $\widetilde{t}_{coll}$ and that higher mode numbers will oscillate faster.

Neglecting surface tension, a useful argument to understand the physics of the predicted oscillations is the following: when the shape of the cavity is disturbed, its curvature is no longer uniform. Therefore, neither is the acceleration of the converging flow associated to its collapse. As a result of continuity, convergence is stronger in regions with larger curvature, which consequently accelerate more and overtake the regions with smaller curvature (Figs. 4.3 and 4.4), inverting the shape of the cavity. The higher the curvature, the quicker the overtaking becomes; thus with larger mode numbers more oscillation cycles are visible (Fig. 4.5).

Qualitatively, there is a connection to other instabilities that occur on accelerated fluid interfaces, like the Rayleigh-Taylor (RT) and Richtmeyer-Meshkov (RM) instabilities. Quantitatively this connection is less clear since, instead of being constant (RT) or shock-like (RM), in our case the acceleration is rapidly increasing in magnitude, and even diverges as $\tau \to 0$ as a consequence of continuity.

Eq. (4.12), along with that for the axisymmetric radial dynamics (4.6) are the ingredients for the comparison of the observed cavity shapes obtained from experiments with theory (§4.4.2).

4.4 Experimental observations

4.4.1 Breaking the axial symmetry: general collapse mechanism

Figure 4.3 shows the collapse of an elliptical cavity (which can be approximated as an $m = 2$ disturbance to a circle) where the longer side of the cavity closes first.

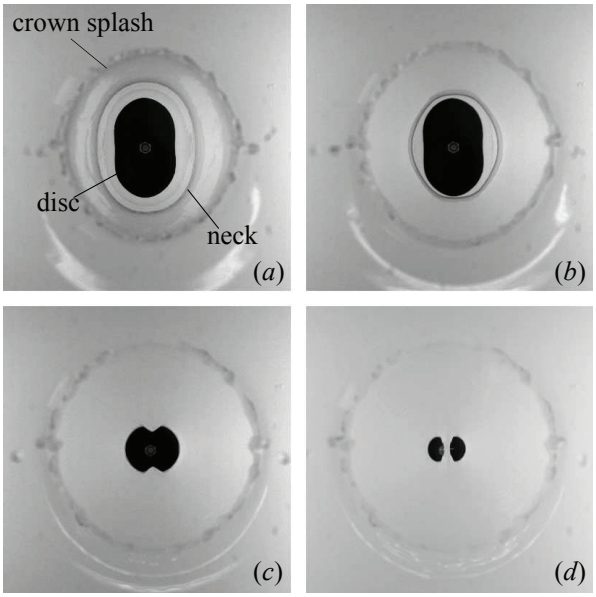

Figure 4.3: Top view of a collapsing cavity ($m = 2$, $R_{disc} = 20$ mm $a_2 = 0.25R_{disc}$) focused on the pinch-off plane. The cavity (neck) and the disc are initially in phase (a). Since the curvature is higher at the top and bottom of the neck, acceleration along the longer axis is larger. This changes the shape of the cavity as it collapses (b and c). Finally, the two points that were originally farthest apart come into contact first (d).

Initially, the shape of the cavity is the same as the impactor that created it (Fig. 4.3a). As it closes, the points that were originally farthest apart come towards each other at a higher speed than that of the end points of the minor axis (Fig. 4.3b). Eventually it becomes clear that the shape of the cavity has inverted its phase with respect to the impactor (Fig. 4.3c). This shift can be considered as an amplitude inversion of the original shape, described as $S(\theta,t) = R(t) + a_m \cos(m\theta)$ where $R(t)$ is the mean radius and the amplitude, a, is originally positive and then becomes negative.

For small amplitudes (1 or 2% of the mean radius), oscillations remain linear and with a nearly constant amplitude until very close to the pinch-off moment. However, the fact that we have a disturbance with constant amplitude in a shrinking geometry implies that the disturbance is actually growing with respect to the mean radius and hence it is bound to become of the same order of magnitude at some point. When this happens, the system starts developing higher harmonics and the linear oscillation model can no longer describe the events. At that moment, we say that the collapse evolves into a non-linear behavior. This was observed for all mode numbers from 2 to 20. In §4.4.2 we first discuss the linear regime, and afterwards turn to the non-linear effects in §4.4.3.

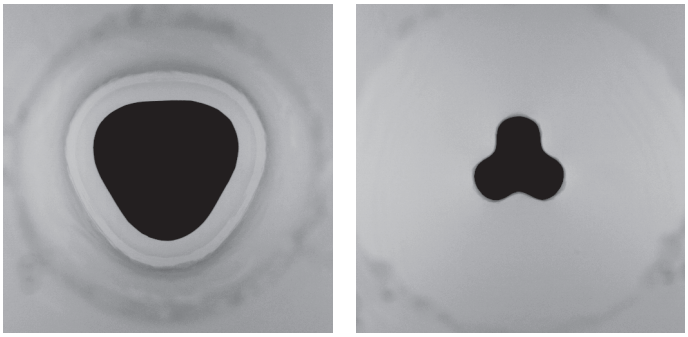

(*a*) (*b*)

Figure 4.4: Image of an $m = 3$, $R_{disc} = 20$ mm, $a = 0.1R_{disc}$ cavity, approximately 10 ms after disc impact (*a*). Approximately 90 ms afterwards, it is clear that the shape has inverted with respect to the original (*b*).

4.4.2 Effect of small-amplitude disturbances

Events on the pinch-off plane

Small disturbances do not decay during the collapse of the cavities formed in our experiments. In Fig. 4.5 we show as an example eight snapshots of the evolution of an $m = 16$ cavity. Within the bounds set by the used frame rate and resolution (20000 fps and a scale of approximately 86 μm/pixel), the cavities retain memory of the shape that created them throughout the whole collapse process. We tracked the edge of the cavity $S(\theta,t)$ at every frame from the top-view videos, and found the mean radius $R(t)$ and disturbance amplitude $a_m(t)$ at each time by fitting the curve

$$S(\theta,t) = R(t) + a_m(t)\cos(m\theta + \phi_m(t)), \tag{4.14}$$

which is Eq. (4.11) for a single mode perturbation. Since $\phi_m(t)$ was found to be nearly constant in time, we chose the reference angle $\theta = 0$ to be any line of symmetry in order to match with the model's description of the free surface.

We determined the proportionality constant α and the power-law exponent β by fitting (4.7) to the experimental data of the mean radius. The values found for α were around 1.4 for all realizations. For a constant sink flow of dimensionless strength $\widetilde{Q} = \widetilde{R}\dot{\widetilde{R}}$, with $\widetilde{R}$ given by (4.7) it follows that $\widetilde{Q} = \beta\alpha^2\widetilde{\tau}^{2\beta-1}$, where $\widetilde{\tau} = \widetilde{t}_{coll} - \widetilde{t}$. Using $\beta = \frac{1}{2}$ (from the power-law model for the axisymmetric case by [3] and [4]) we find that $\widetilde{Q} = \frac{1}{2}\alpha^2$. With $\alpha \approx 1.4$, as found in our experiments, $\widetilde{Q}_{exp} \approx 1$. The appropriate dimensional scaling of the flow in this work is $Q_{theo} \sim R_{disc}V_0 = 0.02\ (\mathrm{m}^2/\mathrm{s})$, which upon nondimensionalization with the scales R_{disc} and V_0 becomes $\widetilde{Q}_{theo} = 1$, thereby confirming that the mean flow behavior in our experiments is

similar to the axisymmetric case. Values for β were found to lie in the range $0.57 - 0.60$, which is also consistent with previous works (see §4.3.1).

Next, we constructed the theoretical curves for the evolution of the amplitude a_m by introducing the fitted power law into (4.12). The initial condition for a_m was determined from experimental observations and taken at a maximum of the curve; hence, the initial condition for the derivative is $\dot{a}_m = 0$. Figs. 4.6 and 4.7 show the experimental results compared with the theory in semi-logarithmic plots of the mode amplitude versus the mean cavity radius, nondimensionalized using R_{disc} (in these plots time increases from right to left). The amplitude in the theoretical curves neither blows up nor decays; it stays roughly constant in time. This is confirmed by the experimental data, at least during the first oscillations. The amplitude in experimental data drops at the end since we lose the capability to faithfully track the edge of the cavity towards the final collapse.

The oscillation amplitude is roughly preserved, but as $R(t)$ collapses, the relative disturbance $a_m(t)/R(t)$ grows (Fig. 4.8). Since linear oscillations occur only for $a(t) \ll R(t)$, once this condition is not fulfilled non-linear effects overtake the dynamics, adding complexities to the shape of the cavity and increasing the difficulty of tracing its contour. The oscillation period looks constant, but as the horizontal axis is logarithmic, the frequency is actually increasing exponentially (chirping, cf. Eq. (4.13)). This is how the apparent contradiction between the universality of the axisymmetric system and the retention of the azimuthal disturbance at the same time, manifests itself in the dynamics. Part of the information (the mode amplitude) from the initial conditions is encoded and preserved –the cavity 'remembers' the shape that created it– but the chirping of the frequency makes it increasingly difficult to backtrack the evolution of the cavity as the collapse approaches, hence scrambling part of the information at the end [1].

The role of surface tension

We shall now, as an interlude, comment on the role of surface tension. According to the model, surface tension is expected to change the oscillation frequency and amplitude (Fig. 4.8). Nonetheless, we see that experimental data acquired using water ($\sigma_w = 72$ mN/m) and data with the milk solution ($\sigma_m = 47.1$ mN/m) lay on top of each other (Figs. 4.6 and 4.7). At first this might suggest that surface tension plays no role at all. If this were true, the theoretical curve without surface tension would fit these data; but it does not. Instead, the best fit is obtained with the surface tension of the milk solution.

The milk powder dissolved in the experimental tank contains surfactant particles which adhere to the free and initially quiescent surface reducing surface tension. When the disc impacts and penetrates, a fresh free surface is rapidly created on the walls of the cavity, to which surfactants take time to adhere. Thus, for the duration of

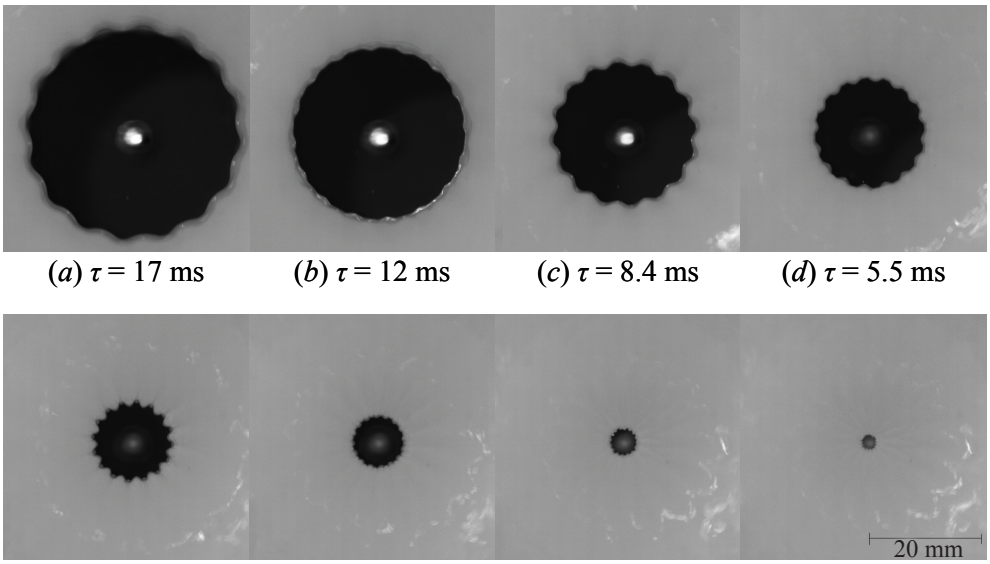

Figure 4.5: Eight snapshots from a collapse with $m = 16$, $R_{disc} = 20$ mm and $a_m = 0.02R_{disc}$. The 16 peaks and valleys from the original shape can be clearly seen (*a*). The amplitude decreases on the way to inversion (*b*) and for an instant has a nearly round shape. The amplitude increases again (*c*) but it has now inverted with respect to (*a*). The process carries on (*d,e*) until we can still see a disturbance but cannot make out the details clearly at our experimental resolution (*f,g*). Finally, the void pinches off (*h*).

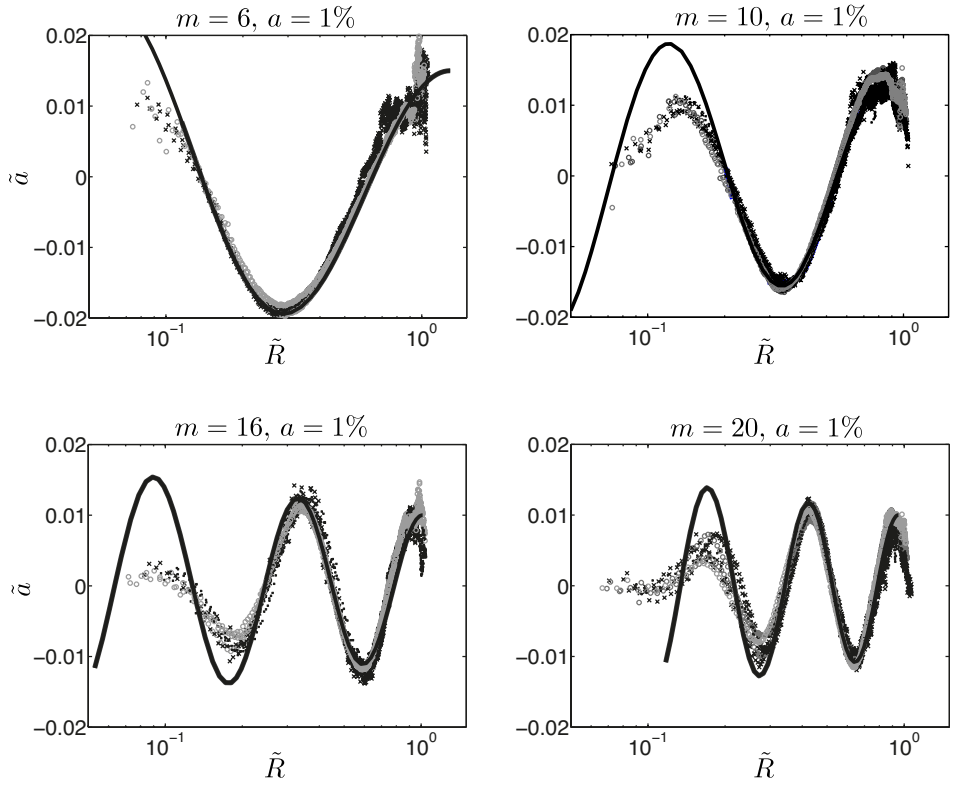

Figure 4.6: Evolution of the dimensionless oscillation amplitude as the radius collapses (time goes from right to left). Results for several different mode numbers with an initial amplitude of 1% of the mean radius. Amplitude is expressed as $\widetilde{a} = a(t)/R_{disc}$. Circles: measurements with milk; crosses: plain water; solid line: theoretical prediction from Eq. (4.12) using the measured surface tension for the milk solution and for a given (dimensionless) mean radius $\widetilde{R} = \alpha(\widetilde{t_{coll}} - \widetilde{t})^{\beta}$ with α and β obtained from experiment.

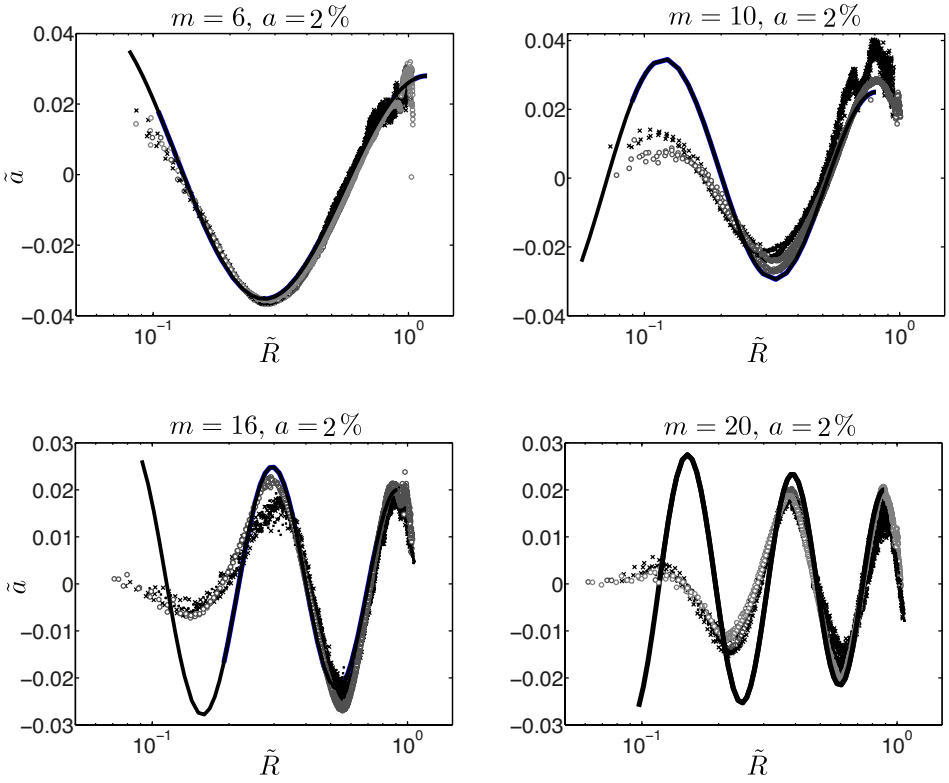

Figure 4.7: Evolution of the dimensionless oscillation amplitude as the radius collapses. Results for several different mode numbers with a slightly higher initial amplitude of 2% of the mean radius. Circles: measurements with milk; crosses: plain water; solid line: theoretical prediction.

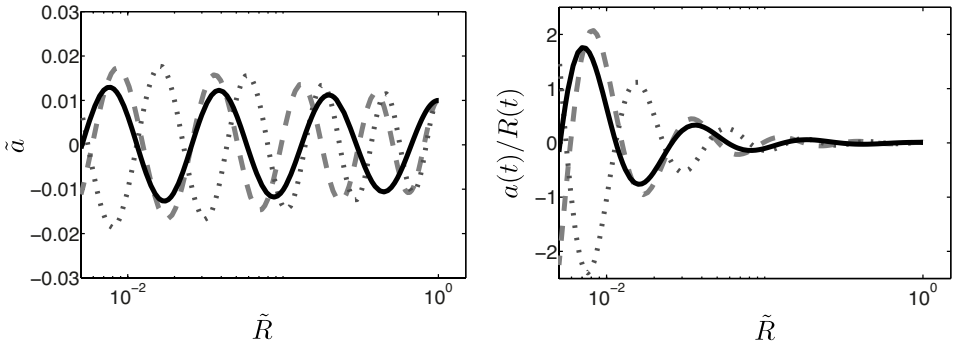

Figure 4.8: Theoretical behavior of the amplitude, normalized by the disc radius, of an $m = 20$, $a_{20}(0) = 0.01R_{disc}$ collapse with different surface tension values (left). — $\sigma = 0$, −− $\sigma_m = 47.1$ mN/m (milk), $\cdots$ $\sigma_w = 72$ mN/m (water). The same plot is shown on the right, but with the amplitude $a_{20}(t)$ divided by $R(t)$, to illustrate the growth of the relative disturbance.

the experiment (~ 100 ms) surface tension must be effectively the same as water, or at least considerably higher than the value measured at the static surface. Nonetheless, from fit of the theoretical model we consistently find that the effective surface tension σ_{eff} must be lower. We now show that this can be interpreted as an effect of the axial curvature, neglected by the two-dimensional model.

Considering the axial curvature as being related to the mean cavity radius $R(t)$ (which is the curvature radius in the azimuthal direction) by a (nearly constant) ratio γ such that $R_{ax}(t) = -\gamma R(t)$, we can write the Laplace pressure jump across the interface as $\sigma\kappa = \sigma\,(1/R(t) - 1/\gamma R(t))$. The opposing signs in the curvatures are due to the hourglass shape of the cavity, which can be seen in Fig. 4.1. The right-hand side of the previous expression can be rewritten as $\sigma_{\text{eff}}/R(t)$ where $\sigma_{\text{eff}} = \sigma\,(1 - 1/\gamma)$, which for any $\gamma > 1$ gives a lower effective surface tension, thereby qualitatively explaining our experimental observations. Figure 4.1 also makes clear that $R_{ax} > R(t)$ and thus indeed $\gamma > 1$. From side-view experimental images, we have observed that during the analyzed part of the collapse, γ varies between 2 and 4. The relation between the effective surface tension used for the theoretical fit (σ_m) and the value for water (σ_w) is $\sigma_m \approx \frac{2}{3}\sigma_w$, corresponding to $\gamma \approx 3$, which is in quantitative accordance with our estimation of the effect of the axial curvature.

The structure of the cavity

We have so far tracked the instantaneous shape of the cavity on a horizontal plane at the pinch-off depth by looking from the top (see [19]). Switching to a side view allows us to see the complete evolution of the cavity at any given time before collapse

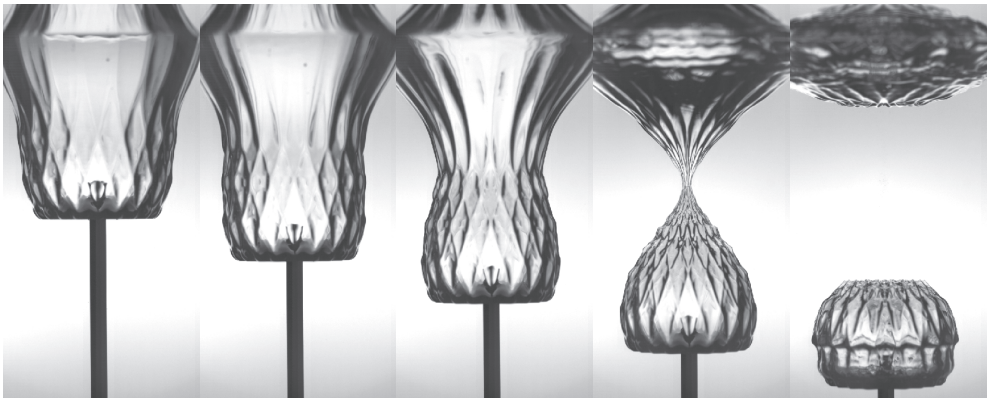

Figure 4.9: Evolution of the collapse of an $m = 20$, $a_{20} = 4\%$ cavity as viewed from the side; $R_{disc} = 20$ mm and $V_0 = 1$ m/s.

in a single snapshot. Figure 4.9 shows four images of a cavity before it pinches off and one afterwards. We can see the walls of the cavity developing a structure that resembles the skin of a pineapple (see [20]). Furthermore, the structure is not lost after collapse and is still clearly seen in the horizontal cavity ripples that form after pinch-off and were studied in detail by [21].

We can reconstruct the shape by combining the model for axisymmetric collapse (4.6) with the equation for the perturbation's amplitude (4.12). First we solve the equation for the mean radial dynamics (4.6), and afterwards introduce the obtained $R(t)$ and its time derivatives in (4.12). Since the models are two-dimensional and decoupled in the vertical direction, the three-dimensional shape is built by solving the equations simultaneously at several depths z as done in [17] for the cylindrical void collapse in dry quicksand. Figure 4.10 shows a parametric plot of the solutions just before pinch-off (4.10a) and an experimental image at the same time (4.10b). We can improve on this result by using the same axisymmetric boundary integral code that was used in [10, 11, 22] to obtain the undisturbed cavity profile $R(z,t)$ which has been found to be in very good agreement with the experimental results [2] and again use equation (4.12) to superimpose the effect of the disturbance in exactly the same manner as described above. This procedure gives the shape in Fig. 4.10(c) which is very similar to the experimental picture, capturing even small details.

4.4.3 Effect of large-amplitude disturbances

Increasing the amplitude of disturbances gives rise to more complex collapses. Such cases cannot be described with models derived from the analysis of a small perturba-

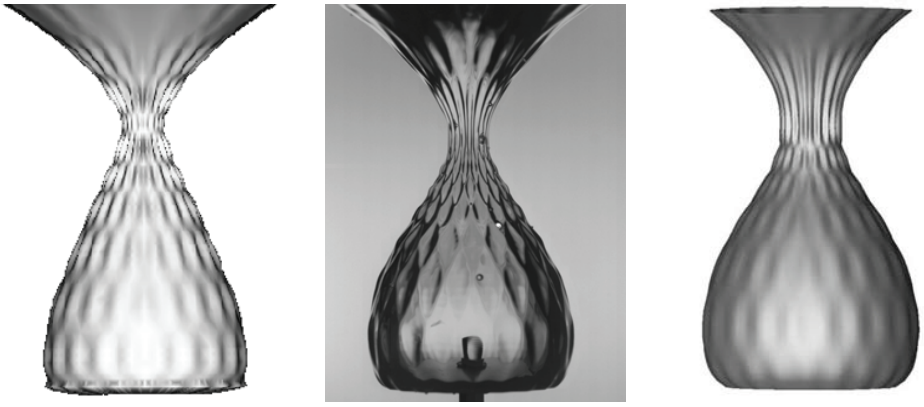

(*a*) (*b*) (*c*)

Figure 4.10: Side view images from experiments and model of $m = 20$, $a_{20} = 2\%$ collapses. The view in (*a*) was obtained through the simultaneous solution of the model for two-dimensional axisymmetric collapse and the one for the amplitude of a disturbance; (*b*) is an experimental image; and (*c*) was obtained by applying the second model to a cavity profile that resulted from a boundary integral simulation of the axisymmetric case. This last method is more effective in reproducing the shape of the cavity, as it captures the axial curvature better.

tion, since there is a clear non-linear behavior. Furthermore, the cavities' evolutions are not the same for all geometries. Phase inversions are still observed and are explained by our continuity argument (§4.4.1) but it is very clear that the cavities no longer close approximately at a single point. Instead, a variety of closure types arise [cf. 15]; for example: pointy and angular structures, finger-like forms, jets in the radial direction, and sub-cavities. Combinations of two or more of these events might take place. The symmetries of the cavities are always preserved, which means that the original single mode perturbation is dominant. However, other modes are excited and, since symmetry is conserved, the excited mode number m changes to an integer multiple of its initial value. On top of this, there are situations in which one value of the angular position θ corresponds to multiple points of the cavity wall, thereby confirming that a simple mode description is no longer applicable.

Some characteristic features

In Fig. 4.11 we compare snapshots from $m = 6$ cavities with different initial disturbance amplitudes $a_6(0)/R(0) = 4\%, 10\%$, and 25%. Each column is a time series of images belonging to one experimental realization. Corresponding snapshots in each series have been taken at equal remaining times to collapse (τ). Whereas the 4% and 10% series are similar, with comparable features occurring at approximately equal times –albeit more pronounced for the larger initial disturbance– the 25% series differs considerably. A closer look at images *a*iii and *b*iii ($\tau = 9$ ms) in Fig. 4.11 reveals pointy, ridge-like jets being formed in singular cusps where the flow converges. For the largest disturbance, this happens only at $\tau = 0.74$ ms (*c*vi). In time, such ridge-like formations can evolve into thicker, finger-like structures (*b*iv).

We found these kind of shapes to be recurrent for most modes and amplitudes but the time at which they happen varies in each case. When they occur too close to pinch-off there is no time for thickening and the collapse takes place with coalescence of the jets in the middle, which tends to happen when the initial amplitude is small (4% or less). Larger amplitudes seem to be more likely to form bigger sub-cavities. Still, the description cannot be generalized. For example, an $m = 6$, $a_6 = 25\%$ cavity will develop wide liquid structures that seem to crawl towards the center (Fig. 4.11*c*i) and eventually it assumes a shape with thin air arms (*c*iv) through which water rushes in to invert the shape; in the end, the collapse (from the top) looks a lot like those with a small initial amplitude. In contrast, an $m = 3$, $a_3 = 25\%$ void will initially form similar thick structures, but they will come in contact with each other, forming large cylindrical sub-cavities (Fig. 4.12).

The disturbance amplitude is roughly conserved during non-linear collapse. We have measured the longest and shortest diameters of cavities through several frames and from that estimated the mean radius and amplitude. The maximum amplitudes found have been of the same order as the impacting shape's. In Fig. 4.11 we can

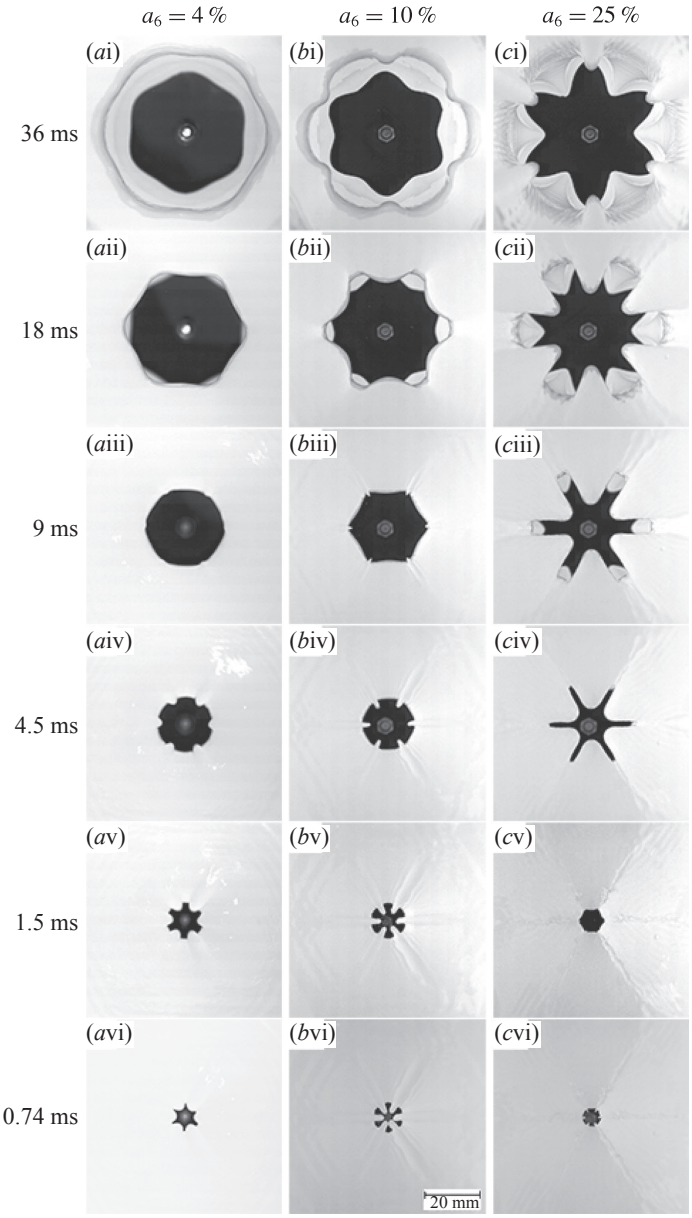

Figure 4.11: Comparison of $m = 6$ collapses with different initial amplitudes. The oscillation periods of disturbances 4 and 10% of the mean radius seem a lot more similar to each other than to $a_6 = 25\%$, where it takes a considerably longer time for the shape to invert. In addition to cusps (*a*vi) and jets (*b*iii,*c*vi), we can see finger-like structures (*b*iv, *b*v) that come into contact to form sub-cavities (*b*vi). When the initial disturbance is very large, such features become very pronounced (series *c*).

see that the oscillation period changes noticeably when varying the initial amplitude. Look at the row where $\tau = 9$ ms and notice how the two cavities on the left (the smaller-amplitude ones) have already started the shape inversion, as made clear by the jets that are being formed, while the rightmost void is still evolving towards the reversal.

Sub-cavity formation

By looking at the last images before the void closes it is easy to convince oneself that it is very unlikely that the cavities will pinch-off at a single point, thus sub-cavity formation must have happened in every case, although it might be extremely short-lived, not appreciable with our imaging capability, or both. The type of sub-cavity formation depends on whether the last inversion takes place early enough to allow for the thickening of the jet-like structures or not; and we have identified several different cases. For all mode numbers, $m+1$ sub-cavities are formed -a central one surrounded by m satellites- except for $m = 2$, where there are just m of these (Fig. 4.3). Sometimes the central sub-cavity is the smallest and collapses right away while the surrounding ones take longer to disappear. In other cases the exact opposite occurs. An example of the first case is shown in Fig. 4.12, where an $m = 3$, $a_3 = 25\%$ void forms four sub-cavities. The center one is gone almost immediately but the other three live long enough to further partition and briefly become six little holes. When we can observe the sub-cavity evolution we always observe a phenomenon like in Fig. 4.12(c) where small jets are impinged from the contact points into all of the remaining sub-voids.

Side view

Another difference with small-amplitude collapses is revealed by looking at the pinch-off from the side. Figure 4.13 shows the pinch-off moment for a round disc and three $m = 6$ discs with amplitudes 4, 10, and 25%. The images in every case are just one frame before the cavity is definitely separated into top and bottom voids. Here the effects of the disconnection not taking place at a single point are manifested in drastic changes of the void's shape at the pinch-off point and accentuation of the top-down asymmetry, which affects the bottom part the most. Figure 4.13(c) shows three air columns with water around them; presumably there are three more columns hidden behind these (see Fig. 4.11$b$vi), depicting a situation where seven sub-cavities were formed, the central one collapsed first, and the remaining six close afterwards simultaneously. In Fig. 4.13(d) we can see that the pinch-off took place in two stages; the "arms" of the cavity closed first, and smaller cavity is left in the center which collapses much like smaller-amplitude voids (see third column in Fig. 4.11).

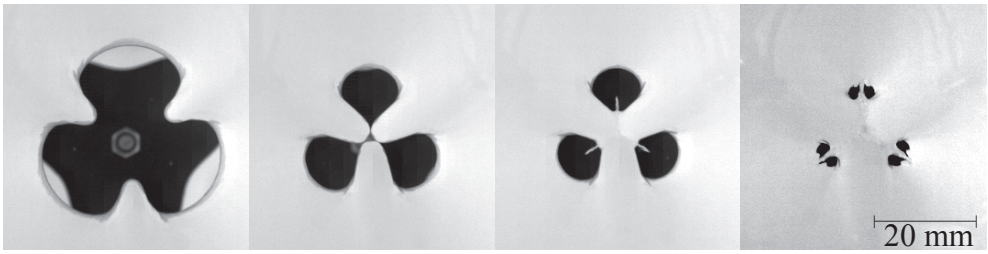

(a) $\tau \approx 12.8$ ms (b) $\tau \approx 5.0$ ms (c) $\tau \approx 3.5$ ms (d) $\tau \approx 0.5$ ms

Figure 4.12: Example of sub-cavity formation for an $m = 3$, $a_3 = 25\%$ collapse. Three large sub-cavities are formed around a smaller central one which quickly disappears. The inward pointing jets in (a) are due to the growth of the initial $m = 3$ disturbance. The jets in (c) are due to the collision (shown in image b) and subsequent convergence of neighboring regions of fluid which lead to six small cavities before closing (d).

4.5 Conclusions

We have experimentally shown that breaking the axial symmetry of an impact-created cavity leads to oscillations of its walls as it collapses. A small, single-mode disturbance with an amplitude of 1 or 2% of the mean radius gives rise to linear oscillations of approximately constant amplitude and increasing frequency. The linear behavior is maintained until the radius shrinks to a size comparable to the disturbance; afterwards, higher oscillation modes evolve and non-linearity sets in. The mean radius evolves in the same way as the axisymmetric, universal case, making this system unique in the sense that it combines universal behavior in the radial direction with memory of initial conditions in the azimuthal direction. Using two-dimensional models for the mean radius and the disturbance's amplitude we can reproduce the three-dimensional shape of the cavities and understand its structure.

Increasing the amplitude of disturbances induces non-linear behavior earlier in the collapse. The structures revealed in these cases attest to the beauty underlying collapse phenomena in fluid dynamics. We have observed a variety of pinch-off types arise and vary with mode numbers and amplitudes. Cavities preserve their symmetries in all cases, but the development of higher harmonics in this system is beyond our mathematical modeling so far.

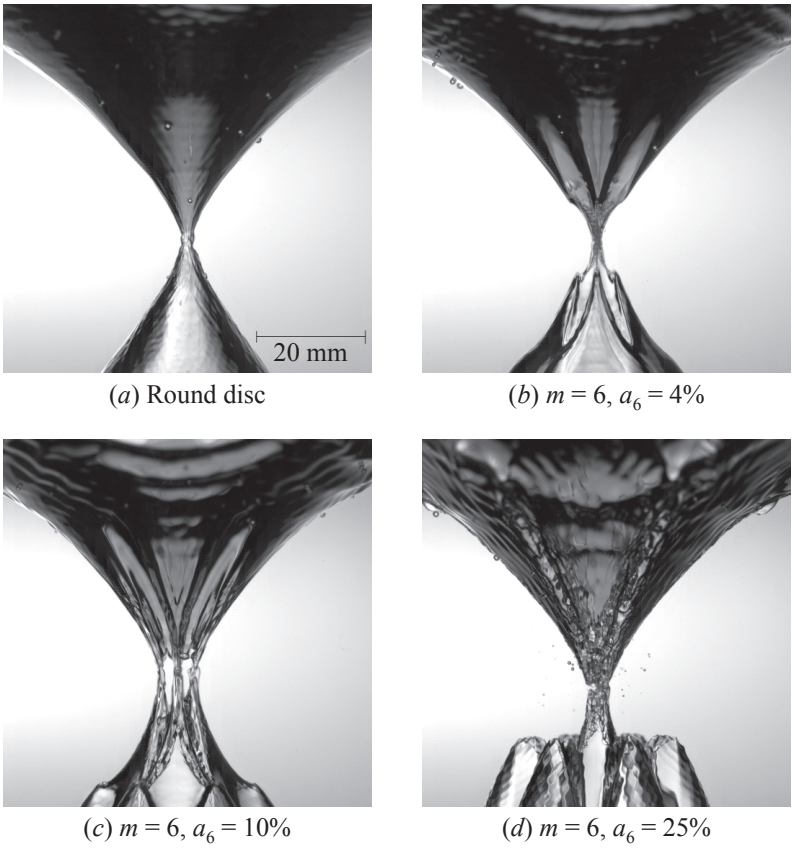

(*a*) Round disc (*b*) $m = 6$, $a_6 = 4\%$

(*c*) $m = 6$, $a_6 = 10\%$ (*d*) $m = 6$, $a_6 = 25\%$

Figure 4.13: Effects of axial symmetry breakup on pinch-off. Perturbed cavities no longer collapse at the same point and, as could be expected, the effects become more pronounced with larger amplitudes. Up-down asymmetry is noticeably accentuated, affecting the void below the deep seal point more.

References

[1] L. E. Schmidt, N. C. Keim, W. W. Zhang, and S. R. Nagel, *Memory-encoding vibrations in a disconnecting air bubble*, Nature Phys. **5**, 343–346 (2009).

[2] R. Bergmann, D. van der Meer, S. Gekle, A. van der Bos, and D. Lohse, *Controlled impact of a disk on a water surface: cavity dynamics*, J. Fluid Mech. **633**, 381–409 (2009).

[3] M. S. Longuet-Higgins, B. R. Kerman, and K. Lunde, *The release of air bubbles from an underwater nozzle*, J. Fluid Mech. **230**, 365–390 (1991).

[4] H. N. Oguz and A. Prosperetti, *Dynamics of bubble growth and detachment from a needle*, J. Fluid Mech. **257**, 111–145 (1993).

[5] J. C. Burton, R. Waldrep, and P. Taborek, *Scaling and Instabilities in Bubble Pinch-Off*, Phys. Rev. Lett. **94**, 184502 (2005).

[6] S. T. Thoroddsen, T. G. Etoh, and K. Takehara, *Experiments on bubble pinch-off*, Phys. Fluids **19**, 042101 (2007).

[7] J. M. Gordillo, A. Sevilla, J. Rodríguez-Rodríguez, and C. Martínez-Bazán, *Axisymmetric Bubble Pinch-Off at High Reynolds Numbers*, Phys. Rev. Lett. **95**, 194501 (2005).

[8] R. Bergmann, A. Andersen, D. van der Meer, and T. Bohr, *Bubble Pinch-Off in a Rotating Flow*, Phys. Rev. Lett. **102**, 204501 (2009).

[9] J. Eggers, M. A. Fontelos, D. Leppinen, and J. H. Snoeijer, *Theory of the Collapsing Axisymmetric Cavity*, Phys. Rev. Lett. **98**, 94502 (2007).

[10] R. Bergmann, D. van der Meer, M. Stijnman, M. Sandtke, A. Prosperetti, and D. Lohse, *Giant Bubble Pinch-Off*, Phys. Rev. Lett. **96**, 154505 (2006).

[11] S. Gekle, A. van der Bos, R. Bergmann, D. van der Meer, and D. Lohse, *Noncontinuous Froude Number Scaling for the Closure Depth of a Cylindrical Cavity*, Phys. Rev. Lett. **100**, 084502 (2008).

[12] S. Gekle, J. H. Snoeijer, D. Lohse, and D. van der Meer, *Approach to universality in axisymmetric bubble pinch-off*, Phys. Rev. E **80**, 036305 (2009).

[13] N. C. Keim, P. Møller, W. W. Zhang, and S. R. Nagel, *Breakup of Air Bubbles in Water: Memory and Breakdown of Cylindrical Symmetry*, Phys. Rev. Lett. **97**, 144503 (2006).

[14] J. M. Gordillo and M. Pérez-Saborid, *Axisymmetric breakup of bubbles at high Reynolds numbers*, J. Fluid Mech. **562**, 303–312 (2006).

[15] K. S. Turitsyn, L. Lai, and W. W. Zhang, *Asymmetric Disconnection of an Underwater Air Bubble: Persistent Neck Vibrations Evolve into a Smooth Contact*, Phys. Rev. Lett. **103**, 124501 (2009).

[16] N. C. Keim, *Perturbed breakup of gas bubbles in water: Memory, gas flow, and coalescence*, Phys. Rev. E **83**, 056325 (2011).

[17] D. Lohse, R. Bergmann, R. Mikkelsen, C. Zeilstra, D. van der Meer, M. Versluis, K. van der Weele, M. van der Hoef, and H. Kuipers, *Impact on Soft Sand: Void Collapse and Jet Formation*, Phys. Rev. Lett. **93**, 198003 (2004).

[18] L. E. Schmidt, *Azimuthal Asymmetries and Vibrational Modes in Bubble Pinch-off*, Ph.D. thesis, University of Chicago (2008).

[19] O. R. Enríquez, I. R. Peters, S. Gekle, L. E. Schmidt, M. Versluis, D. van der Meer, and D. Lohse, *Collapse of nonaxisymmetric cavities*, Phys. Fluids **22**, 091104 (2010).

[20] O. R. Enríquez, I. R. Peters, S. Gekle, L. E. Schmidt, D. van der Meer, and D. Lohse, *Non-axisymmetric impact creates pineapple-shaped cavity*, Phys. Fluids **23**, 091106 (2011).

[21] T. Grumstrup, J. B. Keller, and A. Belmonte, *Cavity Ripples Observed during the Impact of Solid Objects into Liquids*, Phys. Rev. Lett. **99**, 114502 (2007).

[22] S. Gekle, J. M. Gordillo, D. van der Meer, and D. Lohse, *High-Speed Jet Formation after Solid Object Impact*, Phys. Rev. Lett. **102**, 034502 (2009).

5

Splash formation and droplet ejection after disc impact on a liquid surface.*

In this paper we analyze the generation and breakup of the crown splash created when a disc impacts normally onto a free surface. We find that for sufficiently small time after impact, the flow and the free surface in the region close to the disc edge possesses a self similar structure. Moreover, for the case under study here, which correspond to large values of the Weber number $We = \rho R_D V_D^2/\sigma$*, we find that breakup of the splash into a crown only occurs above a threshold Weber number* We_{crit}*. Above* We_{crit}*, the rim formed at the highest part of the splash breaks into drops as a consequence of a Rayleigh-Taylor instability. We identify the transition to this instability by a* local *Bond number, which we define using the downwards acceleration and the rim size. We show that* $Bo_{local} \propto We$*, leading to the value of* We_{crit}*.*

5.1 Introduction

The seemingly straightforward experiment of impacting a solid or liquid object on a liquid surface exhibits many challenges for physical understanding, as was already noticed more than a century ago [1–3]. The creation and collapse of an underwater cavity has been studied extensively for a solid impacting a liquid surface [4–9], as well as the formation of jets resulting from the collapse of this cavity [10–14]. The

*I.R. Peters, J.M. Gordillo, and D. van der Meer, *Splash formation and droplet ejection after disc impact on a liquid surface*, Preprint (2012)

first event that is visible after an object hits a liquid is however the splash. It is formed by the liquid that is moving upwards close to the downwards moving object, which initially can be considered as a Wagner problem, under the condition that the object can locally be approximated as flat [15, 16]. When the object is not locally flat, a splash will be formed provided that certain conditions are fulfilled. These conditions can sometimes be as subtle as the wetting properties of a smooth sphere, as was shown by Duez *et al.* [17].

The approximation of the impact of a flat plate allows for analytical investigations, and is also accessible by experiments and numerical simulations. Self-similar solutions for the case without surface tension ($We \to \infty$) have been found by [18] for the initial stage after impact, whose scaling exponents were already noticed by [19]. Later, this analysis was expanded in order to calculate the hydrodynamic load on a flat surface close to impact [20].

The liquid that is thrown upwards due to the impact of an object develops in a thin sheet with a cylindrical rim on top of it [21][†]. This rim is susceptible to instabilities, which can result in the ejection of droplets. Finding the nature of instabilities that result in the formation of droplets has been the motivation for many studies.

In [23], it is argued that the crown formation is the result of a Richtmyer-Meshkov instability, and the effect of interfacial curvature on liquid rims is discussed in [24], again in the light of Richtmyer-Meshkov and Rayleigh-Taylor instabilities. Deegan *et al.* [25] showed that in a narrow range of parameters, this instability can develop in a very regular pattern, which was later used [26] to experimentally show that the wavelength of this regular pattern agrees with the predicted value corresponding to a Rayleigh-Plateau instability. An analytical study [27] elaborates more on the interplay between the Rayleigh-Plateau and the Rayleigh-Taylor instability. Lister *et al.* [28] specifically isolated the Rayleigh-Taylor instability on a cylinder, tuning the body force normal to the cylinder surface by tilting a liquid cylinder inside a liquid of higher density. Finally, Lhuissier *et al.* [29] found that a Rayleigh-Taylor instability is responsible for the formation of ligaments from the liquid rim observed in bursting bubbles.

Although the Rayleigh-Plateau instability can play a role in the wavelength selection of the instability on the rim [26], it is not likely that this instability is responsible for the *ejection* of secondary droplets. For droplets to be ejected, there needs to be a clear direction to which the instability develops. Assuming that the rim has a cylindrical shape that is attached to the liquid sheet by surface tension, a Rayleigh-Plateau instability would break this cylinder in droplets, but these droplets would still be attached to the sheet. Therefore, a crown would be generated, but we would not see the typical breakup and subsequent ejection of droplets that is observed in experiments.

[†] A similar rim is also observed by Clanet *et al.* [22], where they create a liquid sheet by impacting a liquid jet on a circular target.

By including surface tension into the analysis, we will show that self-similar solutions exists for *any* value of the Weber number, which is then corroborated with the aid of boundary integral (BI) simulations. Also, we show that the downwards moving disc introduces a non self-similar term, for which we provide a correction term. We account for viscous effects, which influence the splash very close to the edge of the disc, by implementing the concept of a virtual origin. After introducing the virtual origin we find an excellent match between the (inviscid) simulations and the experiments, revealing the self-similar properties of the experimentally obtained profiles.

In this chapter we argue that the deceleration of the splash plays a key role in the ejection of droplets from the crown. Droplets will be ejected when the deceleration a minus the gravitational acceleration g becomes more important than the surface tension, which is expressed by the local Bond number at the tip of the splash:

$$Bo_{tip} = \rho(a-g)R_C^2/\sigma, \tag{5.1}$$

with ρ and σ the density and surface tension respectively of water, and R_C the radius of curvature of the rim. We combine experiments, numerical simulations and theory to show that the local Bond number at the tip of the splash is the relevant parameter to predict the transition to the ejection of droplets.

The chapter is organized as follows. In §5.2 we experimentally describe the different spatial regions appearing after the impact of a solid disc against a free surface. In this section we also show that, experimental results can be reproduced by using potential flow numerical simulations. Making use of potential flow theory, we find in §5.3 that the splash region possesses a self similar structure that depends only on *We* for dimensionless times satisfying $t \ll Fr^{3/4}$. In section §5.4 we find the threshold value for the critical Weber number We_{crit} above which the crown breaks up and droplets are ejected. Conclusions are drawn in §5.5.

5.2 Experiments and comparison with boundary integral simulations.

Our experimental setup consists of a disc with radius R_D which we pull down through a water surface at a constant speed V_D using a linear motor. The linear motor ensures that our disc always moves with a constant prescribed velocity. We record the events using a Photron SA1 high speed camera. A more detailed description of the experimental setup can be found in Chapter 4 or [9].

Fig. 5.1 shows the sequence of events occurring immediately after a circular disc impacts perpendicularly with a constant velocity onto a free surface bounding a deep water layer. From these images, it can be appreciated that a circular liquid sheet is ejected out of the liquid bulk all along the perimeter of the disc. The sheet

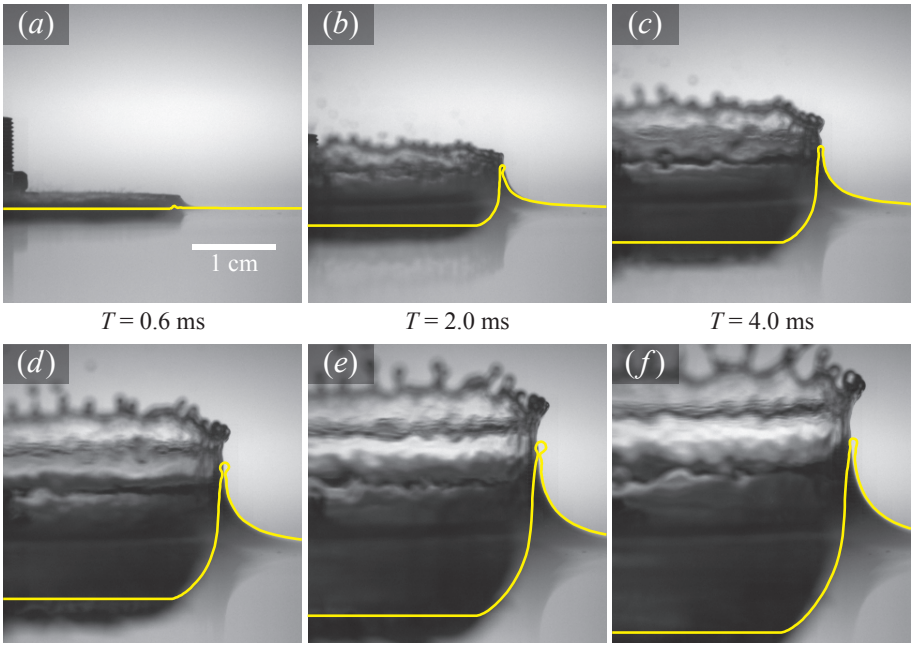

Figure 5.1: Six snapshots of the experiment at times T after disc impact, compared with the corresponding results from the boundary integral simulations (yellow lines). Disc radius is 20 mm, the impact speed is 1 m/s. The agreement between numerical simulations and experiments is excellent once two precisions are made: First, in the numerical simulations, the tip of the splash is unstable and therefore breaks earlier than in experiments. For this reason, the splash in the experiment appears higher than in the simulations. Second, the times corresponding to the experimental profiles are those of the numerical ones plus a constant $T_0 \simeq 0.6$ ms. The existence of this time shift is related to viscous effects at the bottom of the disc and can be retained by simply shifting the origin of the time by a constant value (virtual origin, see text).

then propagates radially outwards, 'informing' the rest of the fluid of the solid body impact. The liquid speeds inside the splash are much larger than the disc impact velocity V_D: indeed, observe that for a given instant in time, the distance traveled out of the liquid bulk by the top part of the liquid sheet is much larger than the distance traveled by the disc. This can also be seen clearly in Fig. 5.4(b), where the height of the splash is much larger than the hardly noticeable distance traveled by the disc. Also notice in Figs. 5.1 and 5.4 that initially the splash develops in time in a region of characteristic length $R_S(T) \ll R_D$ located very close to the disc edge, with R_S the typical distance traveled by the splash, defined in Fig. 5.2. We observe that the liquid sheet can either breakup into drops or just retract into the liquid bulk without breaking, depending on the impact velocity. If V_D is sufficiently large, the rim at the highest part of the sheet breaks into drops, provoking what we refer to as the crown breakup. If, on the contrary, V_D is sufficiently small, surface tension forces and gravity pull back the edge of the rim into the liquid.

Since the impact Reynolds number $Re = V_D R_D/\nu$, where ν indicates the kinematic viscosity of the liquid, is such that $Re \gtrsim O(10^4)$, we expect that viscous effects are confined to thin boundary layers on the bottom of the disc. Thus, the velocity field in most of the liquid volume is expected to be described using a velocity potential and the time evolution of the free surface can be well predicted by using a potential flow boundary integral method of the type used to describe the collapse of cavities [30, 31], the ejection of Worthington jets [14, 32, 33] or the formation of bubbles from an underwater nozzle [34, 35].

In Fig. 5.1 and 5.3 we show that numerical simulations very well reproduce the experiments once the origin of times for the numerical simulations is shifted in time by a quantity T_0, which accounts for the effect of both the gas presence between the plate and the free surface as well as the (small) width of the liquid boundary layer. We conclude from these figures that the liquid flow can be accurately reproduced using a potential flow description.

From both Fig. 5.1 and Fig. 5.2, it is clear that there exist two well-differentiated spatial regions after a solid impacts a free surface. Indeed, using the (dimensional) polar coordinates (R,θ) centered at the disc edge shown Fig. 5.2, we observe that there exists an inner region $R \sim R_S(T) \ll R_D$, where the interface deforms appreciably and an outer region $R \gg R_S(T) \ll R_D$ where the interface hardly changes from its initial position. This experimental fact is essential to theoretically describe the time evolution of the splash, as discussed in detail in the next section.

5.3 Theoretical description of the splash

In this section we will provide a theoretical description for the formation of the splash, part of this analysis is analogous to [18]. From now on, distances, times, velocities

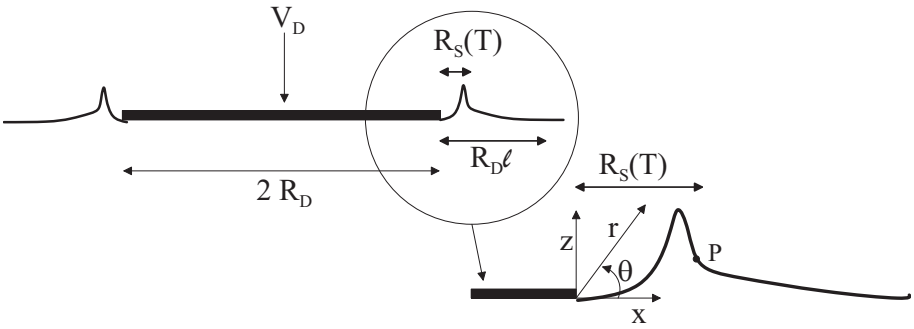

Figure 5.2: Schematic drawing of the impact of the disc and generation of the splash. We define the origin of our coordinate system at the edge of the disc for both the cartesian and polar coordinate system. The point P, which we use as a reference point to measure velocities and lengths in the splash, is defined where the slope of the splash is -1. The splash region $R_S(T)$ indicates at which distance from the edge of the disc the free surface has deformed significantly. ℓ is the nondimensional intermediate length, which is much larger than the $R_S(T)$, but small enough to approximate the flow as 2-dimensional, as explained in § 5.3.

and pressures are made dimensionless using R_D, R_D/V_D, V_D and ρV_D^2 as characteristic length, time, velocity and pressure respectively. We start with deriving the flow field close to the edge of the disc ($r \ll 1$), at times close to the moment of impact ($t \ll 1$), and neglecting the deformation of the free surface (Section 5.3.1). After that, we use this flow field as an outer solution which needs to match the boundary conditions in the region $r \sim r_S$ where we find deformation of the free surface. This matching leads to self-similar solutions, which we confirm by rescaling the profiles that we obtained using the numerical boundary integral method (Section 5.3.2). Finally, we show that the self-similar scalings are fully recovered after we compensate for the downwards motion of the disc, which introduces a non self-similar term (Section 5.3.3).

5.3.1 Flow field

Since $r_S(t) \ll 1$, it is possible to define an intermediate length $\ell(t)$ such that $r_S(t) \ll \ell(t) \ll 1$ at which the height of the interface hardly varies with respect to its initial position. Since $\ell(t) \ll 1$, the velocity potential ϕ at the intermediate region can be described using a two dimensional approach, which satisfies the following equation:

$$\nabla^2\phi = \frac{\partial^2\phi}{\partial x^2} + \frac{\partial^2\phi}{\partial z^2} = 0\,, \tag{5.2}$$

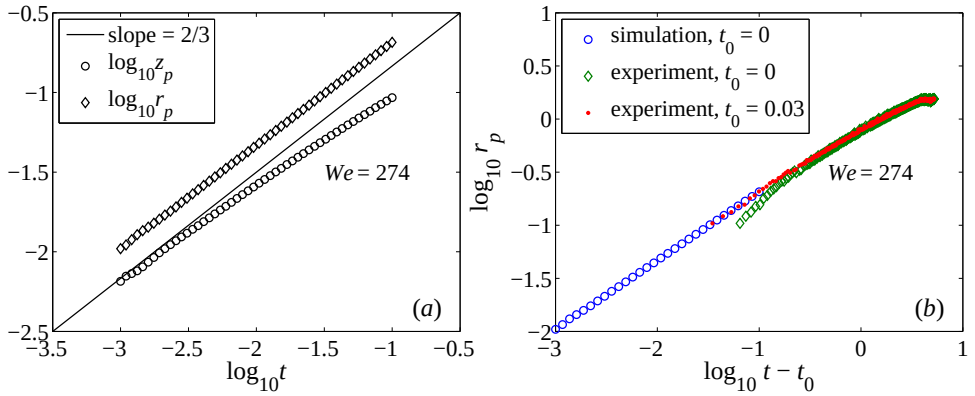

Figure 5.3: (*a*) Time evolution of the horizontal and vertical coordinates of point P. Numerical results reveal that the scaling for both x_p and z_p follows the prediction of equation Eq. (5.15) for $\alpha = 2/3$. The results for z_p slightly deviate from a pure power law due to the real boundary condition at infinity in (5.11), which includes the non self-similar term z, which is due to the downward motion of the disc. (*b*) Comparison between the experiment and the simulation for the radial position of point P. The green diamonds indicate the unmodified experimental data. Once the virtual origin correction t_0 is introduced to account for viscous effects, numerics (blue circles) and experiments (red dots) are in excellent agreement. Deviations from the scaling is expected when $t \sim 1$, because the system can not be approximated as 2-dimensional anymore.

subject to the following boundary conditions:

$$\frac{\partial \phi}{\partial z} = -1 \quad \text{at} \quad z = -t \simeq 0 \quad x < 0\,, \tag{5.3}$$

which is the kinematic boundary condition boundary condition imposed by the downward moving disc,

$$\phi \simeq 0 \quad \text{at} \quad z \simeq 0 \quad x > 0\,, \tag{5.4}$$

denoting the dynamic boundary condition at the free surface[‡], and

$$\phi \to 0 \quad \text{for} \quad \sqrt{x^2+z^2} \to \infty, \tag{5.5}$$

enforcing the fluid far away from the impact to be at rest.

Here, we used the cartesian coordinates (x,z) defined in Fig. 5.2 and have taken into account the observations in Fig. 5.1: that for $t \ll 1$ ($T \ll 20$ ms in Fig. 5.1), the splash develops close to the edge of the disc and that the interface is not appreciably distorted in the intermediate region $r \sim \ell(t)$. The solution to the system (5.2)-(5.5) can be found using standard transformal mapping techniques, yielding the complex flow field

$$\frac{d\omega}{d\zeta} \equiv \frac{\partial \phi}{\partial x} - i\frac{\partial \phi}{\partial z} = i + iA\, r^{-1/2} e^{-i\theta/2} \left(1 + \tfrac{1}{2} r e^{i\theta}\right) \left(1 + \tfrac{1}{4} r e^{i\theta}\right)^{-1/2}, \tag{5.6}$$

where $i = \sqrt{-1}$ and the constant A is determined by matching the velocity field given in Eq. (5.6) with the numerical solution of the velocity field at $r \to 1$, which takes into account the real, i.e., three-dimensional, geometry of the impactor and corresponding flow. Fig. 5.4 shows a comparison for two instants of time, such that $t \ll 1$, between the numerical calculated velocity field and the one given by Eq. (5.6), which is valid in the intermediate region $r \sim \ell(t)$. The agreement is almost perfect when the deformation of the free surface is minimal, as in Fig. 5.4(a). Fig. 5.4(b) shows the influence of the splash region $r \sim r_S$, where there is a clear discrepancy between the approach of Eq. (5.6) and the numerical solution. However, looking at the region $r \sim \ell(t)$, where deformation can be neglected, the agreement is fully recovered.

Now, since the solution (5.6) constitutes the outer boundary condition for the velocity field in the inner region $r \sim r_S(t) \ll \ell(t) \ll 1$, we are interested in the approximation of this equation in the limit $r \ll 1$, which yields,

$$\frac{\partial \phi}{\partial x} \simeq A r^{-1/2} \sin(\theta/2)\,, \quad \frac{\partial \phi}{\partial z} \simeq -1 - A r^{-1/2} \cos(\theta/2) \tag{5.7}$$

[‡]Eq. (5.4) has been obtained by approximating the time-integrated unsteady Bernoulli equation for very small values of t, which can be written as: $\phi \simeq \phi(t=0, z=0, x>0) - \frac{1}{2}|\nabla\phi(t=0)|^2 t \simeq 0$, and taking into account that $\phi(t=0, z=0, x>0) = 0$.

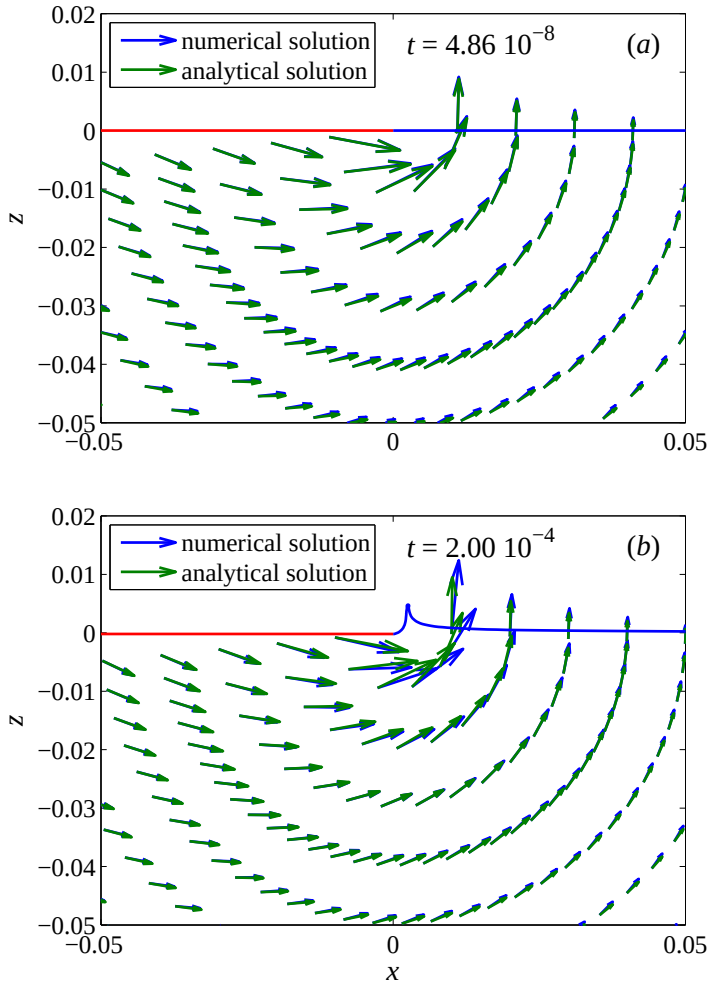

Figure 5.4: The analytical flow field given in Eq. (5.6) compares very favorably with the numerical one once the constant A is set to 0.44. (*a*) At an extremely short time after impact, when the free surface has not yet deformed, the analytical solution agrees with the boundary integral result in the full inner domain where $r \ll 1$. (*b*) At a later point in time we observe that close to the splash region, where the deformation is appreciable, the analytical flow field deviates from the numerical solution. Away from the splash region, the agreement improves again.

and the potential

$$\phi \simeq -z - 2Ar^{1/2}\sin(\theta/2)\,, \tag{5.8}$$

which will serve as a boundary condition to the problem of determining the free surface shape and potential in the splash region.

5.3.2 Self similarity

In the frame of reference moving at the disc velocity, the splash region $r \sim r_S(t) \ll \ell(t)$ can be described by solving the Laplace equation (5.2) subjected to the following boundary conditions at a given point in time:

$$\frac{\partial \phi}{\partial z} = 0 \quad \text{at} \quad z = 0 \quad x < 0\,, \tag{5.9}$$

which is the kinematic boundary condition at the bottom of the disc, and

$$\frac{\partial \phi}{\partial t} + \frac{|\nabla \phi|^2}{2} + \frac{\kappa}{We} + \frac{z}{Fr} = 0 \quad \text{at} \quad z = f(x,t) \quad x > 0\,, \tag{5.10}$$

which is the dynamic boundary condition at the free surface, with $We = \rho V_D^2 R_D/\sigma$ the Weber number and $Fr = V_D^2/(gR_D)$ the Froude number. These equations need to be complemented with the far field velocity potential in the region where the interface is virtually undisturbed, i.e.,

$$\phi \to -2Ar^{1/2}\sin(\theta/2) \quad \text{for} \quad r \to \infty\,. \tag{5.11}$$

$f(x,t)$ defines the position of the free interface, which satisfies the kinematic boundary condition

$$\frac{\partial f}{\partial t} = \frac{\partial \phi}{\partial z} - \frac{\partial \phi}{\partial x}\frac{\partial f}{\partial x} \quad \text{at} \quad z = f(x,t) \quad x > 0\,, \tag{5.12}$$

where

$$f(x, t = 0) = 0 \quad \text{and} \quad f(t, x \to \infty) \to t\,. \tag{5.13}$$

Note that in the Bernoulli equation (5.10) we have used the interfacial curvature

$$\kappa = \frac{\partial^2 f}{\partial x^2}\left(1 + \left(\frac{\partial f}{\partial x}\right)^2\right)^{-3/2} \tag{5.14}$$

to express the pressure jump across the surface, i.e., $p = \kappa We^{-1}$. Since there is no characteristic length scale in the system of equations (5.2) and (5.9)-(5.12), we expect the existence of self-similar solutions of the type

$$\phi = (t - t_0)^{\beta}\,\bar{\phi}\left(\frac{x}{(t-t_0)^{\alpha}}, \frac{z}{(t-t_0)^{\alpha}}\right), \tag{5.15}$$

which we now write as

$$\phi = \tau^{\beta}\bar{\phi}(\chi,\eta), \tag{5.16}$$

with $\chi = x/\tau^{\alpha}$, $\eta = z/\tau^{\alpha}$, and $\tau = t - t_0$. t_0 can be an arbitrary constant, and the shape of the free surface can be expressed as

$$f(x,t) = \tau^{\alpha}F(\chi)\,. \tag{5.17}$$

From the Bernoulli equation (5.10) we find, by comparing the first two terms, that self-similar solutions can only exist if $\beta = 2\alpha - 1$. By matching to the asymptotic solution (5.11) we obtain $2\beta = \alpha$. Combining these two conditions then result in $\beta = 1/3$ and $\alpha = 2/3$. Thus, lengths are expected to scale with $\tau^{2/3}$ and velocities with $\tau^{-1/3}$. Indeed, the system of equations that solve for both $\bar{\phi}$ and F reads, with relative errors $\sim O(\tau^{1/3}) \ll 1$,

$$\frac{\partial^2\bar{\phi}}{\partial\chi^2} + \frac{\partial^2\bar{\phi}}{\partial\eta^2} = 0\,, \tag{5.18}$$

$$\frac{\partial\bar{\phi}}{\partial\eta} = 0 \quad \text{at} \quad \eta = 0\,, \chi < 0 \tag{5.19}$$

$$\bar{\phi} \to -2A\bar{r}^{1/2}\sin(\theta/2) \quad \text{for} \quad \bar{r}\to\infty, \quad \text{with} \quad \bar{r} = \sqrt{\eta^2+\chi^2} \tag{5.20}$$

$$\frac{1}{3}\bar{\phi} - \frac{2}{3}\left(\chi\frac{\partial\bar{\phi}}{\partial\chi} + \eta\frac{\partial\bar{\phi}}{\partial\eta}\right) + \tfrac{1}{2}\left[\left(\frac{\partial\bar{\phi}}{\partial\chi}\right)^2 + \left(\frac{\partial\bar{\phi}}{\partial\eta}\right)^2\right] + \frac{\bar{\kappa}}{We} + \frac{\eta\tau^{4/3}}{Fr} = 0 \tag{5.21}$$

$$\text{at} \quad \eta = F(\chi)\,,$$

with

$$\bar{\kappa} = \frac{d^2F}{d\chi^2}\left(1 + \left(\frac{dF}{d\chi}\right)^2\right)^{-3/2},$$

and

$$\frac{2}{3}F - \chi\frac{dF}{d\chi} = \frac{\partial\bar{\phi}}{\partial\eta} - \frac{dF}{d\chi}\frac{\partial\bar{\phi}}{\partial\chi} \quad \text{at} \quad \eta = F(\chi) \quad \text{and} \quad F(\chi)\to 0 \quad \text{for} \quad \chi\to\infty. \tag{5.22}$$

Note that there is only one term that is breaking the self-similarity of Eqs. (5.18)-(5.22), which is the last term of Eq. (5.21), i.e., $\eta\tau^{4/3}Fr^{-1}$, due to the presence of τ in it. There will therefore exist a self-similar solution whenever $\tau^{1/3} \ll Fr^{1/4} \sim O(1)$, with $Fr = V_D^2/(gR_D)$, i.e., for times shortly after impact, such that the disc has not moved down such an extend that gravity starts to play a role.

Most importantly however, the Laplace pressure term κWe^{-1} in is self-similar. This is because balancing the Laplace pressure term in the Bernoulli equation (5.21) with the inertial terms on the left hand side and inserting the self-similar ansatz

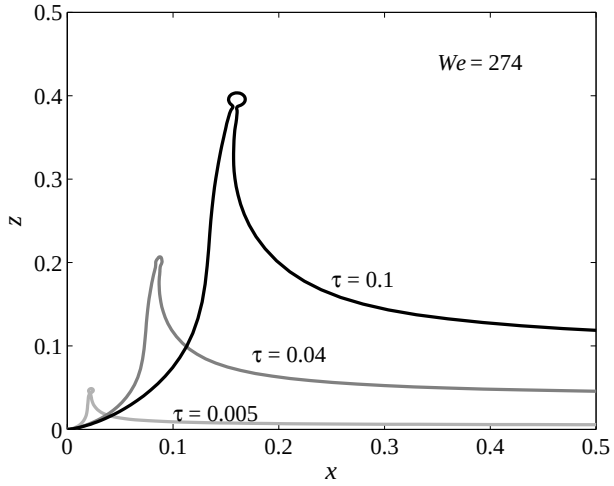

Figure 5.5: Time evolution of the splash region for a given value of the Weber number. The growth of the splash is much larger than the downwards displacement of the disc. For a disc radius $R_D = 20$ mm and an impact speed $V_D = 1$ m/s, the dimensionless times correspond to $T = 0.1$ ms, $T = 0.8$ ms and $T = 2$ ms.

(5.16)-(5.17) will give us $2\beta = \alpha$ and $\beta = 1 - \alpha$, which is solved by exactly the same exponents $\alpha = 2/3$, $\beta = 1/3$ that we have just found by matching to the asymptotic solution of the flow field (5.11). It is this remarkable feature that warrants the existence of self-similar solutions to the system (5.18)-(5.22) for every value of the Weber number *We*.

Clearly, the solution of the system (5.18)-(5.22) needs to be found numerically. It is, however, easier to solve the Laplace equation subjected to the unsteady boundary conditions given by (5.10)-(5.12) and then express the solution in terms of the variables χ, η and F defined in equations (5.16)-(5.17).

Fig. 5.5 shows the solution from the boundary integral method for one specific Weber number at three instances in time, which all are in the regime $\tau \ll 1$ where we expect to find self similar solutions. In Fig. 5.6(*c*) we have rescaled the solution of Fig. 5.5, according to (5.16). Inspecting all shapes in Fig. 5.6(*a-d*), we see that indeed we find self similar solutions for a large range of Weber numbers, that only depend on *We*. Fig. 5.7 shows that for $We \to \infty$ the solution becomes independent of *We*, confirming the results of [18].

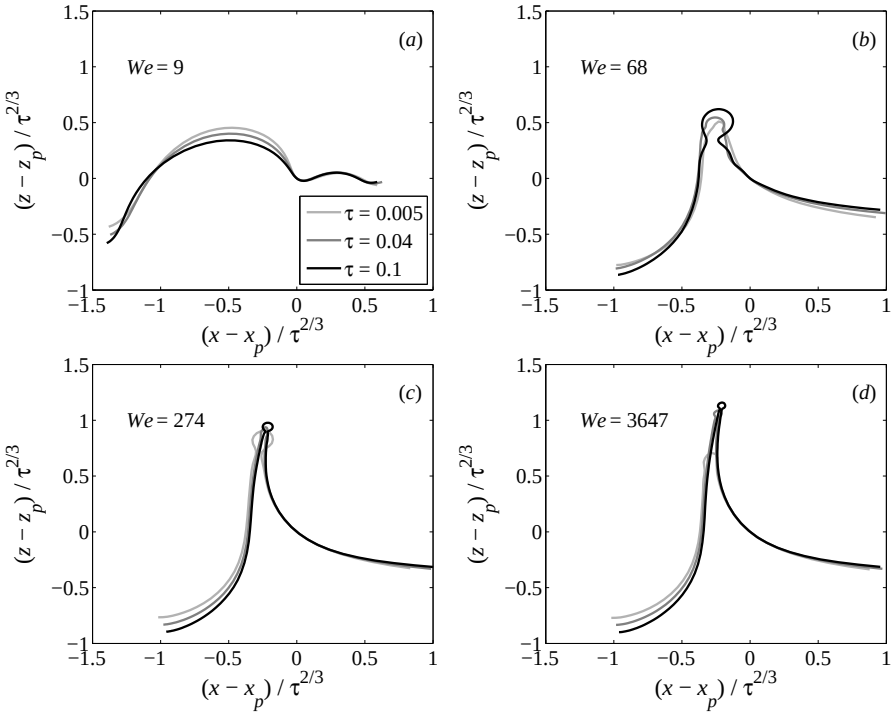

Figure 5.6: Shape of the splash with all distances rescaled by $\tau^{2/3}$ for four different values of the Weber number *We*. Each plot contains three instances in time ($\tau = 0.005$, $\tau = 0.04$, $\tau = 0.1$). The shapes have first been translated such that point P is in the origin of the plots, in order to better show the collapse of the shapes.

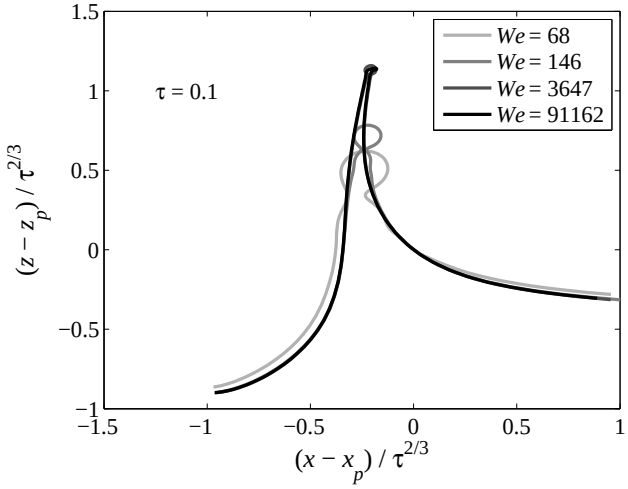

Figure 5.7: Comparison of the self-similar shape of the splash (i.e., with all length scales rescaled by $\tau^{2/3}$) for four different values of the Weber number. Differences in the rescaled shapes are only observed for lower values of the Weber number, see for example the shape for $We = 68$ and $We = 9$ in Fig. 5.6. For high Weber numbers ($We \gtrsim 100$) the rescaled shape hardly changes as a function of We.

5.3.3 Correction for non self-similar terms

From Fig. 5.3 it is clear that the vertical position z_p of point P does not follow the scaling $\tau^{2/3}$ strictly, except in the limit $\tau \to 0$. This difference is caused by the downward motion of the disc, which introduces the non self-similar term t in Eq. (5.13)[§]. To recover the scaling, we need to introduce a constant B_z times τ:

$$(z_p + B_z\tau) \propto \tau^{2/3} \tag{5.23}$$

A similar correction is needed for the vertical velocity u_p at point P:

$$(u_p + B_u) \propto \tau^{-1/3} \tag{5.24}$$

Fig. 5.8(a) shows the position, velocity, and width of the splash at point P. All values become independent of time after the proper rescaling. The same scaling is also valid at the tip of the splash, as seen in Fig. 5.8(b), where we measure the radius of curvature R_C and velocity u_{tip} at the point where the velocity is purely normal to the

[§]A simple way to see why the disc introduces a non self-similar term is by looking at the vertical distance between the disc and the undisturbed free surface: while this distance scales linearly with time (because the disc has a constant velocity) all other lengths scale as $\tau^{2/3}$.

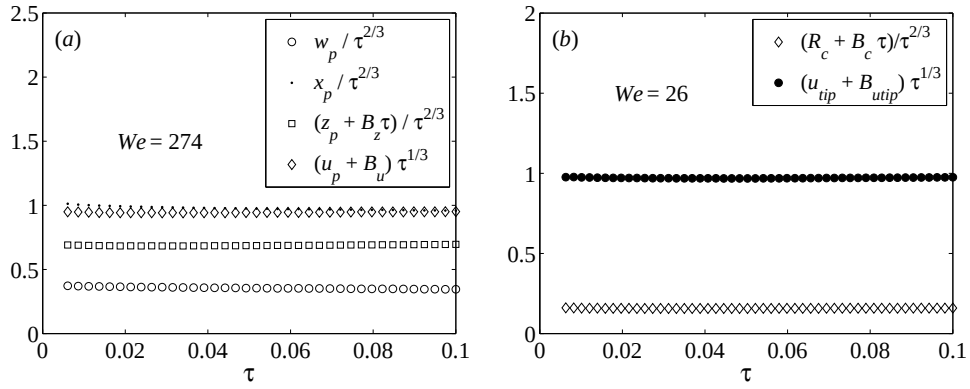

Figure 5.8: Length scales and velocities in the splash rescaled by $\tau^{2/3}$ and $\tau^{-1/3}$ respectively. After proper rescaling, all the plotted values become independent of time, which indicates the self-similar behavior. (*a*) The splash width, position and velocity at the point P as a function of time. As expected from the analysis, the horizontal position x_p of point P as well as the width w_p of the splash at point P are proportional to $\tau^{2/3}$. Due to the term t in Eq. (5.13), a constant B_u is added to the vertical velocity u_p and a term B_z times τ is added to the vertical position z_p of point P (see text). (*b*) Radius of curvature R_C and velocity u_{tip} at the tip of the splash as a function of time, where the tip of the splash is defined as the point where the velocity on the surface is directed purely normal to the surface. Clearly, the same scalings $\tau^{2/3}$ and $\tau^{-1/3}$ that we observe at the point P are also valid at the tip of the splash.

surface: $\phi_n \gg \phi_s$, where the subscripts n and s denote the partial derivative in the normal and tangential direction respectively.

Fig. 5.9 shows the scaling of lengths (*a*) and velocities (*b*) for a wide range of Weber numbers. As expected from the previous analysis, the rescaled values become independent of *We* for large Weber numbers. The same holds for the correction terms: $B_z = 0.56 \pm 0.03$ and $B_u = 0.59 \pm 0.01$ for $We \gtrsim 50$.

5.4 Crown breakup transition

We have provided a scaling for the shape of the splash, and we have shown that the splash possesses a self-similar shape for every value of the Weber number. We will now have a closer look at the breakup of the splash into a crown. With the crown breakup, we are referring to the detachment of ejected droplets from the tip of the splash.

In order to find out when downwards acceleration is large enough to be responsible for a growth of perturbations, we define a local Bond number at the tip of the

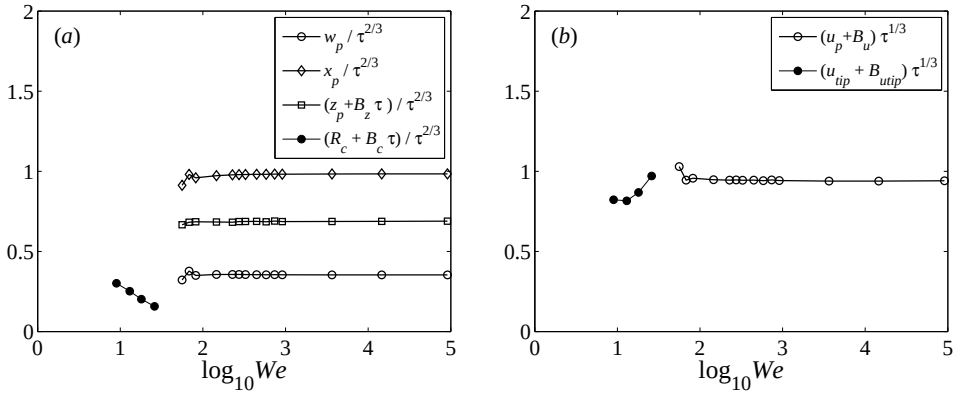

Figure 5.9: (*a*) The positions x_p and z_p, the splash width w_p, and the radius of curvature R_C at the tip of the splash, for different values of the Weber number. (*b*) The vertical velocity u_p and the normal velocity at the tip u_{tip} as a function of *We*. Clearly, all the rescaled values are independent of the Weber number for $We \gtrsim 100$ (see also Fig. 5.7). The rescaled values at the tip are taken at relatively low values of the Weber number, and therefore are not independent of *We*. The solutions are however still self-similar, as is shown in Fig. 5.8(*b*) and Fig. 5.6.

splash using the radius of curvature and the acceleration at the tip, see Eq. (5.1). Bo_{tip} is corrected for gravitational acceleration, which means that if the downwards acceleration is equal to the gravitational acceleration, we consider the acceleration as zero.

The most difficult task is now to determine the local Bond number at the tip of the splash Bo_{tip}. From the numerical simulations, the local Bond number at the tip can be obtained very accurate, but only in an indirect manner for most Weber numbers. The reason for this is that the tip of the splash if unstable in the numerical simulations for $We \gtrsim 30$, as is explained in more detail later in this section. We will show that our indirect measurements are plausible by comparing them to experimental data. The local Bond number at the tip can be determined directly from the experiments, but with a relatively large uncertainty. Both the experimental and numerical method of determining the local Bond number will be explained now.

We obtain experimental values for Bo_{tip} by tracing the tip of the splash, within a time interval T_i with a duration of typically 3 ms, in high-speed movies taken at 5400 frames per second. A second-order fit to the position data versus time gives us the mean acceleration a of the tip. We determine the radius of the rim R_C by measuring it graphically at the beginning and at the end of T_i, giving us a minimum and maximum value for R_C within the time interval. The experimental values for Bo_{tip} are shown in Fig. 5.11 in black symbols. The error bars are obtained by using

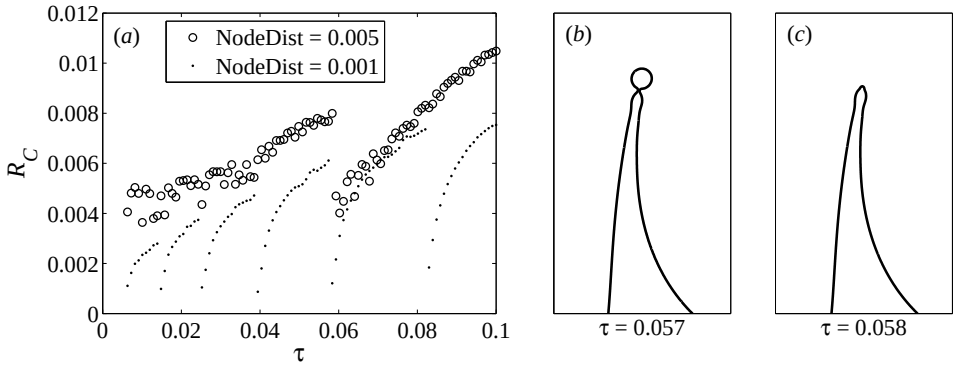

Figure 5.10: Influence of the node density on the tip of the splash, for $We = 274$. (*a*) The radius of curvature R_C at the tip has a minimum value comparable to the minimum distance between the nodes. The radius of curvature increases as the cylindrical rim grows in size, until the rim pinches off, and the radius of curvature starts again at its minimum value. This process is sensitive to the node density, but has no influence on the solution away from the tip, and is not present when *We* is small enough. (*b*) The cylindrical rim at its maximum size before it pinches off, for a minimum node distance of 0.001. (*c*) The same simulation as (*b*), just after the rim has pinched off. The rim is removed from the simulation directly after the pinch-off because it does not represent the physical situation (see text).

the minimum and maximum of R_C, because the radius of curvature is the dominant source of uncertainty, due to the squared appearance of R_C in (5.1).

In the boundary integral simulations, the radius of curvature and acceleration can be determined accurately at any moment of time. The tip of the splash, which is the region in which we are interested, is however only stable in a limited range of low Weber numbers. For higher Weber numbers ($We \gtrsim 30$) a neck is formed below the rim, leading to the pinch-off of the rim (see Fig. 5.10(*b*-*c*)). As soon as the pinch-off has occurred, a new neck forms which pinches off a bit later. This induces a series of pinch-offs in the numerics, which are unphysical for a number of reasons. The first is that, due to axisymmetry, the droplet is tubular, much unlike the droplets that are generated in experiments. The second is that the details of the pinch-off are strongly dependent on the node density that is used in the BI simulations, as is shown in Fig. 5.10, and therefore needs to be qualified as a numerical artifact. The series of pinches influence both the length scale and the acceleration of the tip, such that it is not possible to determine the local Bond number at the tip of the splash for high Weber numbers in the simulations. Although the tip of the splash is unstable, the rest of the splash is not influenced by these numerical artifacts. For this reason, we

determine the local Bond number at point P (see Fig. 5.2), using the width w_p as the length scale and calculate the downwards acceleration at the same point. We will call the local Bond number calculated at point P Bo_P.

In Fig. 5.11, the different methods of measuring the local Bond number are put together. Using the lower reference point P on the splash shows that for $We \gtrsim 100$, the local Bond number is proportional to *We* (blue squares, Fig. 5.11), and we find that it is constant in time. Comparing Bo_P with the experimental values of Bo_{tip} however, shows that the local Bond number is overestimated if we use Bo_P. Calculating the local Bond number in the numerical simulations at different positions on the splash results only in a vertical shift of the points in Fig. 5.11, which shows that we can calculate the local Bond number at different positions by simply multiplying Bo_P by a constant. For Bo_{tip}, we determine this constant to be ~ 0.1 using the experimentally measured local Bond number at the tip of the splash. The local Bond number at the tip that we have deduced from Bo_P is shown in Fig. 5.11 with red circles. Clearly, the transition to breakup into a crown occurs when the local Bond number at the tip of the splash is of order unity.

The proportionality of the local Bond number with the Weber and the independence of time number is not unexpected, because it results from the self-similarity solution that becomes independent of *We* for large Weber numbers. Following the self-similar solutions, we write the acceleration and typical length scale in dimensional form as:

$$a = \frac{V_D^2}{R_D} C_a \tau^{-4/3} \tag{5.25}$$

and

$$R_C = R_D C_R \tau^{2/3}, \tag{5.26}$$

where C_a and C_R are dimensionless constants, independent of time and Weber number. Note that the acceleration and length scale is made dimensional using the disc radius R_D and impact velocity V_D. Substituting (5.25) and (5.26) in (5.1), and using the fact that $a \gg g$ for large values of *We*gives:

$$Bo_{tip} \simeq C_a C_R^2 \frac{\rho V_D^2 R_D}{\sigma} = C_a C_R^2 We, \tag{5.27}$$

clearly showing that the local Bond number is independent of time and proportional to *We*.

Using the proportionality $Bo_{tip} \propto We$ and the crown breakup condition that Bo_{tip} is of order unity around the transition, we can define a condition for the crown breakup transition based on *We* that does not involve the local Bond number. Such a condition is preferable, because whereas the local Bond number is difficult to determine, the Weber number is directly given by the experimental conditions. There indeed exists one critical Weber number We_{crit} above which we always observe breakup

R_D (mm)	We_{crit}	Fr	Re
15	145 ± 5	4.77	12573
20	135 ± 19	2.51	14032
25	134 ± 11	1.59	15630
30	142 ± 19	1.18	17657

Table 5.1: Transition to crown breakup of the splash for different disc radii. The value of the critical Weber number does not differ appreciably with the size of the disc, where the Froude number and the Reynolds number at the transition show a clear dependence on R_D.

of the splash into a crown, as can be seen in table 5.1. The table shows the values of *We*, *Fr* and *Re* at the crown breakup transition[¶]. Note that only the Weber number always has approximately the same value at the transition, showing that the Weber number is indeed the relevant parameter to indicate the transition to crown breakup and droplet ejection.

5.5 Conclusions

We have studied the formation of a splash and the transition to the ejection of droplets after the impact of a disc on a liquid by using boundary integral simulations, experiments and theoretical analysis. Only by combining these three methods, we have been able to analyze the full problem. Although each method has its limitations, either in accuracy, stability or mathematical formulation, each method is able to reveal specific parts of the problem unaccessible by the other methods. Using the overlapping parts however, we accurately demonstrated the validity of each method.

By approximating the time just after disc impact ($t \ll 1$) as a 2-dimensional potential flow problem, we have shown that there exist self-similar solutions of the second kind for any value of the Weber number. These self-similar solutions exist because matching the inertial terms in the unsteady Bernoulli equation to the far-field velocity gives the same scaling powers as matching to the surface tension term. When the Weber number is increased to larger values ($\gtrsim 100$), the shape of the splash becomes independent of the Weber number. Both predictions are confirmed by boundary integral simulations, by rescaling the calculated shapes for a wide range of Weber numbers. We found the correct scaling for both the lengths ($\sim \tau^{2/3}$), and velocities ($\sim \tau^{-1/3}$) at different positions in the splash: at the point P on the edge of the splash, and at the tip of the splash. In the experiments, the same scaling is found

[¶]Clearly, *We*, *Fr* and *Re* can be related after calculating the disc velocity V_D using the disc radius R_D and either of the three dimensionless numbers in table 5.1.

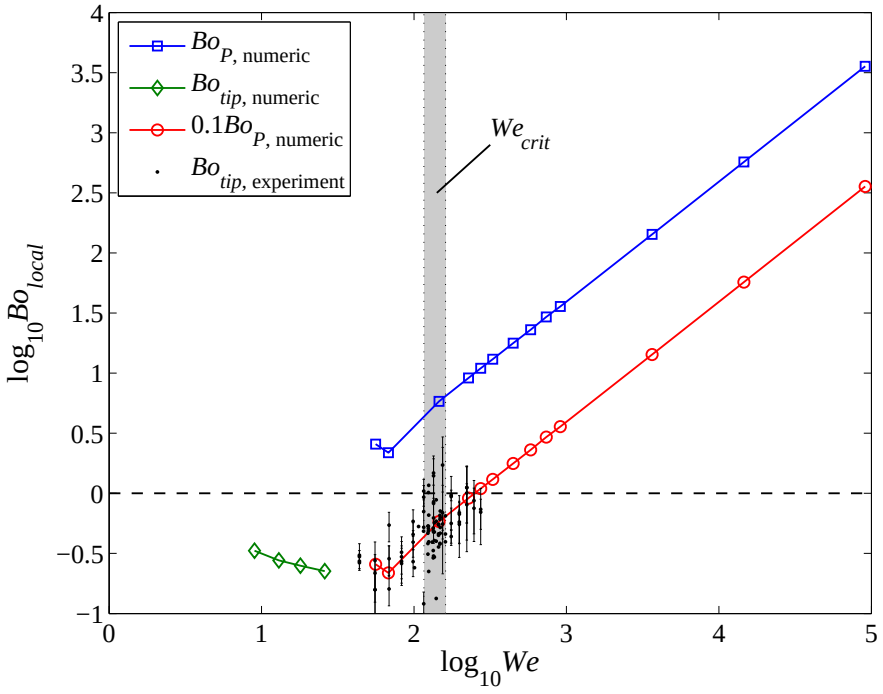

Figure 5.11: The local Bond number measured in different ways as a function of *We*. The blue squares are the local Bond numbers determined in the simulations at point P, the red circles are these same values multiplied by 0.1. This multiplication factor has been found by matching to the experimental values of the local Bond number at the tip (black symbols). The green diamonds show the local Bond numbers measured at the tip of the splash in the BI simulations, which is only possible for $We \lesssim 30$ (see text). The shaded area indicates the range of experimental conditions in which we observe the crown breakup transition. Note that this transition occurs when the local Bond number is of order unity (dashed horizontal line).

after introducing a small time-shift t_0 which accounts for the viscous boundary layer.

We have shown that the transition to droplet ejection (crown breakup transition) is caused by a Rayleigh-Taylor instability, by investigating the acceleration and size of the rim. We experimentally determined that the local Bond number at the tip, based on the downwards acceleration and corrected for gravity, is of order unity at the splash transition. Theoretical analysis predict, and numerical simulations confirm that, Bo_{tip} depends linear on the Weber number for $We \gtrsim 100$. From this linear dependence between Bo_{tip} and We, we have concluded that the splash transition can be identified by a critical Weber number, which we indeed find in the experiments.

References

[1] A. M. Worthington and R. S. Cole, *Impact with a Liquid Surface, Studies by the Aid of Instantaneous Photography*, Philos. T. R. Soc. A **189**, 137–148 (1896).

[2] A. M. Worthington and R. S. Cole, *Impact with a Liquid Surface Studied by the Aid of Instantaneous Photography. Paper II*, Philos. T. R. Soc. A **194**, 175–199 (1900).

[3] A. M. Worthington, *A study of splashes* (Longman and Green, London) (1908).

[4] E. G. Richardson, *The Impact of a Solid on a Liquid Surface*, Proc. Phys. Soc. **61**, 352–367 (1948).

[5] S. Gaudet, *Numerical simulation of circular disks entering the free surface of a fluid*, Phys. Fluids **10**, 2489 (1998).

[6] M. Lee, R. Longoria, and D. Wilson, *Cavity dynamics in high-speed water entry*, Phys. Fluids **9**, 540–550 (1997).

[7] R. Bergmann, D. van der Meer, M. Stijnman, M. Sandtke, A. Prosperetti, and D. Lohse, *Giant Bubble Pinch-Off*, Phys. Rev. Lett. **96**, 154505 (2006).

[8] V. Ducleaux, F. Caillé, C. Duez, C. Ybert, L. Bocquet, and C. Clanet, *Dynamics of transient cavities*, J. Fluid Mech. **591**, 1–19 (2007).

[9] R. Bergmann, D. van der Meer, S. Gekle, A. van der Bos, and D. Lohse, *Controlled impact of a disk on a water surface: cavity dynamics*, J. Fluid Mech. **633**, 381–409 (2009).

[10] M. S. Longuet-Higgins, *Bubbles, breaking waves and hyperbolic jets at a free surface*, J. Fluid Mech. **127**, 103–121 (1983).

[11] J. Hogrefe, N. Peffley, C. Goodridge, W. Shi, H. Hentschel, and D. Lathrop, *Power-law singularities in gravity-capillary waves*, Physica D **123**, 183–205 (1998).

[12] B. Zeff, B. Kleber, J. Fineberg, and D. Lathrop, *Singularity dynamics in curvature collapse and jet eruption on a fluid surface*, Nature **403**, 401–404 (2000).

[13] L. Duchemin, S. Popinet, C. Josserand, and S. Zaleski, *Jet formation in bubbles bursting at a free surface*, Phys. Fluids **14**, 3000–3008 (2002).

[14] S. Gekle, J. M. Gordillo, D. van der Meer, and D. Lohse, *High-Speed Jet Formation after Solid Object Impact*, Phys. Rev. Lett. **102**, 034502 (2009).

[15] H. Wagner, *Über Stoß- und Gleitvorgänge an der Oberfläche von Flüssigkeiten*, Z. Angew. Math. Mech. **12**, 193–215 (1932).

[16] Y.-M. Scolan and A. A. Korobkin, *Three-dimensional theory of water impact. Part 1. Inverse Wagner problem*, J. Fluid Mech. **440**, 293–326 (2001).

[17] C. Duez, C. Ybert, C. Clanet, and L. Bocquet, *Making a splash with water repellency*, Nature Phys. **3**, 180–183 (2007).

[18] A. Iafrati and A. A. Korobkin, *Initial stage of flat plate impact onto liquid free surface*, Phys. Fluids **16**, 2214 (2004).

[19] Y. L. Yakimov, *Effect of the Atmosphere with the Fall of Bodies into Water*, Fluid Dyn. **8**, 679—-682 (1973).

[20] A. Iafrati and A. A. Korobkin, *Hydrodynamic loads during early stage of flat plate impact onto water surface*, Phys. Fluids **20**, 082104 (2008).

[21] A. L. Yarin, *Drop Impact Dynamics: Splashing, Spreading, Receding, Bouncing...*, Ann. Rev. Fluid. Mech. **38**, 159–192 (2006).

[22] C. Clanet and E. Villermaux, *Life of a smooth liquid sheet*, J. Fluid Mech. **462**, 307–340 (2002).

[23] R. Krechetnikov and G. M. Homsy, *Crown-forming instability phenomena in the drop splash problem.*, J. Coll. Int. Sci. **331**, 555–9 (2009).

[24] R. Krechetnikov, *RayleighTaylor and RichtmyerMeshkov instabilities of flat and curved interfaces*, J. Fluid Mech. **625**, 387 (2009).

[25] R. D. Deegan, P. Brunet, and J. Eggers, *Complexities of splashing*, Nonlinearity **21**, C1–C11 (2008).

[26] L. V. Zhang, P. Brunet, J. Eggers, and R. D. Deegan, *Wavelength selection in the crown splash*, Phys. Fluids **22**, 122105 (2010).

[27] R. Krechetnikov, *Stability of liquid sheet edges*, Phys. Fluids **22**, 092101 (2010).

[28] J. R. Lister, R. C. Kerr, N. J. Russell, and A. Crosby, *RayleighTaylor instability of an inclined buoyant viscous cylinder*, J. Fluid Mech. **671**, 1–26 (2011).

[29] H. Lhuissier and E. Villermaux, *Bursting bubble aerosols*, J. Fluid Mech. **696**, 5–44 (2012).

[30] M. Longuet-Higgins and H. Oguz, *Critical microjets in collapsing cavities*, J. Fluid Mech. **290**, 183–201 (1995).

[31] S. Gekle, A. van der Bos, R. Bergmann, D. van der Meer, and D. Lohse, *Noncontinuous Froude Number Scaling for the Closure Depth of a Cylindrical Cavity*, Phys. Rev. Lett. **100**, 084502 (2008).

[32] S. Gekle and J. M. Gordillo, *Generation and breakup of Worthington jets after cavity collapse. Part 1. Jet formation*, J. Fluid Mech. **663**, 293–330 (2010).

[33] J. M. Gordillo and S. Gekle, *Generation and breakup of Worthington jets after cavity collapse. Part 2. Tip breakup of stretched jets*, J. Fluid Mech. **663**, 331–346 (2010).

[34] H. N. Oguz and A. Prosperetti, *Dynamics of bubble growth and detachment from a needle*, J. Fluid Mech. **257**, 111–145 (1993).

[35] J. M. Gordillo, *Axisymmetric Bubble Pinch-Off at High Reynolds Numbers*, Phys. Rev. Lett. **95**, 194501 (2005).

6

The multi-fluid impact experiment*

When a round disc impacts on a water surface, a cavity is created that collapses under the influence of hydrostatic pressure, leading to a pinch-off where two jets are formed, one shooting upwards, and one downwards. If the water surface is covered with a layer of oil, the same is true for the cavity, providing a clear picture of what happens within the liquid after the pinch-off: The jet initially exists of only oil, in agreement with earlier theoretical predictions [1]. When the jet develops further and becomes thicker, the jet is composed mainly of water, but with a stable core of oil that extends all the way down to the bulk. We explore how the oil-water contents of the jet depends on the initial thickness of the oil layer and the Froude number.

In a second set of experiments we prepare a system where no air is involved, only oil and water. By pulling down the disc starting from the oil-water interface, we observe universal shapes for $Fr^* \to \infty$, where Fr^* is the Froude number corrected for the reduced density difference between the two phases.

6.1 Introduction

The splashes and jets that are formed after the impact on a liquid surface have been observed and photographed by Worthington at the end of the nineteenth century [2]. In search of explanations for the observed phenomena, the experimental observations were soon extended to below the liquid surface [3], which led to the conclusion that

*I.R. Peters, M. Madonia, D. Lohse, and D. van der Meer, *The multi-fluid impact experiment*, Preprint (2012)

the jet is formed due to the collapse of a surface cavity. Besides observing the shape of the cavity, which obtained enormous impulse due to the development of digital high-speed imaging techniques, the availability of particle image velocimetry (PIV) has made it possible to directly measure the velocities in the bulk of the liquid [4–6].

There is however little experimental information on the origin of the jet that forms after the collapse of the above described cavities. The behavior of jets long *after* they have formed has been studied extensively [7], most specifically their breakup into droplets, but the formation of the jet we examine has only been studied numerically and theoretically where experiments mainly were used for verification [1, 8, 9]. The lack of direct experimental information on the structure and formation of the jet is possibly explained by the numerical simulations of [1], where it was found that the liquid in the jet originates from a thin layer on the surface of the collapsing cavity. This is difficult to demonstrate using standard PIV techniques, which are not suitable for visualization close to free surfaces. Reflections of laser light on the free surface make it difficult to visualize tracer particles close to a free surface, and in addition, tracer particles tend to cluster on the free surface. Oil however, can easily be used as a tracer liquid at free surfaces, as it naturally spreads evenly over a free surface provided that the oil layer is sufficiently thick.

Besides fundamental interest in jet formation, the behavior of immiscible liquids is important for applications like flow-focusing devices [10, 11], where a liquid jet breaks up surrounded by a co-flowing liquid. The behavior of oil floating on water is of interest for cleaning techniques after oil spills on the ocean [12], or, when removing the oil is not possible, to enhance dispersion of the oil without the use of additional chemicals [13]. One might also wonder what happens to the spilled oil when it starts to rain, and millions of droplets impact the floating oil layer. Even certain geophysical flows, for example during solidification in the early stages of development of planets, can be understood using the behavior of two immiscible liquids [14, 15].

We will report the results from two kinds of experiments in this chapter. After introducing the experimental setup and the relevant experimental parameters in Sec. 6.2, we start with the impact on a layer of oil floating on a water surface in Sec. 6.3. This experiment provides excellent experimental insight into the process of jet formation and the behavior of the liquid in the bulk after the pinch-off. More specifically, we will provide direct experimental proof of the model for jet formation after cavity collapse proposed in [1], described above. In agreement with this model, our experimental results confirm that the stagnation point flow after the pinch-off is very weak. In Sec. 6.4, we report experiments where we start with the disc at the oil-water interface. When the disc moves down, it drags along the oil, which then obtains a particular profile. We observe how these profiles depend on the velocity of the disc, and find that for high velocities, there exists a universal profile. We conclude

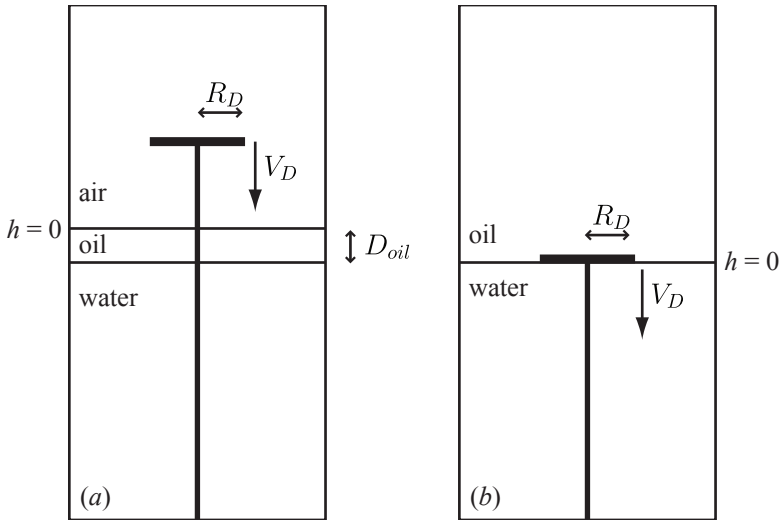

Figure 6.1: Schematic view of the experiment, with disc radius R_D and disc velocity V_D. In (a) we impact the disc on a layer of oil of thickness D_{oil} that is floating on a deep layer of water. For this situation we define the vertical coordinate $h = 0$ at the undisturbed oil-air interface. In (b) we start with the bottom of the disc at rest at the interface between a deep layer of oil on a deep layer of water, after which we pull down the disc at constant speed V_D. We define $h = 0$ at the undisturbed oil-water interface.

in Sec. 6.5

6.2 Experimental setup

The experimental setup consists of a water reservoir with a cross section of 15 cm by 15 cm and a height of 50 cm. A linear motor that is mounted below the tank pulls a disc through the water surface at a constant speed, by means of a thin rod connecting the linear motor with the disc. The disc is accelerated with a maximum acceleration of 42 $\mathrm{m/s^2}$ until the desired velocity V_D is reached. The events are recorded with a Photron SA2 high speed camera at frame rates ranging from 1 to 8 kHz. Our main control parameter is the Froude number, which is defined as the disc speed V_D, made dimensionless by the disc radius R_D and the gravitational acceleration g:

$$Fr = \frac{V_D^2}{gR_D}. \tag{6.1}$$

In the case where we pull down the disc from the oil-water interface, we have to adjust the Froude number because of the decreased effect of gravity due to the small

density difference between the oil and the water phase. The effective Froude number Fr^* can be obtained by replacing g in (6.1) by the effective gravitational acceleration g^*, as one would use to determine the wave speed of gravitational waves on a density interface $g^* = g(\rho_w - \rho_o)/(\rho_w + \rho_o)$ [16], yielding

$$Fr^* = \frac{V_D^2}{gR_D}\left(\frac{\rho_w + \rho_o}{\rho_w - \rho_o}\right), \tag{6.2}$$

where ρ_w and ρ_o are the densities of water and oil respectively. In our experiments we use sunflower oil, which has a density $\rho_o = 900$ kg/m^3 and viscosity $\nu \sim 50 \cdot 10^{-6}$m^2/s. Next to demineralized water we use a solution of table salt in water to increase the density of the water phase. We dissolved 1.0 kg of table salt in 5000 ml water, resulting in $\rho_{sw} = 1140$ kg/m^3.

6.3 Impact on a layer of oil

We impact a disc on an oil layer floating on a deep layer of water. In Fig. 6.2 we compare a series of snapshots from an impact experiment on pure water with the corresponding ones from an impact on water covered by a layer of oil with thickness $D_{oil} = 15$ mm[†]. We use the same disc ($R_D = 20$ mm) and impact speed ($V_D = 1.0$ m/s) in both cases. We first observe a splash (Fig. 6.2(*b*i)), where in the second experiment (Fig. 6.2(*b*ii)) the oil is thrown up around the edge of the disc [18]. Subsequently, a surface cavity is formed which collapses under the influence of hydrostatic pressure (Fig. 6.2(*b-d*)). In the oil-layer experiment the surface of this cavity is covered with a thin layer of oil, which is difficult to discern in Fig. 6.2(*c*ii), but can be clearly distinguished in Fig. 6.2(*d*ii): The entrained air bubble pinches off and is surrounded by oil.

We can estimate the typical thickness of the oil layer that is covering the cavity in the expansion phase, by taking a cross-section at the pinch-off depth and assuming that flow is directed mainly radially in the time interval between maximum expansion and pinch-off [5]. The oil layer that sits on the cavity surface needs to be thinner when the radius of the cavity is larger, because the surface of the cavity that it covers is larger. This can be quantified using volume conservation together with the assumption of purely radial flow. First, we measure the radius of the oil R_{oil} at the pinch-off depth at the moment of pinch-off. In Fig. 6.2(*d*ii), $R_{oil} = 5.2$ mm. At the same depth, the cavity reached a maximum radius $R_{max} = 26.4$ mm. The thickness of the oil layer at that point is then:

$$D_{film} = \sqrt{R_{max}^2 + R_{oil}^2} - R_{max} \tag{6.3}$$

[†]One may note from Fig. 6.2 that the shape of the cavity is very similar for the experiments with pure water and with an oil layer. Only the depth where the pinch-off takes place has shifted and the shape of upper half of the cavity at pinch-off is slightly different.

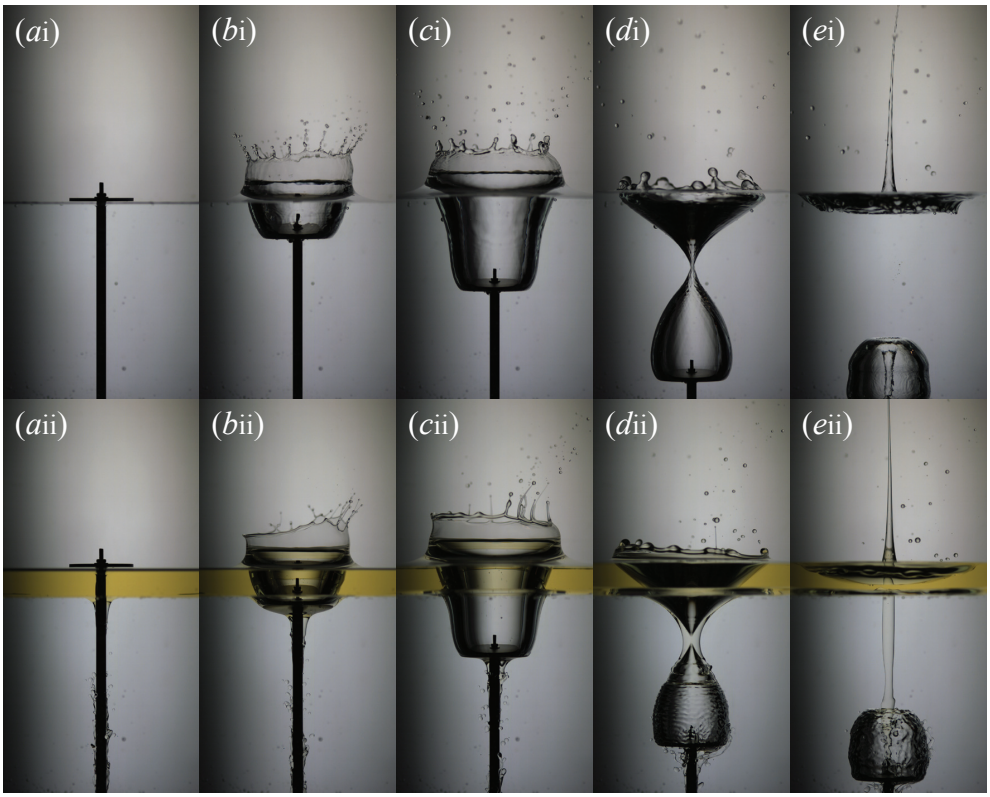

Figure 6.2: Snapshots of two experiments: (*a*i-*e*i) impact on a water surface, (*a*ii-*e*ii) impact on an oil layer covering a water surface. For both experiments, $R_D = 20$ mm and $V_D = 1.0$ m/s. The thickness of the oil layer is $D_{oil} = 15$ mm (due to the perspective view, the layer appears slightly thicker in the image). (*a*) The disc moves down at a constant speed of $V_D = 1$ m/s. (*b*) A splash is formed, which is similar in both cases. (*c*) A cavity is created, which for the second experiment is covered with a layer of oil on the inside. In this case, ripples with a short wavelength appear suddenly at the oil-water interface at $t \approx -68$ ms and onwards. (*d*) We define $t = 0$ when the entrained air pinches off. In the second experiment, the pinch-off point on the axis of symmetry is surrounded by oil, preventing water to contact the air. (*e*) A thin jet shoots up, which in the second experiment consists only of oil coming from the surface of the cavity. In the bulk there is a stable entrained column of oil, indicating the absence of radial flow in the stagnation point (= pinch-off point) area after the pinch-off.

For the experiment in Fig. 6.2 we find $D_{film} \approx 0.5$ mm.

Waves with a typical wavelength of $\lambda \approx 2.5$ mm appear suddenly at $t \approx -47$ μs, visible in Fig. 6.2(*d*ii) (the moment of appearance depends on the experimental conditions). These waves are most probably capillary ripples concerning the condition $\lambda \ll 2\pi\ell$ [19], in which ℓ is the capillary length similar to that of water[‡]. It is not clear which event has triggered these waves, possible explanations could be found in the breakup of the oil layer on the cavity surface. This layer is likely to become thinner as the length of the cavity increases and can become unstable if the layer is thin enough. The origin of these waves is however not a subject of this paper, and in all the cases that we study, the waves only exist below the pinch-off depth and are not influencing our measurements.

Before the pinch-off, the flow around the cavity is mainly radial, with a strongly increasing velocity towards the moment of pinch-off [5]. After the pinch-off, the radial flow suddenly is converted into a vertical flow, resulting in the formation of a thin jet. Looking at the pure water experiment (Fig. 6.2(*e*i)), it remains unclear where the liquid in the jet originates. However, in Fig. 6.2(*e*ii) we observe that the jet initially consists of only oil, from which we can conclude that the jet is formed from liquid very close to the surface of the cavity. The dynamics of the jet formation becomes even more clear when looking in the bulk, where a stable cylinder of oil is entrained. The stability of this oil cylinder as seen in Fig. 6.2(*e*ii) indicates that directly after the pinch-off, there is no more radial flow around the pinch-off point, and that the (radial) inflow into the jet is localized near the base of the jet. The observations that the jet is formed from the surface of the cavity and the non-persistent radial flow confirm the model for jet formation of Gekle *et. al* [1]. This is in contrast to the hyperbolic jet [8], where liquid from the bulk would enter the jet.

Only a considerable amount of time after the jet starts to form, water is joining into the jet. Nevertheless, in the center of the jet we always observe a stable core of oil, which is connected to the cylinder of oil observed in the bulk. Fig 6.3 shows the composition of the jet after the water as joined for two different values of D_{oil}. The upper part of the jet still consists of only oil, which connects to the oil core in the lower part of the jet. The moment at which the water joins into the jet depends on the initial thickness of the oil layer D_{oil}, which is reflected in the thickness of the jet when the water joins. If D_{oil} is large enough, a layer of oil on the outside of the jet can be observed as shown in Fig. 6.3(*a*). For smaller D_{oil}, Fig. 6.3(*b*), this layer is either too thin to observe, or has disappeared due to breakup of the oil film [20, 21]. Finally, if the initial oil layer is thin enough, a Rayleigh-Plateau instability develops on the oil cylinder [10, 22] inside the water phase, which eventually leads to the formation of oil droplets inside the jet (Fig. 6.4).

[‡]Strictly speaking, the condition $\lambda \ll 2\pi\ell$ [19] should be modified because gravity is not directed perpendicular to the disturbance. Such a modification would however be in favor of the capillary waves.

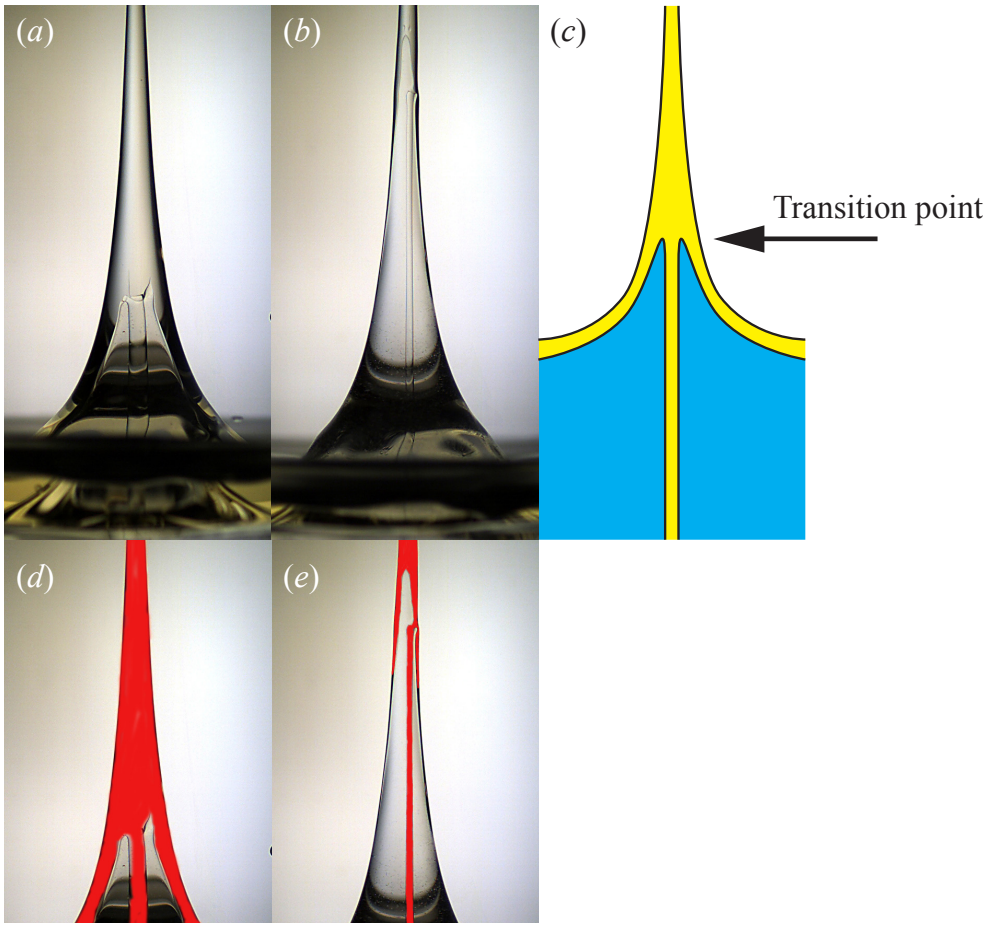

Figure 6.3: The composition of the jet after the water has joined, for (*a*) $D_{oil} = 15$ mm and (*b*) $D_{oil} = 10$ mm. Both images are taken 176 ms after the disc has impacted oil surface, $R_D = 20$ mm. The upper part of the jet contains only oil, the lower part has an oil core in the center, which is surrounded by water. For the thicker oil layers (*a*), the outside of the jet is clearly covered by oil. For thinner oil layers, it is not clear whether the lower part of the jet is covered with an oil layer on the outside (see text). (*d*) and (*e*) are the same as (*a*) and (*b*), only colored red to indicate where the oil is. (*c*) A schematic view of the jet composition: The oil in the upper part of the jet is connected to the undisturbed oil layer far away via the (thin) oil layer on the surface of the jet. The oil core in the center of the jet extends all the way into the bulk, as is visible in Fig. 6.2(*e*ii).

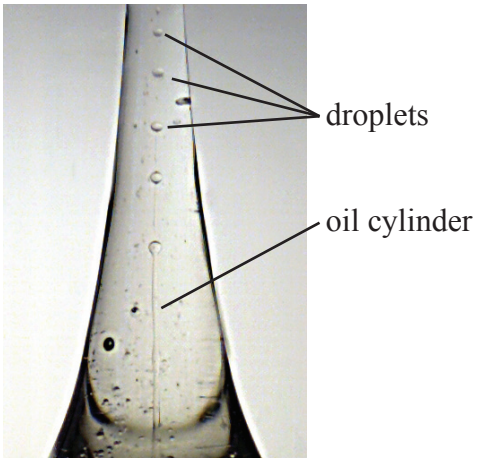

Figure 6.4: Snapshot of a jet 0.18 s after impact on a thin layer of oil ($D_{oil} = 6.5$ mm, $R_D = 20$ mm). The oil core in the center of the jet breaks up into droplets due to a Rayleigh-Plateau instability.

6.3.1 Influence of oil layer thickness

As shown in Fig 6.3, at some point in time after the pinch-off water will start entering the the jet and moving upward with the rest of the jet. This leads to a structure as sketched in Fig. 6.3(c) where the oil-water interface of the core of the jet connects to the oil-water interface at the free surface. The thicker the initial oil layer, the later the water will join into the jet. To quantify the amount of water that joins the jet, we measure the radius of the jet R_{jet} at this joining point at that moment in time at which the joining point has reached a height of two disc radii above the initial free surface of the oil. A small value of R_{jet} indicates the presence of water in an early stage of jet development and, consequently, that a larger fraction of the jet consists of water at any fixed moment in time. Figure 6.5(a) shows how R_{jet} depends on the oil layer thickness D_{oil}, where both length scales are normalized by the disc radius. For $D_{oil}/R_D \lesssim 0.6$, R_{jet} grows linear with the oil layer thickness. This relation breaks down for thicker layers, which could be related to the limited growth of the jet due to gravity: For $D_{oil}/R_D = 0.875$, the upwards motion of the jet is stopped and the jet falls back under the influence of gravity before the water phase has reached the point where we measure the jet radius. During this reversal of the jet movement, one can expect that the inertial stretching of the jet [7] is decreased due to gravity, resulting in thickening of the jet. This then would explain why the growth of R_{jet} as a function of D_{oil} increases when the maximum thickness is approached. In Fig. 6.5(b) we plot the time T_{jet}, normalized by the gravitational time scale $T_g = (R_D/g)^{1/2}$, against the oil layer thickness. We defined T_{jet} as the time between the moment of initial formation

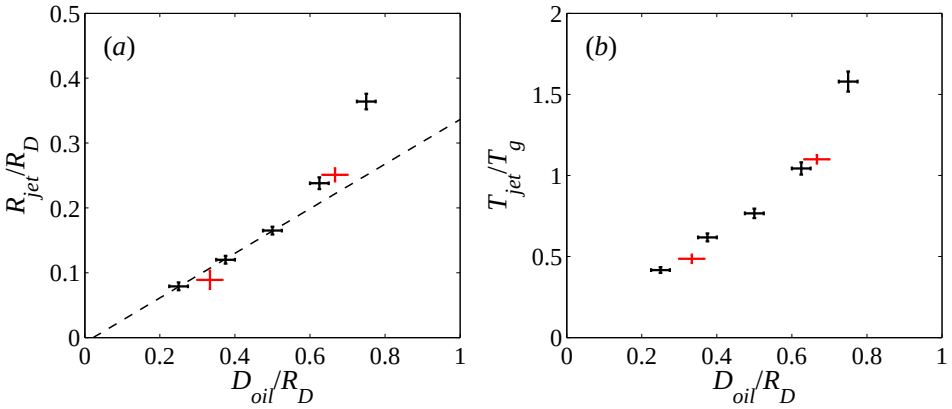

Figure 6.5: (*a*) The radius of the jet R_{jet} at the point where water is joining the jet, measured at $h = 2R_D$ for a Froude number $Fr = 5.1$. R_{jet} initially increases approximately linear with the oil layer thickness D_{oil}. The dashed line is a linear fit to the lower three black data points. For $D_{oil}/R_D = 0.875$, the water does not reach the height $h = 2R_D$ due to gravity. Black symbols are obtained with $R_D = 20$ mm ($V_D = 1.0$ m/s), the red symbols are obtained with a smaller disc $R_D = 15$ mm ($V_D = 0.87$ m/s). (*b*) The time T_{jet} it takes for the water inside the jet to reach the height $h = 2R_D$, divided by the gravitational time $T_g = (R_D/g)^{1/2}$. T_{jet} and T_g are of comparable magnitude, indicating the importance of gravity.

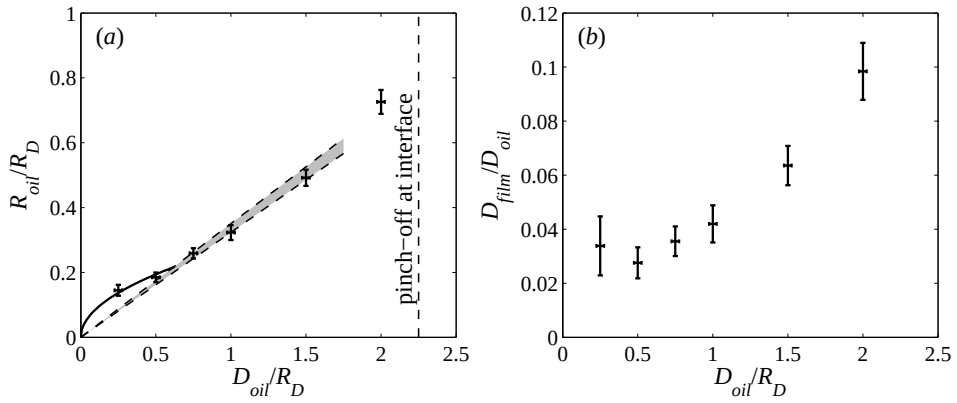

Figure 6.6: (*a*) The radius of the entrained oil column R_{oil} at the moment of pinch-off as a function of the oil layer thickness D_{oil}. We measure the radius R_{oil} at the same depth as where the pinch-off takes place. The impact speed V_D was 1 m/s and the disc radius R_D was 20 mm for all experiments ($Fr = 5.1$). The pinch-off depth coincides with the oil-water interface when $D_{oil} \approx 45$ mm for this set of experiments, indicated by the vertical dashed line. The shaded area bounded by the dashed lines indicates the range of linear fits that fit the four data points in the range $0.5 \leq D_{oil}/R_D \leq 1.5$. The solid line corresponds to Eq. (6.5). Error bars are obtained by repeating the experiment and taking the standard deviation. (*b*) The film thickness (determined using Eq. (6.3)) divided by the oil layer thickness.

of the jet and the moment that the joining point has reached $h = 2R_D$. We indeed find that the T_{jet} and T_g are of the same order of magnitude, so we can expect gravity to be influencing the evolution of the jet.

At the moment pinch-off (Fig 6.2(*d*ii)), the layer of oil on the surface of the cavity collides at the axis of symmetry. After the pinch-off, a small part of this oil goes into the jet, but the largest part is left behind to form a cylinder of oil as can be seen in Fig. 6.2(*e*ii). When the radius of the cavity is large, the layer of oil on the surface of the cavity is thin. During the collapse, the radius of the cavity decreases, and as a result the thickness of the oil layer increases. At pinch-off, the oil layer has reached its maximum thickness, and can be measured as the radius of the oil at the pinch-off depth R_{oil}.

Figure 6.6(*a*) shows the radius of the oil at the pinch-off as a function of the initial oil layer thickness. As expected, R_{oil} increases with increasing D_{oil}. Clearly, when the pinch-off takes place place within the oil layer, R_{oil} is not defined anymore. This will be the case when the oil layer thickness D_{oil} is the same or larger than the pinch-off depth D_{pinch}, indicated by the vertical dashed line in Fig. 6.6(*a*).

Looking at the other end of the data set in Fig. 6.6(a), it appears that R_{oil} does not approach zero with $D_{oil} \to 0$. Although it seems that there is only one data point (the lowest one in Fig. 6.6(a)) that falls outside the linear trend, we must stress that the experimental result is very reproducible; each data point is based on about six repeated experiments. An explanation might be found by looking at the oil film thickness when the cavity has reached its maximum expansion. Fig. 6.6(b) shows the ratio between the film thickness D_{film} and the oil layer thickness D_{oil} as a function of the oil layer thickness, where we calculated D_{film} using Eq. (6.3). For a large part of the experimental range the ratio D_{film}/D_{oil} increases with D_{oil}, but at very thin oil layers, the ratio is constant within experimental errors. A constant ratio is D_{film}/D_{oil} reasonable, because it simply means that the film thickness is proportional to D_{oil} for small values of D_{oil}. This constant ratio also implies that R_{oil} will approach zero, only in a different way as we will explain now. Using the approximate constant value 0.03 for the ratio D_{film}/D_{oil}, we can write

$$D_{film} \simeq 0.03 D_{oil}, \tag{6.4}$$

and after substituting this into (6.3), we can write an equation for R_{oil} as a function of D_{oil}:

$$R_{oil} \simeq \sqrt{(0.03 D_{oil} + R_{max}^2) - R_{max}^2}, \tag{6.5}$$

where we take $R_{max} \approx 25$ mm, which is valid in the range that we are interested in. Equation 6.5 is shown as a black solid line in Fig. 6.6(a). Testing this relation for smaller values of D_{oil} is however not straightforward, as it is very difficult to create very thin stable oil layers.

6.3.2 Influence of impact speed

In Fig 6.7 we vary the Froude number by changing the impact speed of the disc. Increasing the Froude number results in more elongated cavities because the collapse, which is initiated by gravity, is slower compared to the disc velocity for higher Froude numbers. A longer cavity has more surface area, over which the oil has to spread. Continuing this argument, increasing the Froude number will decrease the thickness of the oil layer on the surface of the cavity, and consequently the radius of the oil at the pinch-off R_{oil} will be smaller. This would explain the decreasing R_{oil} for increasing Froude numbers.

For higher Froude numbers however, R_{oil} remains approximately constant. Although the uncertainty is larger, there is certainly not the same steep decrease as we observe for $Fr \lesssim 3$. A possible explanation is that for these high velocities the oil does not cover the full surface of the cavity, and the depth to which the oil reaches saturates. We were however not able to obtain a clear picture of what happens due to

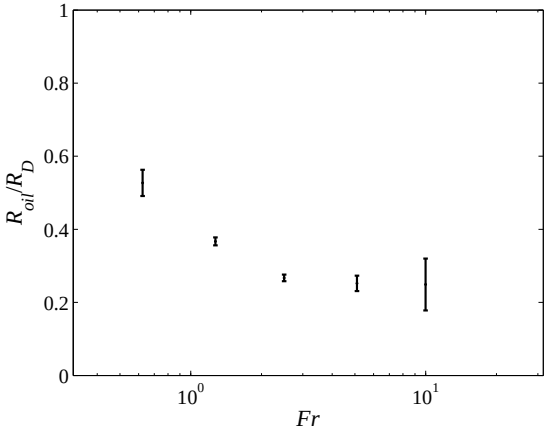

Figure 6.7: Radius of the entrained oil column R_{oil} at the moment of pinch-off as a function of the Froude number. The oil layer thickness D_{oil} was 15 mm and $R_D =$ 20 mm for all experiments. The error bar increases a lot for the highest impact speed, due to the surface seal (see text).

the appearance of a surface seal, where the splash is drawn inwards due to Bernoulli-suction of the air flow, and the cavity is distorted [5]. The surface seal is also the reason for the increased uncertainty at $Fr = 10$.

6.4 Disc started from oil-water interface

We now turn to the experiments described by the setup in Fig. 6.2(b) in which we start the disc at the oil-water interface, accelerate it with a high acceleration to a desired velocity V_D and continue to move down with this velocity. The thickness of the oil layer in these experiments was 45 mm, which is thick enough to be considered as infinite. We verified this by performing the same experiment with an oil layer of 90 mm and 135 mm, which did not influence our results.

Figure 6.8 shows two experiments where we pull down the disc from the oil-water interface. Initially the disc is at rest, we align the bottom of the disc with the oil-water interface. Then, the disc is set into motion and in a short period of time obtains a constant speed V_D[§]. A vortex ring appears just above the disc, along with a smooth profile in the center which connects to the thick oil layer at the top. We are interested in this smooth profile, which has similarities with the shapes seen in [23],

[§]With an acceleration of 42 m/s^2, it takes 0.024 s to reach $V_D = 1$ m/s ($Fr^* = 43$). The duration of the experiment in that case is 0.08 s. The acceleration does not significantly influence the experiment, as can be appreciated in Fig. 6.9

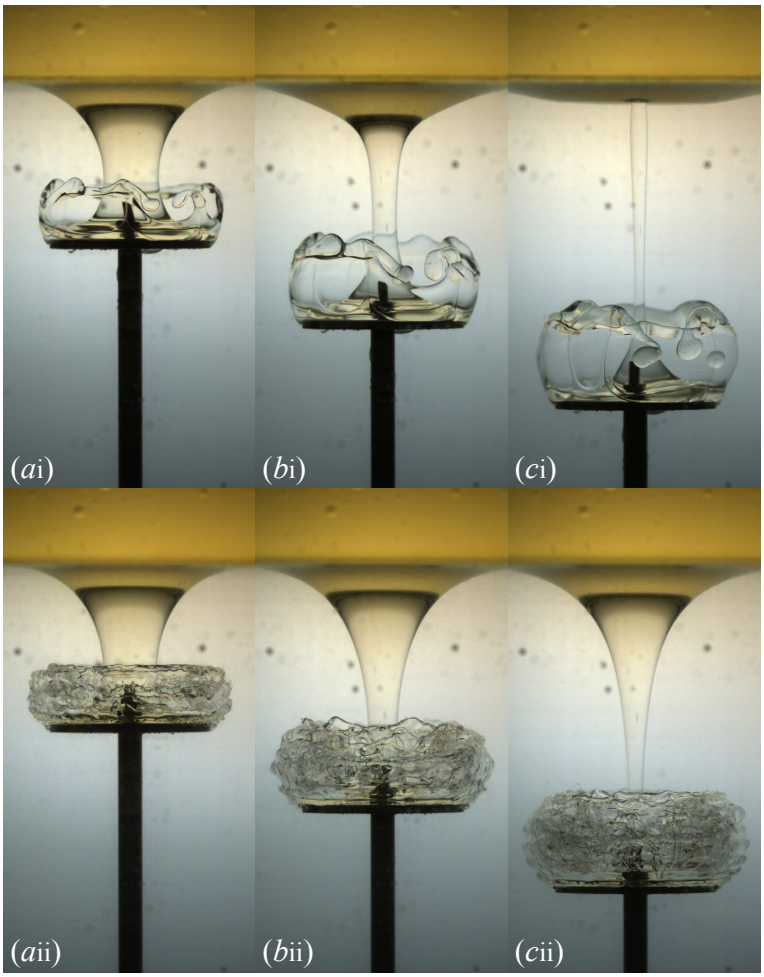

Figure 6.8: Snapshots from two experiments where the disc ($R_D = 20$ mm) starts from the oil-water interface, both with added salt in the water phase, for two different values of the effective Froude number Fr^*: (*a*i-*c*i) $V_D = 0.25$ m/s, $Fr^* = 2.7$; (*a*ii-*c*ii) $V_D = 1.00$ m/s, $Fr^* = 43$. Corresponding pictures have been taken at the same dimensionless time τ. In the top experiment gravity has a clear influence on the shape of the entrained oil column. The bottom experiment is in the inertial regime, where gravity has negligible influence. Near the disc a vortex ring appears, but the funnel-shape of the entrained oil is unaffected.

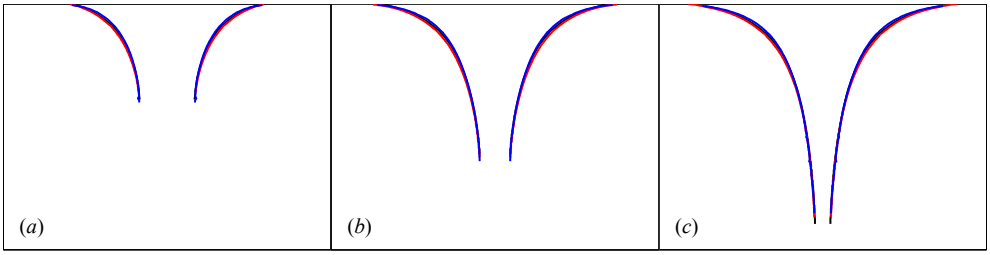

Figure 6.9: Entrained oil for experiments using demineralized water as the heavy fluid (blue lines), and salt water (red lines). An experiment with reduced acceleration (19 m/s^2 in stead of 42 m/s^2) is indicated by the black line. (*a*) $\tau = 2$; (*b*) $\tau = 3$; (*c*) $\tau = 4$.

although that study concentrated on the formation of the vortex ring.

In order to compare the experiments for different disc speeds, we define a dimensionless time $\tau = tV_D/R_D$ (at equal dimensionless times the disc has reached the same vertical position below the undisturbed oil-water interface, measured in units of the disc radius R_D). Comparing Fig. 6.8(*a*i) and (*a*ii), we see that at $\tau = 2$ the shape of the entrained oil is very similar for $Fr^* = 2.7$ and $Fr^* = 43$, although the amount of vorticity in the vortex ring is much larger for the higher speed. At $\tau = 3$ the effect of buoyancy becomes visible, where a difference in the shape of the entrained oil between Fig. 6.8(*b*i) and (*b*ii) is appreciable. In the last frame, Fig. 6.8(*c*i) and (*c*ii) at $\tau = 4$, the oil in the case of $Fr^* = 2.7$ has clearly moved back up due to buoyancy, leaving only a relatively straight cylinder of oil behind. For $Fr^* = 43$, the shape is still unaffected by gravity.

In order to see what the effect of the density difference is on the shape that we obtain at high Froude numbers, we performed experiments with demineralized water ($\rho = 998$ kg/m^3) at $V_D = 1$ m/s ($Fr^* = 99$) and with salt water ($\rho = 1140$ kg/m^3) at $V_D = 1.5$ m/s ($Fr^* = 97$). The obtained profiles are shown in Fig. 6.9. Although there is a factor two in the density difference between the water and the oil phase, the difference in the profiles is negligible, which leads us to the conclusion that the shape of the entrained oil column does not strongly depend on the relative density difference between the fluids. The use of salt water does however have an experimental advantage: The oil-water interface becomes less contaminated with oil and water droplets, which reduces the time that we need to wait between two experiments until the surface is smooth enough to clearly observe formation of the profile of the entrained oil. For experimental convenience, we used salt water in all experiments reported in this section.

In Fig. 6.10 we determined the profiles of the entrained oil for a wide range of Froude numbers. Every colored profile in Fig. 6.10(*c*) consists of several lines, ob-

tained by repeating the experiment. The collapse of lines with the same color indicate the reproducibility of the experiment. We repeated the experiments by decreasing the acceleration of the disc by a factor two to make sure that the observed profiles are not influenced by the initial startup motion of the disc, and we can assume that V_D is obtained instantaneously. We have included the profiles resulting from the experiments with reduced acceleration in Fig. 6.10, showing that we are indeed only probing the influence of Fr^* by comparing the profiles.

Clearly, at $\tau = 2$ (Fig. 6.10(a)), there is no difference in the shape for any value of Fr^* reported here. At $\tau = 3$ (Fig. 6.10(b)), only the lowest values of Fr^* show a different profile. Figure 6.10(c), at $\tau = 4$, shows that we find shapes independent of the effective Froude number for $Fr \to \infty$.

The appearance of differences in the shapes shown in Fig. 6.10 are a result of gravity that is pushing the oil phase upwards. This will only happen if the time is long enough for gravity to become more important than the inertia that is pulling the oil phase down. We can predict the moment that differences appear by comparing the inertial time scale

$$t_{in} \equiv \frac{R_D}{V_D} \tag{6.6}$$

to the gravitational time scale

$$t_g \equiv \sqrt{\frac{R_D}{g^*}}, \tag{6.7}$$

with $g^* = g(\rho_w - \rho_o)/(\rho_w + \rho_o)$. Gravity is expected to become play a role when $t \gtrsim t_g$, which, after dividing both sides by the inertial time scale can be written as

$$\tau^2 \gtrsim Fr^*, \tag{6.8}$$

where we have used $t/t_{in} \equiv \tau$. If we now again look at Fig. 6.10, we expect according to Eq. (6.8) to see a difference for $Fr^* \lesssim 4$ at $\tau = 2$, for $Fr^* \lesssim 9$ at $\tau = 3$, and for $Fr^* \lesssim 16$ at $\tau = 4$. These predictions agree nicely with the moment that we observe differences in the experimental profiles in Fig. 6.10.

6.5 Conclusions

By impacting a disc on a layer of oil floating on a water surface, we have provided experimental insight into the process of jet formation and the behavior of the liquid in the bulk after the pinch-off of a surface cavity. We have shown that the jet that forms after the pinch-off initially is formed from liquid that is very close to the surface of the cavity, and that the stagnation point flow after the pinch-off is very weak; both observations are in agreement with an earlier theoretical and numerical study [1]. Longer times after the jet formation, when the water joins the jet, we observe a stable

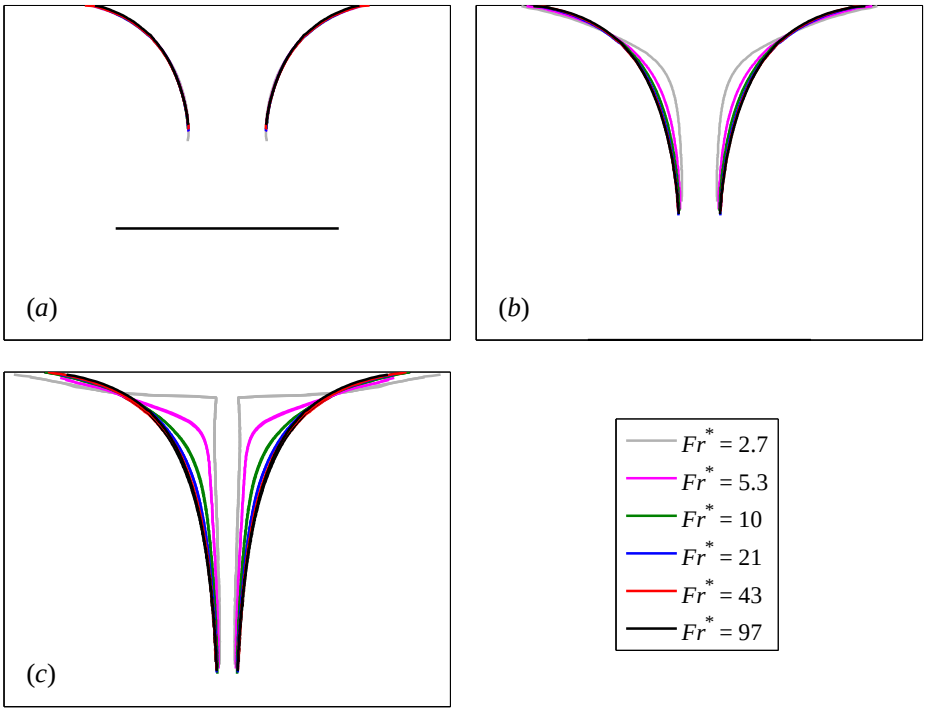

Figure 6.10: Profiles of the entrained oil, for effective Froude numbers ranging from 2.7 to 97. We observe universal profiles for $Fr^* \to \infty$, each color in the image corresponds to one Froude number. (a) at $\tau = 2$, all shapes collapse. (b) at $\tau = 3$, a difference becomes visible for $Fr^* = 2.7$ and $Fr^* = 5.3$ (c) $\tau = 4$, for increasing Fr^*, the shapes of the entrained oil converge to a single universal profile independent of Fr^*. The position and size of the disc is indicated by the horizontal solid black line. In (b) the disc coincides with the bottom of the image; in (c) the disc is below the image. The profile of the oil-water interface is not shown in the vicinity of the disc because the profile was not visible due to the vortex ring, see Fig. 6.8.

core of oil in the center of the jet that extends all the way down into the bulk. We have determined how the oil content depends on the oil layer thickness and impact speed.

In a second set of experiments we started the disc at the oil-water interface and pulled it down at a constant speed from there. The oil layer was thick enough to be considered infinite. We observe that, next to the formation of a vortex ring, a smooth profile is formed by the oil that is being entrained. For large values of the corrected Froude number the shape is unaffected by gravity, resulting in a universal shape that is independent of the Froude number as well as the relative density difference, at least for the density differences studied.

References

[1] S. Gekle, J. M. Gordillo, D. van der Meer, and D. Lohse, *High-Speed Jet Formation after Solid Object Impact*, Phys. Rev. Lett. **102**, 034502 (2009).

[2] A. M. Worthington and R. S. Cole, *Impact with a Liquid Surface, Studies by the Aid of Instantaneous Photography*, Philos. T. R. Soc. A **189**, 137–148 (1896).

[3] A. M. Worthington and R. S. Cole, *Impact with a Liquid Surface Studied by the Aid of Instantaneous Photography. Paper II*, Philos. T. R. Soc. A **194**, 175–199 (1900).

[4] E. G. Richardson, *The Impact of a Solid on a Liquid Surface*, Proc. Phys. Soc. **61**, 352–367 (1948).

[5] R. Bergmann, D. van der Meer, S. Gekle, A. van der Bos, and D. Lohse, *Controlled impact of a disk on a water surface: cavity dynamics*, J. Fluid Mech. **633**, 381–409 (2009).

[6] R. R. L. Foy, T. T. Truscott, and A. H. Techet, *Quantitative Flow Field Imaging about a Hydrophobic Sphere Impacting on a Free Surface* 1–2 (2008), arXiv:0810.1946v2.

[7] J. Eggers and E. Villermaux, *Physics of liquid jets*, Rep. Prog. Phys. **71**, 036601 (2008).

[8] M. S. Longuet-Higgins, *Bubbles, breaking waves and hyperbolic jets at a free surface*, J. Fluid Mech. **127**, 103–121 (1983).

[9] S. Gekle and J. M. Gordillo, *Generation and breakup of Worthington jets after cavity collapse. Part 1. Jet formation*, J. Fluid Mech. **663**, 293–330 (2010).

[10] A. M. Gañán Calvo, *Jetting-dripping transition of a liquid jet in a lower viscosity co-flowing immiscible liquid: the minimum flow rate in flow focusing*, J. Fluid Mech. **553**, 75 (2006).

[11] S. L. Anna, N. Bontoux, and H. a. Stone, *Formation of dispersions using flow focusing in microchannels*, Applied Physics Letters **82**, 364 (2003).

[12] A. Amini, E. Bollaert, J. Boillat, and A. Schleiss, *Dynamics of low-viscosity oils retained by rigid and flexible barriers*, Ocean Eng. **35**, 1479–1491 (2008).

[13] H. Kato, Y. Oe, M. Honoki, T. Mochiki, and T. Fukazawa, *Dispersion of spilled oil by a cavitating jet at sea*, J. Mar. Sci. Tech. **11**, 131–138 (2006).

[14] M. Sato and I. Sumita, *Experiments on gravitational phase separation of binary immiscible fluids*, J. Fluid Mech. **591**, 289–319 (2007).

[15] V. Safronov, *The heating of the earth during its formation*, Icarus **33**, 3–12 (1978).

[16] P. K. Kundu and I. M. Cohen, *Fluid Mechanics*, third edition (Elsevier) (2004).

[17] R. Bergmann, D. van der Meer, M. Stijnman, M. Sandtke, A. Prosperetti, and D. Lohse, *Giant Bubble Pinch-Off*, Phys. Rev. Lett. **96**, 154505 (2006).

[18] I. R. Peters, D. van der Meer, and J. M. Gordillo, *Splash formation and droplet ejection after disc impact on a liquid*, In progress (2012).

[19] P.-G. de Gennes, F. Brochard-Wyart, and D. Quéré, *Capillarity and wetting phenomena* (Springer) (2003).

[20] F. B. Wyart, P. Martin, and C. Redon, *Liquid/liquid dewetting*, Langmuir **9**, 3682–3690 (1993).

[21] P. Lambooy, K. Phelan, O. Haugg, and G. Krausch, *Dewetting at the liquid-liquid interface.*, Phys. Rev. Lett. **76**, 1110–1113 (1996).

[22] L. Rayleigh, *On The Instability Of Jets*, Proc. London Math. Soc. **s1-10**, 4–13 (1878).

[23] Q.-X. Lian and Z. Huang, *Starting flow and structures of the starting vortex behind bluff bodies with sharp edges*, Exp. Fluids **8**, 95–103 (1989).

7

Highly focused supersonic microjets: numerical simulations*

By focusing a laser pulse inside a capillary partially filled with liquid, a vapor bubble is created which emits a pressure wave. This pressure wave travels through the liquid and creates a fast, focused axisymmetric microjet when it is reflected at the meniscus. We numerically investigate the formation of this microjet using axisymmetric boundary-integral simulations, where we model the pressure wave as a pressure pulse applied on the bubble. We find a good agreement between the simulations and experimental results in terms of the time evolution of the jet and on all parameters that can be compared directly. We present a simple analytical model that accurately predicts the velocity of the jet after the pressure pulse and its maximum velocity.

7.1 Introduction

In recent experiments by Tagawa *et al.* [1], it was found that microscopic jets that travel at a speeds up to 850 m/s can be created by focusing a laser pulse inside a liquid-filled capillary that is open at one end. Besides the high velocity, the jets were found to be highly reproducible and controllable. The laser pulse used in the experiments, which has an energy of the order of 100 μJ, results in the formation of a vapor bubble accompanied by a pressure wave [2, 3]. This pressure wave is reflected

*Submitted as: I.R. Peters, Y. Tagawa, N. Oudalov, C. Sun, A. Prosperetti, D. Lohse and D. van der Meer, *Highly focused supersonic microjets: numerical simulations*, J. Fluid Mech. (2012)

at the free surface, where the jet is formed. The shape of the free surface was found to play a crucial role in the formation of the jet, as it is responsible for focusing the liquid into a jet.

In this chapter, we present numerical simulations which accurately reproduce the evolution of the shape and the velocity of the jets observed in the experiments described in [1]. We use axisymmetric boundary integral (BI) simulations where we model the effect of the traveling pressure wave by applying a short pressure pulse on a bubble with a constant amplitude Δp and a (short) duration Δt such that the resulting impulse per unit area $\Delta p \Delta t$ is of the order of 10 Pa$\cdot$s. Figure 7.1 shows the formation of a jet in the experiment together with a result from our boundary integral simulations. We provide a theoretical analysis that gives the correct scaling for the jet speed as a function of the contact angle, bubble distance and pressure pulse.

Jets that are formed from a meniscus have been studied in several cases with different sources for the driving pressure: In [4], the pressure was provided by surface tension, and Antkowiak *et al.* [5] created a pressure pulse by impacting a test tube on a hard surface. In [6] and [7] the driving was provided by hydrostatic pressure. In all these cases the scale of the jets is much larger and the velocities are at least an order of magnitude smaller than those that we study here.

The formation of the jet is different from the jet that follows from the collapse of a liquid void [8–11], where the jet initiates from a geometric singularity. In that case the size and the initial speed of the jet following the collapse of a cavity is therefore not set by the typical size and velocity of the experiment. Neither does the theory of a hyperbolic jet [12] apply here. The main ingredient of the latter is a hyperbolic radial inflow from infinity, which in our setup is impossible due to the confinement of the tube. In fact, the jet that we study scales with the size of the capillary, and the speed is controlled by a combination of driving and geometry.

The chapter is organized as follows. First we introduce the numerical method in § 7.2, after that we discuss the results from the numerical simulations and compare these results to the experiments in § 7.3. We then derive an analytical model in § 7.4, and we end with the conclusions and discussion § 7.5.

7.2 Numerical setup

We perform numerical simulations using a boundary integral code, as described in [13], [14], [15] and [16]. Here, we repeat the basic principles and methods, and elaborate on the parts that are specific for our case.

We approximate the flow in our system to be incompressible, inviscid and irrotational, so that we can describe the velocity field $\mathbf{v}$ as the gradient of a potential ϕ

$$\mathbf{v} = \nabla \phi \tag{7.1}$$

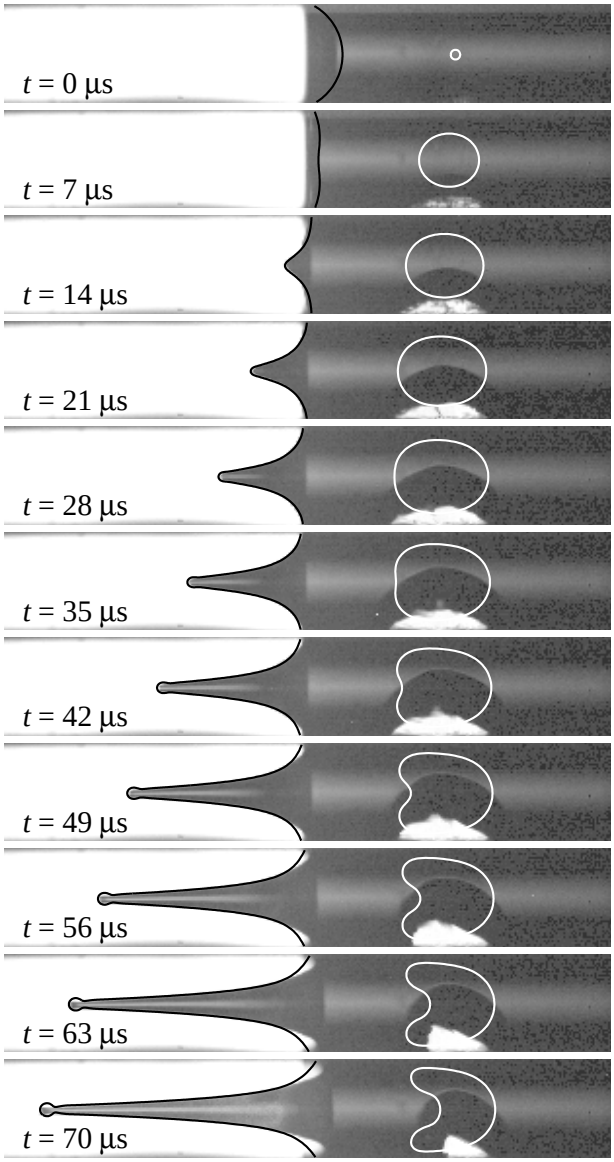

Figure 7.1: Jet formation in experiment (background images) and simulation (black and white solid lines). Absorbed laser energy was 365 μJ, distance between laser focus and meniscus was 600 μm, the tube radius is 250 μm. Pressure amplitude used in the simulation was 1581 bar, pressure duration was 50 ns, and the initial bubble radius was 25 μm.

which satisfies the Laplace equation

$$\nabla^2 \phi = 0. \tag{7.2}$$

Using Green's identity, the potential at any point inside the liquid domain can be described by an integral over the boundary containing ϕ and ϕ_n, where ϕ_n is the spatial derivative of ϕ in the direction normal to the boundary. The system can be solved if at every point on the boundary either ϕ or ϕ_n is known. Solving the system is greatly simplified by imposing axial symmetry, reducing the surface integrals to line integrals. This simplification is justified by the axial symmetry observed in the experiments. On stationary solid boundaries we have $\phi_n = 0$, and on the free surface we know the potential after time-integrating the unsteady Bernoulli equation

$$\frac{\partial \phi}{\partial t} = -\frac{1}{2}|\nabla \phi|^2 - \frac{\Delta p + \kappa \sigma}{\rho} - gz \tag{7.3}$$

with $\Delta p = p_g - p_a$ the pressure of the ambient vapor minus the atmospheric pressure, κ the curvature, σ the surface tension, ρ the liquid density, g the gravitational acceleration and z the vertical coordinate. Due to the size and the time scale of the experiment, the gravitational component gz can be neglected. After solving the boundary integral equation, ϕ and ϕ_n are known everywhere on the boundary, and the new position of the free surface can be achieved by time-integrating the kinematic boundary condition

$$\frac{\mathrm{d}\mathbf{r}}{\mathrm{d}t} = \nabla \phi. \tag{7.4}$$

Due to the absence of viscosity, some form of surface smoothing is necessary to keep the simulation stable. We use the node-shifting technique described by [17], according to which new nodes are placed half way between all existing nodes, after which the original nodes are removed. This method effectively removes instabilities that are related to the node spacing everywhere on the free surface, except at the node on the symmetry axis because this node cannot be shifted or removed. We found that in our situation this node was subject to these instabilities, and therefore we applied an additional smoothing to it. This was done with the help of quadratic extrapolation of the position and the potential, using the two nodes next to the axis of symmetry and the symmetry condition. We verified that the numerical solutions were not sensitive to the amount of smoothing that we applied.

Because we are investigating a liquid inside a capillary, we have to take into account a moving contact line. The node that connects the liquid surface to the solid boundary can be considered both as part of the free surface and of the capillary wall. In solving the boundary integral equation, we treat this connecting node as a the latter, and impose $\phi_n = 0$ on it. Implementation of the actual moving contact line with a dynamic contact angle as described by [18] would not be appropriate here

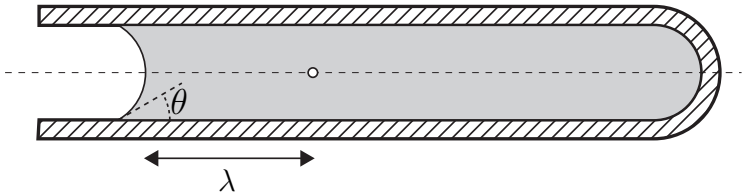

Figure 7.2: The axisymmetric numerical setup. A tube of radius R_t is filled with liquid. The liquid-air interface has the shape of a spherical cap, with a contact angle θ. We position a bubble with a radius of $1/10$ of the tube radius at a distance λ from the meniscus. The dashed line in the center represents the axis of symmetry.

since this is based on a balance between surface tension and viscosity, while our simulations are inviscid. Instead, we calculate the new position of the connecting node by extrapolating the nodes next to the connecting node. This method is similar to the one used by [13], where the node connecting to the solid was displaced so that the contact angle remained at 90°. The exact implementation turns out only to have a non-negligible effect only close to the contact point and not to be important for the development of the jet. Comparing the extrapolation method and fixed contact angles between 60° and 120° resulted in less than 1% variation of the maximum jet velocity.

7.2.1 Initial condition

The computational domain that we use is closed at one side in the shape of a half-sphere; the free surface is at the opposite side of the tube (see Fig. 7.2). Because the diameter of the tube is much smaller than the capillary length, gravity can be safely neglected, and the free surface adopts the shape of a spherical cap. The initial shape of the free surface in the simulations can therefore be defined using only the static contact angle θ. Note that the contact angle θ only serves as an initial condition, and we do not impose a dynamic contact angle. A bubble with a radius $1/10$ of the tube radius is positioned at a distance λ from the free surface. The distance of the bubble from the closed end of the tube does not have an influence on the simulations, as long as it is a few tube radii or more.

7.2.2 Pressure wave model

In the experiment, a pressure wave is created by vaporizing a small amount of liquid with a laser pulse. This abrupt vaporization is responsible for a very large increase in the pressure in a small volume, which results in a pressure wave that travels through the tube and reflects on the free surface [1]. As argued in that paper, the initial velocity V_0 of the free surface is connected to the pressure wave strength $\Delta p \approx \frac{1}{2}\rho c V_0$,

where c is the speed of sound in the liquid. E.g., for $V_0 \sim 10$ m/s and $c = 1497$ m/s we find $\Delta p \sim 75$ bar.

The reflections of the pressure wave on the free surface and the wall of the tube ultimately result in a pressure gradient between the vapor bubble and the free surface, so that the entire liquid volume in between will start to move. Starting from this very early point in time, the dynamics of the system is expected to be well described by the potential flow boundary integral model employed in this chapter. In the simulation, we model this pressure wave by applying a pressure pulse on the bubble [19]. This pressure pulse has a typical amplitude Δp and a duration Δt. Figure 7.3 shows that if Δt is small enough, the only relevant value is the product $\Delta p \Delta t$ (which is of the order of 10 Pa·s) and the pressure pulse can be assumed to be instantaneous. For simplicity, we will keep Δt at 50 ns, and vary only the pressure amplitude. With this choice, the pressure amplitude easily reaches values of the order of 10^3 bar, i.e., in excess of the critical pressure of water (≈ 220 bar). This does not need to worry us too much, since not Δp itself but the product $\Delta p \Delta t$ determines the course of events. After the pressure pulse, the pressure inside the bubble is set to zero to account for the rapid condensation of the vapor in the bubble as was also done by [19]. A more sophisticated model where the heat exchange is taken into account for the growth and collapse of a vapor bubble created by a laser pulse can be found in [20]. In our case, applying a perfect gas law as well as incorporating heat transfer only resulted in marginal differences in the jet. We therefore use a simpler model here, which minimizes the number of unknown adjustable parameters. The good agreement between the simulations and the experiments convinces us that our model is accurate enough to describe the physics that create the jets observed in experiments.

7.3 Numerical results

We will show here the results from the numerical simulations, and compare them with the experiments of Tagawa *et al.* [1]. In Fig. 7.1 we find eleven snapshots from the experiment, overlaid with the corresponding BI results. At $t = 0$ the laser pulse is absorbed which modeled in the simulation as a bubble pressurized to 1581 bar for a time span of 50 ns. The initially concave interface starts to move instantly and goes through an almost flat stage at $t = 7$ μs to the development of a jet ($t = 14 - 56$ μs). The maximum jet speed is reached between the second and the third frame at $t =$ 10 μs, when the jet just starts to form. The position of the tip of the jet is fully reproduced, as well as the overall shape of the jet. The bubble in the experiment is created near the wall of the capillary, resulting in a difference in shape, but its size is reproduced by the simulations at least up to $t = 35$ μs, as can be appreciated by considering volume conservation in the system. Because the full free surface of the

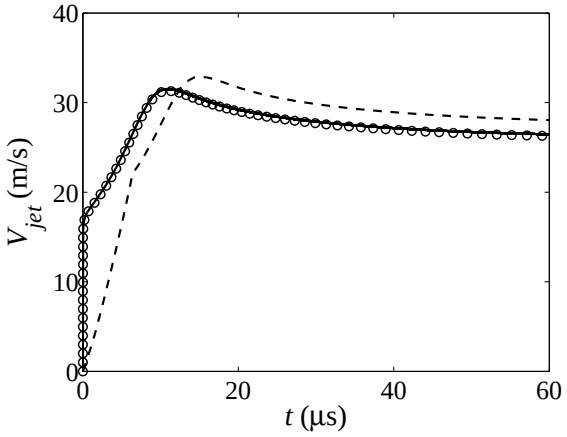

Figure 7.3: The velocity of the tip of the jet as a function of time for different values of Δt. The product $\Delta t \Delta p$ is kept constant at 15.20 Pa·s, showing that the velocity of the jet only depends on this product when Δt is small enough. The results for $\Delta t = 25$ ns (circles, $\Delta p = 6080$ bar) and $\Delta t = 50$ ns (solid line, $\Delta p = 3040$ bar) overlap, whereas a significantly larger duration of the pressure pulse $\Delta t = 6.4$ μs (dashed line, $\Delta p = 23.75$ bar) results in a different velocity and a different evolution of the velocity.

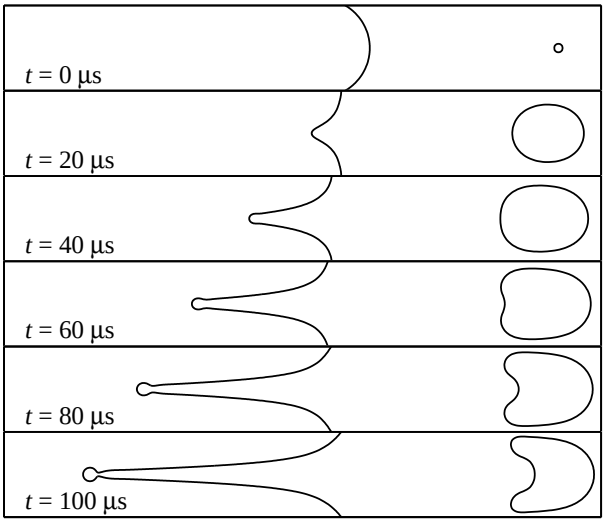

Figure 7.4: The evolution of the jet and the bubble from a boundary integral simulation. Parameters: $R_{tube} = 250$ μm, $\Delta p = 2027$ bar, $\Delta t = 50$ ns, $\theta = 30$ degrees, $\lambda = 1106$ μm.

experimental jet is reproduced by the simulation up to $t = 35$ μs, we know that the volume of the bubble in the simulation is also the same as in the experiment. After this there is a slight difference in the collapse of the bubble, which results in a small difference at the base of the jet where the free surface connects to the wall of the capillary. This however has no significant effect on the part of the jet that is further away from the contact point.

7.3.1 Jet and bubble shape

Figure 7.4 shows how the jet and the bubble develop in time. The maximum speed of the jet is approximately 30 m/s, which is reached around 20 μs after the pressure pulse. The jet has a diameter which is about $1/10$ of the diameter of the tube; this holds for all tube diameters that we tested. The bubble initially grows spherically but, due to confinement and asymmetry, it later takes on an elongated shape and grows more towards the free surface. The right side of the bubble is almost stationary, also during the collapse where a thick jet is formed reminiscent of the collapse of a bubble near a free surface or a solid boundary [21, 22].

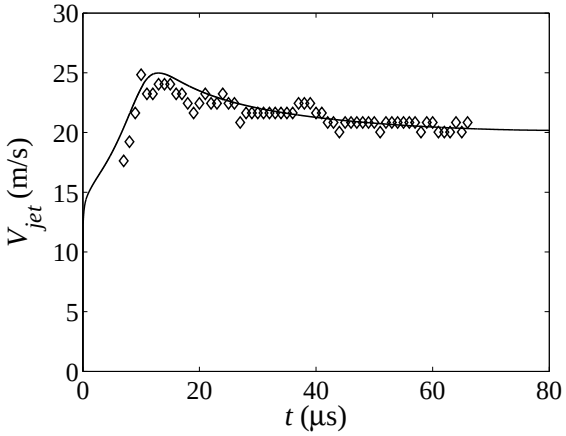

Figure 7.5: The velocity of the tip of the jet as a function of time for both the simulation (solid line) and experiments (diamonds). After an almost instantaneous acceleration to 13 m/s during the 50 ns pressure pulse, the tip is further accelerated by the focusing geometry to about 25 m/s. Experimental conditions and numerical settings are the same as in Fig. 7.1.

7.3.2 Jet velocity and velocity field

In this chapter we focus on the jet velocity which can directly be compared with the experimental measurements. We define the jet velocity as the velocity component parallel to the tube axis at the tip of the jet (in Fig. 7.4 to the left). Figure 7.5 shows numerical results together with experimental results on how the jet velocity evolves in time. There are two acceleration mechanisms: First, driven by the very short pressure pulse, a speed of about 13 m/s is reached almost instantaneously. After this there is no more driving, but the focusing of the flow accounts for a further acceleration of the jet which reaches a maximum velocity of about 25 m/s. Deceleration is accounted for by surface tension (see § 7.3.4) and the collapsing bubble.

Figure 7.6 shows the velocity field in the liquid during jet formation. In Fig. 7.6(a) the interface has not moved significantly due to the small time interval, but it clearly shows how the interface is responsible for the focusing of the flow. In Fig. 7.6(b) we see that although the surface in the center is approximately flat, the velocity still has a focusing profile. Indeed, at $t = 7.5$ μs the jet is still accelerating. Only after about 15 μs (see Fig. 7.6(c)), there is no more focusing of the flow. Stretching of the jet is visible in Fig. 7.6(d) and 7.6(e) where the velocity of the tip of the jet is larger than the velocity at the base, with the consequence that the jet becomes thinner while increasing in length [23].

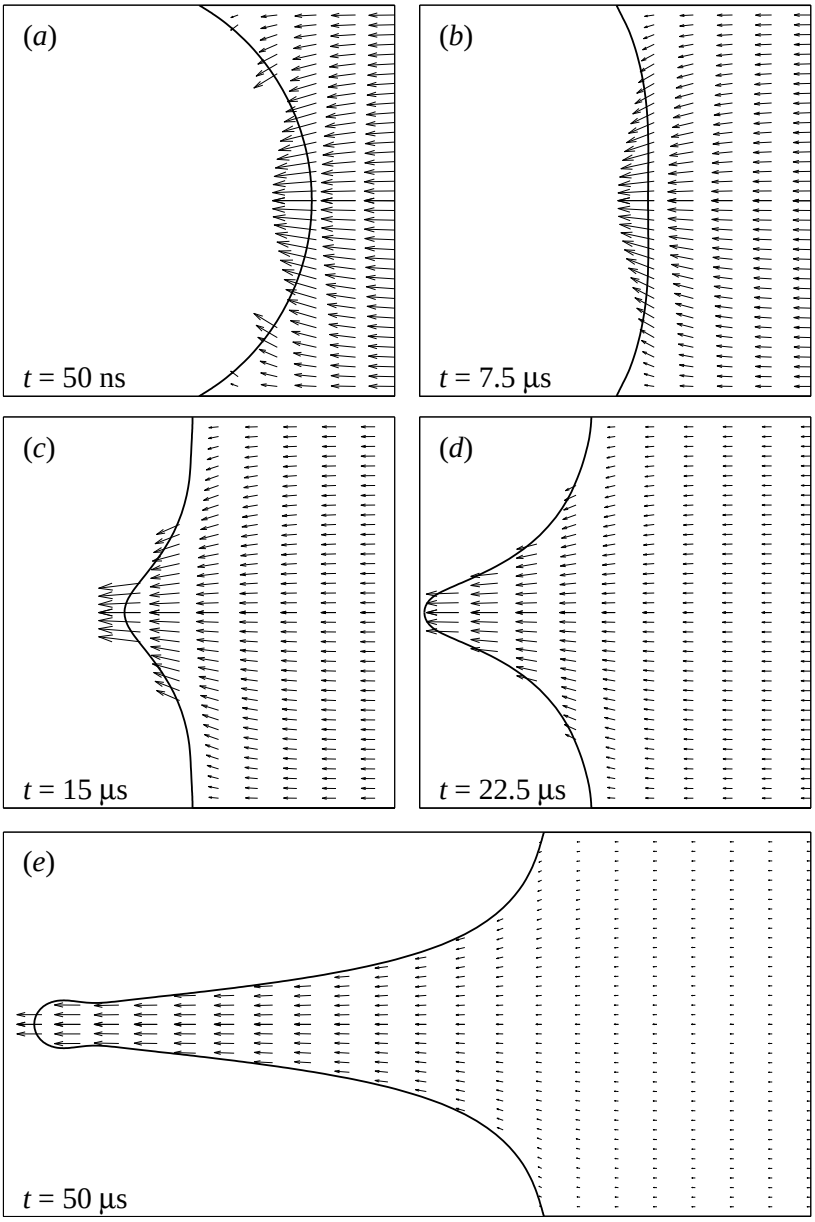

Figure 7.6: The velocity field during the formation of the jet. (*a*) is right after the pressure pulse, the free surface still has a spherical cap shape. In (*a*), (*b*) and (*c*), focusing of the flow can be seen. (*d*) and (*e*) clearly show the stretching of the jet: The largest velocity is in the tip of the jet, and gradually decreases towards the base of the jet.

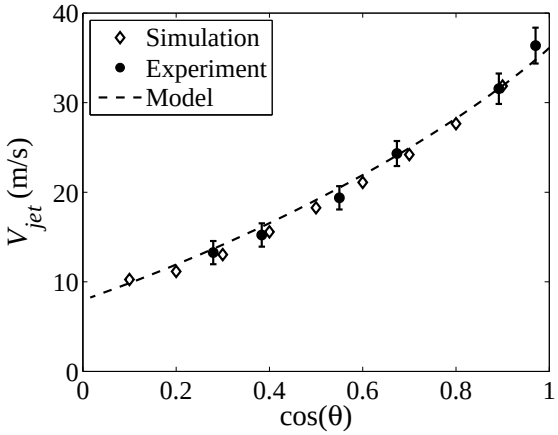

Figure 7.7: The influence of the contact angle on the jet velocity. Tube radius is 250 μm, and $\lambda = 460$ μm. The numerical results are obtained with $\Delta p = 1647$ bar, the absorbed laser energy in the experimental data was 458 μJ. The dashed line represents the model (7.21), with $\alpha = 0.44$, $\beta = 1.33$, and $h_0 = 0.26$.

7.3.3 Contact angle

Now, how does the jet speed depend on the contact angle? As we explained in § 7.2.1 the meniscus initially has the shape of a spherical cap. The meniscus thus has a well-defined radius of curvature, which depends on the contact angle θ. A contact angle of 90° results in a flat interface (no curvature), and a contact angle of 0° gives a radius of curvature equal to the inner radius of the capillary. A smaller contact angle increases the curvature of the free surface, and therefore increases the focusing of the flow.

In the experiments, θ can be measured directly from images of the static meniscus, so we can directly compare the influence of the contact angle in experiments and simulations. Figure 7.7 shows that the jet velocity is approximately linearly dependent on $\cos\theta$. The deviation from the linear fit suggests that the dependence on the contact angle is a bit stronger than linear, both in the experimental and the computation. A correction to the linear dependence and a more precise explanation for the dependence on θ can be found in § 7.4. The absorbed laser energy in the experiments in Fig. 7.7 was 458 μJ, the applied pressure in the simulations was 1674 bar.

7.3.4 Surface tension

In order to study the effect of surface tension in isolation, we turn off the collapse mechanism of the bubble by setting the pressure in it to atmospheric after the initial pressure pulse. In this case the bubble keeps growing until it would be ultimately

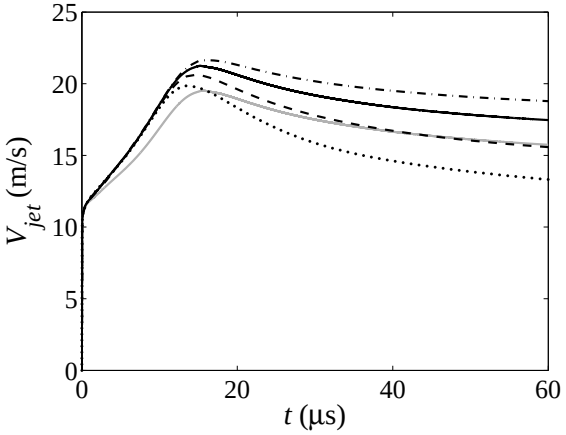

Figure 7.8: Jet speed versus time for different surface tensions. The black solid line has the surface tension of water ($\sigma = 72.8$ mN/m), the other values for the surface tension are $\sigma = 35$ mN/m (dash-dotted line), $\sigma = 150$ mN/m (dashed line) and $\sigma = 300$ mN/m (dotted line). The collapse of the bubble was turned off in these simulations to isolate the effect of surface tension. Tube radius is 250 μm, $\lambda = 1106$ μm, and $\Delta p = 2027$ bar. For reference, the evolution of the jet velocity with bubble collapse is represented by the gray solid line, with the same parameters and $\sigma = 72.8$ mN/m.

restrained by surface tension over a much longer time scale than we consider.

Figure 7.8 shows the development of the jet velocity for four different values of the surface tension. Clearly, the acceleration phase is dominated by inertia, as there is almost no difference in the acceleration while there is an order of magnitude difference in the surface tension. Only when the jet reaches its maximum velocity and during deceleration surface tension starts to play a role. This stands to reason, because the only decelerating mechanism in this case is surface tension, counteracting the increase of surface area caused by the jet.

7.3.5 Pressure impulse

The magnitude of the pressure impulse $\Delta p \Delta t$ is the only parameter that cannot be directly related to the experiment. We expect that the absorbed laser energy is the experimental parameter that is most directly related to it. In the experiments, a linear relation between the energy and the velocity of the jet is found. As can be seen in Fig. 7.9, in the numerical simulation the jet velocity also depends linearly on the pressure pulse. From these observations we conclude that there is a linear relation between the absorbed laser energy (E in Joules) as measured in the experiments and

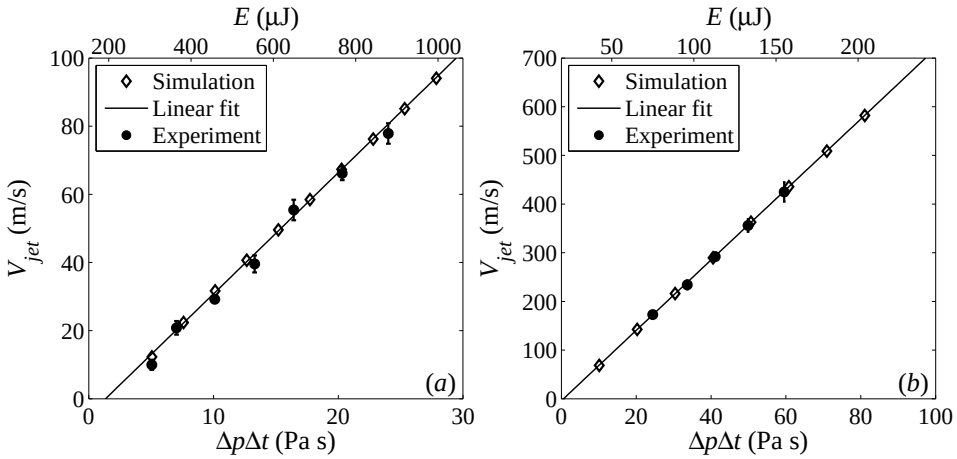

Figure 7.9: The influence of the pressure on the jet velocity, compared to experiments for two different tube radii. (*a*): Tube radius 250 μm, $\Delta t = 50$ ns, $\theta = 30$ degrees and $\lambda = 600$ μm. (*b*): Tube radius 25 μm, $\Delta t = 5$ ns, $\theta = 30$ degrees and $\lambda = 400$ μm. Experimental data were converted from the absorbed laser energy to pressure impulse by a fitting routine; the energy is indicated at the top axis.

the pressure impulse that we apply in the simulations of Fig. 7.9:

$$\Delta p \Delta t \approx 3.30 \cdot 10^4 \ \mathrm{s\,m^{-3}}\, E - 5.0 \ \mathrm{Pa \cdot s} \tag{7.5}$$

for $R_{tube} = 250$ μm, and

$$\Delta p \Delta t \approx 4.39 \cdot 10^5 \ \mathrm{s\,m^{-3}}\, E - 8.5 \ \mathrm{Pa \cdot s} \tag{7.6}$$

for $R_{tube} = 25$ μm. The prefactor is one order of magnitude larger when the tube radius is one order smaller, while the threshold value is of the same order. More about the influence of the tube radius can be found in § 7.3.6.

In both the simulation and the experiment, there is an apparent threshold value for the energy or pressure below which we cannot observe a well-defined jet. In the experiments, the main reason for this would be that a large amount of the laser energy is lost in heating up the fluid before a bubble can be created, as was shown by [20]. In the simulations the only cause for the threshold lies in the surface tension that prevents the formation of a jet, and the vacuum inside the bubble after the pressure pulse is applied. Once the kinetic energy is much larger than the surface energy related to the formation of the jet and the potential energy related to the size of the vacuum bubble, a jet can be formed. The zero value of E extrapolated on the upper horizontal scale in Fig. 7.9 lies considerably to the left of the zero value of the lower

impulse scale, which implies that the experimental threshold, due to thermal and other losses, is significantly higher than the numerical one.

7.3.6 Tube radius

In the experiments, there is a clear dependence of the jet velocity on the tube radius: smaller tubes create faster jets with the same absorbed laser energy, approximately following the relation $V_{jet} \propto 1/R_t$. One naively would argue that a smaller tube will provide a stronger curved free surface, and therefore the stronger focusing will result in a faster jet. Figure 7.10 shows that the maximum jet speed that is obtained in the simulations only shows a very weak dependence on the tube radius. However, a different effect caused by the tube radius is very clear: The acceleration is much larger for smaller tubes, so that the maximum velocity is reached earlier. Indeed, a smaller tube provides a higher curvature of the free surface, so the acceleration due to flow focusing is larger. The maximum velocity, however, is a combination of the magnitude and the duration of the acceleration, which both depend on the tube radius. The simulations show that these two parameters cancel each other if we only change the tube radius: larger tubes have less acceleration due to focusing of the flow, but the acceleration persists for a longer time, as can be seen clearly in Fig. 7.10.

The remaining question is why there is such a strong dependence on the tube radius in the experiments. The most plausible explanation is that for a fixed absorbed energy, the generated pressure has a strong dependence on the tube radius. The reason for this could be found in the volume V_e that is exposed to the laser energy E. Based on dimensional analysis the produced pressure can be expected to scale as

$$\Delta p \propto \frac{E}{V_e} \tag{7.7}$$

A smaller tube would result in a smaller volume that is exposed to the laser energy. This then would account for the dependence of the jet velocity on the tube radius that was observed in the experiments.

7.3.7 Bubble distance from the free surface

In experiments, the most direct measurable parameter is the distance between the meniscus and the bubble. This makes it an excellent candidate to compare with numerical simulations. We define the distance λ as the distance between the center of the bubble and the point on the meniscus that is on the axis of symmetry (see Fig. 7.2). Due to the axisymmetry of the numerical simulations, the bubble is always in the center of the tube. In experiments however, the bubble is usually created near the wall of the tube, due to the characteristics of the absorption of the laser light in the liquid. The difference between these different bubble positions can be neglected

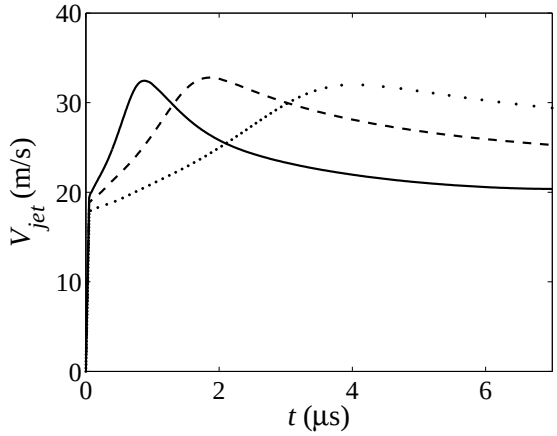

Figure 7.10: The influence of the tube radius on the jet velocity. A smaller radius increases the acceleration due to flow focusing, but decreases the duration of the acceleration, resulting in approximately the same maximum jet velocity. Tube radii in this figure are 25 μm (solid line), 50 μm (dashed line) and 100 μm (dotted line). The other parameters are the same for all three simulations: $\Delta p = 3040$ bar, $\Delta t = 50$ ns, $\theta = 30$ degrees and $\lambda = 1250$ μm.

when the distance between the bubble and the meniscus is large compared to the radius of the tube ($\lambda / R_t \gg 1$).

Figure 7.11 shows the jet velocity as a function of λ, together with the experimental measurements. There is a good agreement between experiments and simulations, and both show a clear $1/\lambda$ dependence for the jet velocity. Both the numerical and the experimental results are obtained with a tube radius of 250 μm and a contact angle of 25 degrees. The absorbed laser energy in the experiments was 305 μJ and the pressure amplitude for the simulations, calculated using (7.5), was 1013 bars.

7.4 Theoretical approximation

We will now try to understand the mechanism of the jet formation and the achieved velocities analytically by approaching the problem with a simplified model. The route through which the jet attains its maximum velocity can be split in two parts: the pressure impulse and the flow focusing. The effect of the former is determined by how the pressure wave in the (incompressible) simulations, which gives an initial velocity to the liquid, is modeled. After the liquid is set into motion, the curved shape of the meniscus leads to a further acceleration of the liquid by focusing it in a fast thin jet. We first neglect the influence of the curvature of the free surface on the action of

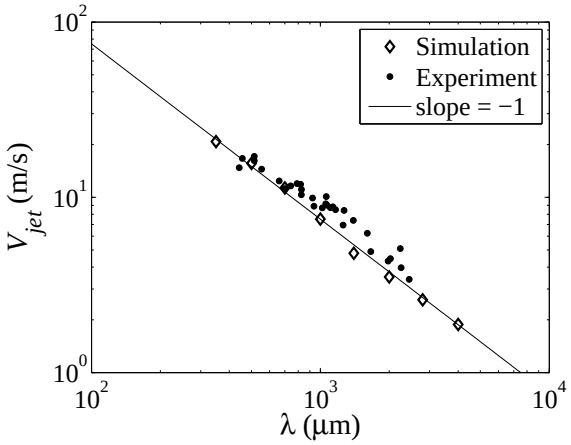

Figure 7.11: The influence of the distance between the bubble and the meniscus on the jet velocity. Tube radius is 250 μm and $\theta = 25°$. The numerical results are obtained with $\Delta p = 1013$ bar, directly related with (7.5) to the absorbed laser energy in the experimental data, which was 305 μJ. A power-law fit (solid line) reveals a clear $1/\lambda$ dependence of the jet velocity.

the pressure pulse; we revisit this aspect later.

7.4.1 The pressure pulse

We approximate the system during the pressure pulse as one-dimensional, so after neglecting viscosity and compressibility we can write the Euler equation as

$$\frac{\partial u}{\partial t} = -\frac{1}{\rho}\frac{\partial p}{\partial z}, \tag{7.8}$$

where u is the axial velocity of the liquid, and t the time. Note that due to continuity in this one-dimensional system, the $\partial u/\partial z$ term in the material derivative equals 0, so on the left hand side we only have $\partial u/\partial t$. The axial pressure gradient $\partial p/\partial z$ is given by the pressure in the bubble Δp and the distance λ between the bubble and the free surface:

$$\frac{\partial p}{\partial z} = \frac{\Delta p}{\lambda}. \tag{7.9}$$

The Laplace pressure jump on the free surface can be neglected because Δp is very large compared to the typical pressure associated with surface tension.

We integrate (7.8) over the duration Δt of the pressure pulse and obtain the velocity V_0 of the free surface after the pressure pulse [19]:

$$V_0 = \frac{\Delta p \Delta t}{\rho \lambda}, \tag{7.10}$$

where we assume λ to be constant, which can be done if Δt is small enough.

7.4.2 The flow focusing

After the pressure pulse there is no more driving of the flow, which means that all further acceleration is caused by focusing. We will now give an analysis for the acceleration due to flow focusing based on continuity. Starting with a spherical surface with radius of curvature R_c and velocity V_0 directed normal it, we keep the flow rate constant:

$$V_0 R_c^2 = (V_0 + dV)(R_c - dR)^2, \tag{7.11}$$

where dV is a small increase in velocity due to a small decrease in radius dR. At leading order, $dR = V_0 dt$, and (7.11) becomes:

$$\frac{dV}{dt} = \frac{2V_0^2}{R_c} \tag{7.12}$$

The radius of curvature can be expressed using the tube radius R_t and the contact angle θ as $R_c = R_t/\cos\theta$, which then gives us the following expression for the acceleration:

$$a = 2V_0^2 \frac{\cos\theta}{R_t}. \tag{7.13}$$

Clearly, smaller tubes have stronger focusing and therefore generate a larger acceleration. This, however, does not mean that the maximum velocity of the jet will be higher as well. To determine the increase in speed due to the flow focusing we have to find a time scale during which the fluid is accelerated. The focusing time scale Δt_f is provided by the typical velocity V_0 (the velocity created by the pressure pulse) and the typical length scale R_t (the radius of the tube):

$$\Delta t_f = \frac{R_t}{V_0}. \tag{7.14}$$

The increase in velocity due to flow focusing is then

$$\Delta V \sim a\Delta t_f = 2V_0 \cos\theta, \tag{7.15}$$

where it becomes clear that the increase in velocity due to flow focusing is independent of the tube radius.

7.4.3 The maximum jet velocity

The maximum velocity reached by the jet is the sum of the velocity reached after the pressure pulse and the increase in velocity due to flow focusing

$$V_{max} = V_0 + \Delta V = \frac{\Delta p \Delta t}{\rho\lambda}(1 + \beta\cos\theta), \tag{7.16}$$

with β a proportionality factor which we expect to be of order unity. First of all, the proportionality to $\frac{\Delta p \Delta t}{\rho \lambda}$ is in excellent agreement with the results from the simulations shown in Figs. 7.9, 7.11 and with the fact that V_{max} does not depend on the tube radius (see Fig. 7.10). To compare the dependence on the curvature of the meniscus, we now turn to Fig. 7.13(a). Here we compare the model with $\beta = 2.0$ to the simulation data. The velocities are roughly reproduced, but it is clear that there is a dependence on the curvature for V_0, which is not accounted for by the model and the increase of V_{max} is therefore not very accurately reproduced. Clearly, neglecting the curvature of the surface during the pressure pulse has been too bold an assumption.

7.4.4 Correction for a pressure pulse on a curved interface

We will now apply a correction to the above derived model to account for the curved interface during the pressure pulse. The above derivation (7.10) gives the velocity in the bulk, far away from the the bubble and the free surface. We will use volume conservation and an approximate velocity distribution on the free surface to calculate the free surface velocity on the tube axis.

The first step will be to determine the velocity distribution on the free surface. Due to the short time scale and the magnitude of the pressure pulse, we can neglect the tangential velocity components. We therefore only take into account the velocity normal to the interface, and we can consider the free surface as an equipotential surface. Away from the free surface we expect the one-dimensional approximation to hold, resulting in a uniform axial velocity, so that we will have evenly spaced equipotential surfaces oriented perpendicular to the tube wall.

The free surface is a curved equipotential surface that needs to matched to the plane equipotential surfaces in the bulk. With reference to Fig. 7.12 we introduce a distance H_0, ultimately to be treated as a fitting parameter, as the smallest distance from the free surface where we assume the equipotential surfaces to be unaffected by the curved interface. We now calculate the distance between the free surface and the horizontal plane defined by H_0 in the direction normal to the free surface. We will call this the ζ-dependent effective distance H_e:

$$H_e(\zeta) = \frac{R_c + H_0}{\cos\zeta} - R_c \tag{7.17}$$

where we have defined the position on the free surface as a function of the radius of curvature R_c and the angle ζ, as shown in Fig. 7.12. Because the potential difference between the plane defined by H_0 and the free surface is constant, we expect the velocity to be inversely proportional to the effective distance H_e:

$$V_{fs}(\zeta) = \frac{A}{H_e(\zeta)} \tag{7.18}$$

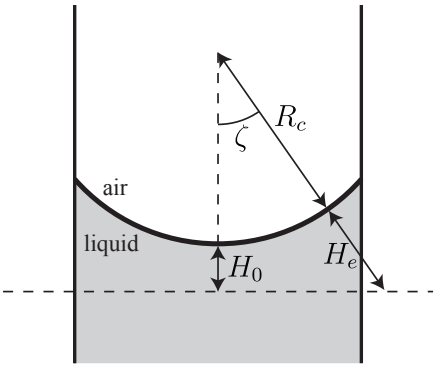

Figure 7.12: Definition of the distance H_0, the effective distance H_e, radius of curvature R_c and angle ζ.

with A a constant that we will determine using volume conservation: The flux through a cross-section in the bulk, where the velocity is uniform, must equal the flux through the free surface:

$$V_B \pi R_t^2 = \int_0^{2\pi} \int_0^{\pi/2-\theta} V_{fs}(\zeta) R_c^2 \sin\zeta \, d\zeta \, d\xi, \tag{7.19}$$

where $V_B = \alpha \frac{\Delta p \Delta t}{\rho \lambda}$, $R_c = R_t/\cos\theta$, and R_t the tube radius. α is a prefactor which should be of order unity, reflecting the one-dimensional character of the flow in the bulk. We expect α to become closer to 1 when λ/R_t increases.

We now have an expression for A, which we substitute in (7.18), and we arrive at the following velocity on the free surface $V_0 \equiv V_{fs}(\zeta = 0, t = \Delta t)$:

$$V_0 = \alpha \frac{\Delta p \Delta t}{\rho \lambda} \frac{1}{2h_0} \frac{\cos\theta}{b \log\left(\frac{\sin\theta - b}{1-b}\right) + \sin\theta - 1} \tag{7.20}$$

with $b = 1 + h_0 \cos\theta$, and the geometrical factor $h_0 = H_0/R_t$. The value of h_0 only needs to be determined once by fitting, since we do not expect it to change with other parameters.

The maximum velocity remains

$$V_{max} = V_0(1 + \beta \cos\theta), \tag{7.21}$$

with V_0 given by (7.20).

In Fig. 7.13(b) we compare the corrected model to the boundary integral simulations, with $\alpha = 0.94$, $\beta = 0.88$, and $h_0 = 0.26$. We find an excellent agreement between the simulations and the model given by (7.20) and (7.21). Figure 7.7 shows

the comparison of the model with both experiments and simulations, for a different tube radius and bubble distance, but we have used the same value for h_0. Note that in the comparison shown in Fig. 7.7, α is smaller, which is due to the fact that in that case $\lambda \sim R_t$.

7.5 Conclusions and discussion

We have numerically investigated the formation of microjets in a capillary by laser induced cavitation using axisymmetric boundary integral simulations. Although compressibility plays an important role in the formation and initial growth of the bubble as well as in the subsequent pressure wave that travels through the liquid, we have assumed incompressibility for our numerical simulations. This is possible because the compressibility is only important during the very short period of the pressure wave reflecting from the free surface, which we have modeled by applying a short strong pressure pulse on the bubble inside the capillary. After the initial pressure impulse, the formation of the jet can be considered as incompressible, because the observed speeds are mostly much smaller than the speed of sound in water, and pressures are moderate.

We have found a convincing agreement in shape and evolution of the jet between the simulations and the experiments, which has allowed us to perform a detailed study of the involved parameters, including those which are difficult to access in experiments.

We compared the influence of the different parameters on the maximum achieved velocity of the jet. We have found good agreement between the simulations and the experiments by investigating the influence of the distance λ and contact angle θ. It is however much harder to directly relate the absorbed laser energy in the experiment to the pressure pulse in the simulation. By comparison we were able to derive that the pressure pulse $\Delta p \Delta t$ is linearly related to the absorbed energy E, and we have given arguments for the dependence of the pressure on the capillary radius R_t.

The jet velocities we find in the simulations can be reproduced accurately by a simple model. We developed this model starting with a one-dimensional approximation for the pressure pulse and dimensional analysis for the focusing effect during jet formation. We improved the one-dimensional approximation by making a correction for the curved interface during the short pressure pulse, where deformation of the meniscus can be neglected.

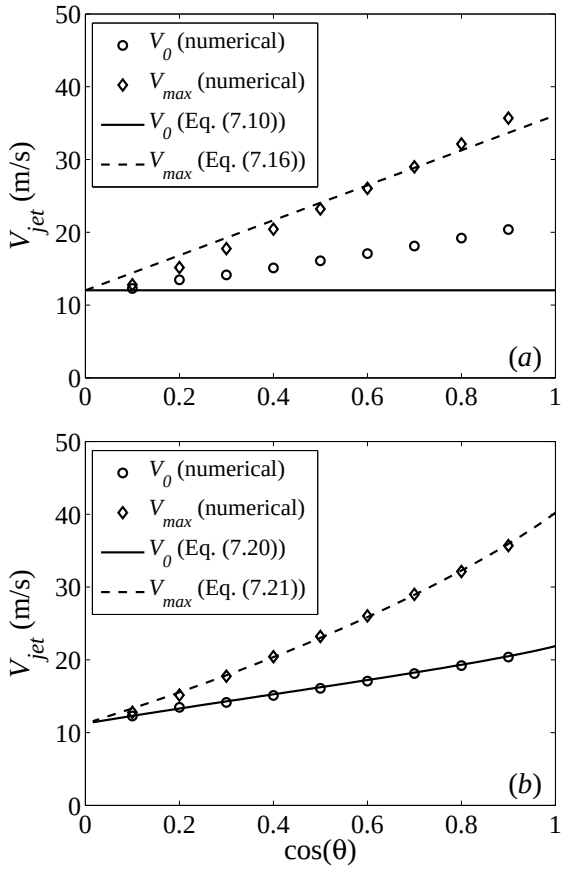

Figure 7.13: The velocity V_0 of the jet just after the pressure pulse and the maximum velocity V_{max} of the jet. Parameters: $R_{tube} = 100\ \mu$m, $\Delta p = 3040$ bar, $\Delta t = 50$ ns, $\lambda = 1250\ \mu$m. The diamonds and circles are results from boundary-integral simulations. In (a) the solid line corresponds to (7.10) and the dashed line corresponds to (7.16), with $\beta = 2$. In (b) the solid line corresponds to (7.20) and the dashed line corresponds to (7.21), with $\alpha = 0.94$, $\beta = 0.84$, and $h_0 = 0.26$.

References

[1] Y. Tagawa, N. Oudalov, C. W. Visser, I. R. Peters, D. van der Meer, C. Sun, A. Prosperetti, and D. Lohse, *Highly focused supersonic microjets* (2012), arXiv:1112.2517v4.

[2] C. E. Bell and J. A. Landt, *Laser-induced high-pressure shock waves in water*, Appl. Phys. Lett. **10**, 46–48 (1967).

[3] M. P. Felix and A. T. Ellis, *Laser-Induced Liquid Breakdown–a Step-By-Step Account*, Appl. Phys. Lett. **19**, 484–486 (1971).

[4] L. Duchemin, S. Popinet, C. Josserand, and S. Zaleski, *Jet formation in bubbles bursting at a free surface*, Phys. Fluids **14**, 3000–3008 (2002).

[5] A. Antkowiak, N. Bremond, S. L. Dizès, and E. Villermaux, *Short-term dynamics of a density interface following an impact*, J. Fluid Mech. **577**, 241–250 (2007).

[6] E. Lorenceau, D. Quéré, J.-Y. Ollitrault, and C. Clanet, *Gravitational oscillations of a liquid column in a pipe*, Phys. Fluids **14**, 1985 (2002).

[7] R. Bergmann, E. de Jong, J. B. Choimet, D. van der Meer, and D. Lohse, *The origin of the tubular jet*, J. Fluid Mech. **600**, 19–43 (2008).

[8] S. Gekle, J. M. Gordillo, D. van der Meer, and D. Lohse, *High-Speed Jet Formation after Solid Object Impact*, Phys. Rev. Lett. **102**, 034502 (2009).

[9] J. E. Hogrefe, N. L. Peffley, C. L. Goodridge, W. T. Shi, H. G. E. Hentschel, and D. P. Lathrop, *Power-law singularities in gravity-capillary waves*, Physica D **123**, 183–205 (1998).

[10] M. S. Longuet-Higgins and H. Oguz, *Critical microjets in collapsing cavities*, J. Fluid Mech. **290**, 183–201 (1995).

[11] R. Bergmann, D. van der Meer, M. Stijnman, M. Sandtke, A. Prosperetti, and D. Lohse, *Giant Bubble Pinch-Off*, Phys. Rev. Lett. **96**, 154505 (2006).

[12] M. S. Longuet-Higgins, *Bubbles, breaking waves and hyperbolic jets at a free surface*, J. Fluid Mech. **127**, 103–121 (1983).

[13] H. N. Oguz and A. Prosperetti, *Dynamics of bubble growth and detachment from a needle*, J. Fluid Mech. **257**, 111–145 (1993).

[14] R. Bergmann, D. van der Meer, S. Gekle, A. van der Bos, and D. Lohse, *Controlled impact of a disk on a water surface: cavity dynamics*, J. Fluid Mech. **633**, 381–409 (2009).

[15] S. Gekle and J. M. Gordillo, *Compressible air flow through a collapsing liquid cavity*, Int. J. Numer. Meth. Fluids (2010).

[16] S. Gekle and J. M. Gordillo, *Generation and breakup of Worthington jets after cavity collapse. Part 1. Jet formation*, J. Fluid Mech. **663**, 293–330 (2010).

[17] H. N. Oguz and A. Prosperetti, *Bubble entrainment by the impact of drops on liquid surfaces*, J. Fluid Mech. **219**, 143–179 (1990).

[18] O. V. Voinov, *Hydrodynamics of wetting*, Fluid Dynamics **11**, 714–721 (1976).

[19] E. Ory, H. Yuan, A. Prosperetti, S. Popinet, and S. Zaleski, *Growth and collapse of a vapor bubble in a narrow tube*, Phys. Fluids **12**, 1268–1277 (2000).

[20] C. Sun, E. Can, R. Dijking, D. Lohse, and A. Prosperetti, *Growth and collapse of a vapour bubble in a mictotube: the role of thermal effects*, J. Fluid Mech. **632**, 5–16 (2009).

[21] J. R. Blake and D. C. Gibson, *Growth and collapse of a vapour cavity near a free surface*, J. Fluid Mech. **111**, 123–140 (1981).

[22] O. Lindau and W. Lauterborn, *Cinematographic observation of the collapse and rebound of a laser-produced cavitation bubble near a wall*, J. Fluid Mech. **479**, 327–348 (2003).

[23] J. Eggers and E. Villermaux, *Physics of liquid jets*, Rep. Prog. Phys. **71**, 036601 (2008).

8

Coexistence of Two Singularities in Dewetting Flows: Regularizing the Corner Tip *

Entrainment in wetting and dewetting flows often occurs through the formation of a corner with a very sharp tip. This corner singularity comes on top of the divergence of viscous stress near the contact line, which is only regularized at molecular scales. We investigate the fine structure of corners appearing at the rear of sliding drops. Experiments reveal a sudden decrease of tip radius, down to 20 microns, before entrainment occurs. We propose a lubrication model for this phenomenon, which compares well to experiments. Despite the disparity of length scales, it turns out that the tip size is set by the classical viscous singularity, for which we deduce a nanometric length from our macroscopic measurements.

8.1 Introduction

Fluid interfaces can be deformed into singular structures exhibiting length scales much smaller than that of the global flow. The most common example is a water drop detaching from a faucet, developing a singularity at pinch-off [1, 2]. Similar topological changes occur when the flow near the interface is driven so strongly that

*Published as: Ivo Peters, Jacco H. Snoeijer, Adrian Daerr, and Laurent Limat, *Coexistence of Two Singularities in Dewetting Flows: Regularizing the Corner Tip*, Phys. Rev. Letters. **103**, 114501 (2009)

one of the fluid phases can invade the other. This so-called entrainment often occurs through a sharp cusp or tip [3–7], as is e.g. observed for air bubbles entrained by a jet or solid plunging into a liquid pool [8–12]. However, below the critical driving strength the interface remains at steady state and a stationary, singular structure is formed. Besides fundamental interest, this control over small length scales is crucial in applications such as spray formation and inkjet printing [13, 14], while entrainment is rate limiting in coating [15].

A peculiar situation arises in wetting flows, when the liquid is bounded by a corner-shaped contact line [8–10, 16–18], cf. Fig. 8.1(*b*). Above a critical speed the sharp corner tip breaks up to entrain bubbles or droplets depending on whether the contact line is advancing or receding. This corner singularity emerges on top of the famous moving contact line singularity: even a perfectly straight contact line develops diverging viscous stress when maintaining a no-slip boundary condition down to molecular scale [19, 20]. Despite progress on the flow away from the tip [21, 22], it has remained unclear how these two singularities can coexist, whether they are related and what determines the sharpness of the corner tip [17].

In this chapter we investigate the fine structure of corner tips appearing at the rear of drops sliding down an inclined plane (Fig. 8.1). The steady-state corners are characterized by the tip radius R, which close to the entrainment threshold is found to decrease dramatically with drop speed U. Using a lubrication model we derive the approximate relation

$$R = \ell\, e^{\theta_e^3/9Ca}, \tag{8.1}$$

that accurately describes the experimental observations. Here θ_e is the equilibrium (receding) contact angle and the speed dependence appears through the capillary number $Ca = U\eta/\gamma$, where η and γ denote viscosity and surface tension. We identify the length ℓ as the molecular scale associated with the microscopic physics of wetting [23–31]. We obtain a length of the order of 10 nm by fitting the experimental data. From a hydrodynamic point of view, this is the scale at which the classical viscous singularity is regularized.

Dewetting corners thus have the remarkable feature that the tip size is governed by an *inner* length scale ℓ, much smaller than the tip radius itself. This scenario is very different from free surface singularities without a contact line, even though these can exhibit a similar exponentially decreasing tip size. For example, the cusp solution by Jeong & Moffat [3] scales as $R_{\mathrm{cusp}} \sim Le^{-Ca}$, but in this case L is an *outer* length scale characterizing the macroscopic flow.

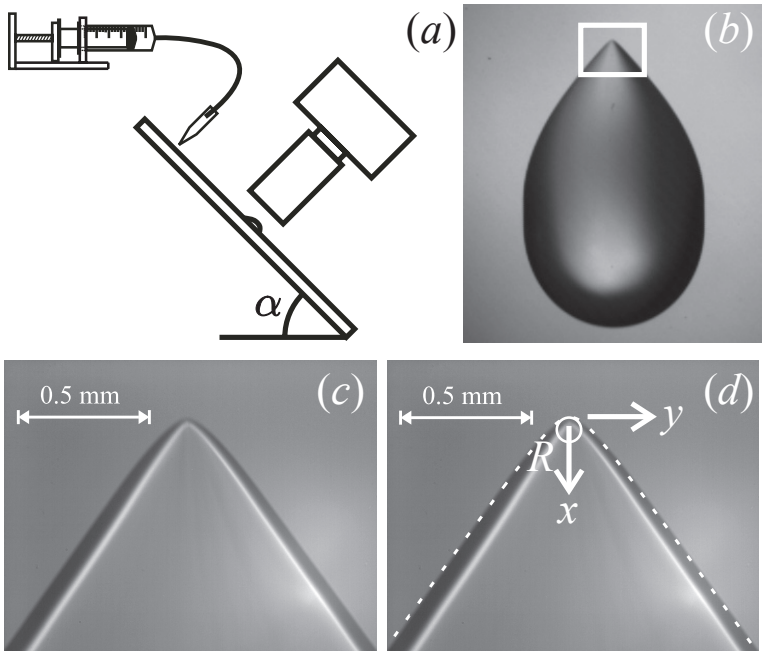

Figure 8.1: (a) Sketch of the experimental setup. Partially wetting silicone oil drops slide down an inclined plane with constant velocity. (b) The interface shape of the drop is monitored from above for different sliding velocities. At large speeds a sharp corner forms at the rear of the drop. (c) The tip radius R can be determined from a zoom of the corner tip. (d) Same as in (c) showing that the contact line is well approximated by a hyperbolic shape (dashed, using $R = 50$ μm).

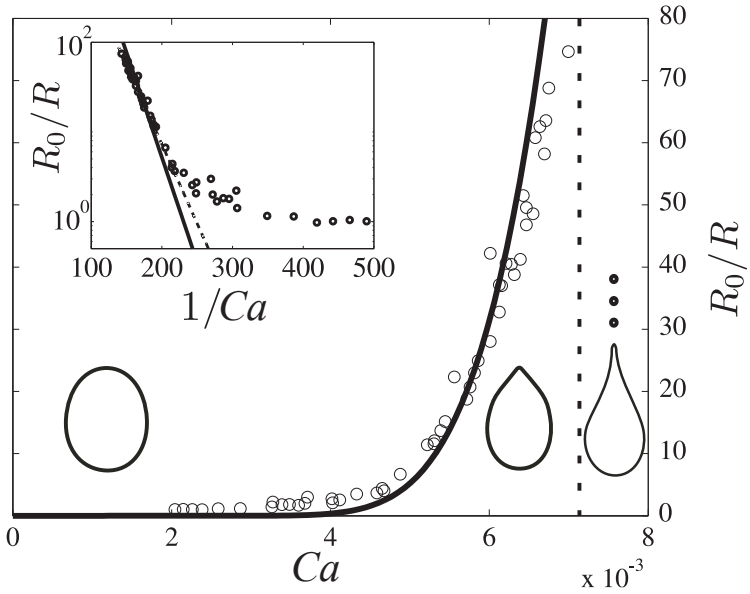

Figure 8.2: Experimental measurements of the tip curvature $1/R$ as a function of Ca. Data are normalized by the contact line radius at zero speed, $R_0 = 1.63$ mm. At low $Ca$the curvature stays nearly constant $R/R_0 \approx 1$, while close to the pearling transition (vertical dashed line) the curvature increases nearly two orders of magnitude. Solid line indicates the prediction (8.1) with $\ell = 7$ nm. Inset: The logarithmic plot confirms the predicted scaling. Dashed line is the best linear fit.

8.2 Experiments

A schematic view of the experimental setup is given in Fig. 8.1(a). Silicon oil drops are deposited on an inclined glass plate ($\eta = 18.6$ cP, $\gamma = 0.0205$ N/m, $\rho = 940$ kg/m^3). The drops detach from a pipette connected to a syringe pump, resulting in a constant drop volume (typically $8-10$ mm^3). The drops slide down at a constant speed U that is controlled by the angle at which the plate is inclined. The glass plate is coated with fluoro-polymers (FC725), providing partial wetting conditions for silicon oil [16] with static advancing and receding angles of 55° and 45° respectively. As we consider the receding contact line at the rear of the drop we take $\theta_e = 45°$. The corners are visualized with large magnification that is achieved by using a 25 mm Pentax lens in reversed direction combined with several macro extension tubes. The optical resolution of the images like Fig. 8.1(c) on which the actual tip curvature measurements are done is 2 μm/pixel on a 1 megapixel image.

Figure 8.2 shows experimental results on the contact line curvature $1/R$ as a function of drop speed Ca. Tip radii are normalized by the radius of curvature of

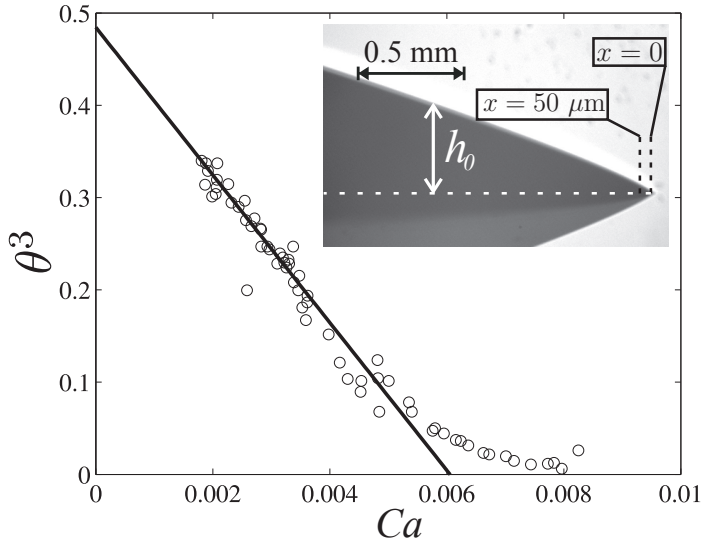

Figure 8.3: The receding contact angle θ measured at a fixed distance $x = 50$ μm. A linear fit is made to the Cox-Voinov regime (solid line). A clear departure from the linear regime sets in at $Ca \approx 6 \cdot 10^{-3}$, where R approaches the measurement scale of 50 μm. Inset: A side view of the rear of a drop sliding from right to left. h_0 is the height of the drop along the centerline.

a static drop of the same volume, $R_0 = 1.63$ mm. At low speeds the curvature remains constant, while a rapid increase of the curvature can be seen at capillary numbers $Ca \gtrsim 5 \cdot 10^{-3}$. This behavior coincides with the onset of the cornered shape. The measurements continue up to the "pearling transition" at which small droplets are entrained, occurring around $Ca = 7 \cdot 10^{-3}$. The smallest tip size we find before this entrainment is approximately 20 μm, which is nearly two orders of magnitude smaller than the global drop size. The scaling (8.1) is revealed in the inset of Fig. 8.2, showing the curvature $1/R$ on a semi-logarithmic scale versus $1/Ca$. In the corner regime the data agree very well with this exponential behavior. The solid line was fitted using the length scale ℓ as the sole adjustable parameter, yielding $\ell = 7$ nm. We wish to emphasize, however, that the determination of ℓ is very sensitive to the details of the fit. For example, when fitting (8.1) using θ_e as second adjustable parameter one finds $\theta_e = 41^\circ$ and $\ell = 65$ nm (dashed line). We nevertheless conclude that the length scale is of nanometric size, consistent with the typical size of silicone oil molecules [17].

We now wish to demonstrate that ℓ is related to the regularization of the viscous singularity that appears in the Cox-Voinov law for the dynamic contact angle θ [23]

$$\theta^3 = \theta_e^3 - 9Ca \ln \frac{x}{\ell_\theta}, \tag{8.2}$$

which is accurate within 2% for angles up to 45° [24]. This dynamic angle varies logarithmically with the distance to the contact line x, cut-off at a scale ℓ_θ. The precise interpretation of this length depends on the physics at molecular scale, which goes beyond hydrodynamics and beyond the purpose of the present paper [23–31]. Here we estimate ℓ_θ by measuring the contact angle along the central axis of the drop, very near the tip, from side view images at different speeds (cf. inset of Fig. 8.3). Strictly speaking, (8.2) is derived for straight contact lines. We therefore perform our measurements at a distance $\ll R$, where the effect of contact line curvature should be negligible. Given the resolution of the side view images, we take $x = 50$ μm in order to have sufficient accuracy on the contact angle.

Figure 8.3 shows θ^3 versus Ca. We clearly distinguish the linear regime of (8.2), as well as a departure from this behavior at higher drop speeds. From a linear fit we recover the (receding) equilibrium angle $\theta_e = 45 \pm 1^\circ$ as well as $\ell_\theta = 8 \pm 5$ nm. This length scale is consistent with the order of magnitude found from the R measurements. The deviation from the Cox-Voinov behavior occurs when the radius of curvature approaches the measurement scale of 50 μm, around $Ca \approx 6 \cdot 10^{-3}$. This once more suggests an interaction between R and ℓ_θ in the corner regime.

8.3 Lubrication model

We interpret these findings within a lubrication model that incorporates the strongly curved tip. For small contact angles the shape of the liquid-gas interface, $h(x,y)$, obeys a partial differential equation that expresses a balance between capillary and viscous forces [32]. The multi-scale nature of the problem makes it difficult to solve the equation by direct simulation. Instead, we propose an approximate analysis that has the additional advantage of yielding expressions in closed form. First, we assume that the flow is oriented purely in the x direction (Fig. 8.4, inset), so that the lubrication equation simplifies

$$\partial_x \kappa = \frac{3Ca}{h^2}. \tag{8.3}$$

κ is the interface curvature providing the Laplace pressure $p = -\gamma\kappa$. For sharp corners with vanishing tip size, this "planar flow approximation" was found very accurate [21]. In the present case this corresponds to $x \gg R$. For $x \ll R$ the flow becomes truly one-dimensional since $\partial/\partial_y \ll \partial/\partial_x$ and (8.3) is even exact. In this region $\kappa = \partial_{xx} h$, and (8.3) can be integrated to the Cox-Voinov law [23, 24, 33]. For corners such as in Fig. 8.1 we thus expect to recover (8.2) at small distance from the tip.

Away from the tip, $x \sim R$, the interface exhibits a truly two-dimensional structure, $\kappa = \partial_{xx} h + \partial_{yy} h$, making the analysis much more involved. This effect has been considered in the limit of weak contact line curvature [34], but this is not sufficient for the present purpose. To make progress we estimate κ by *(i)* approximating the contact line shape by a hyperbola, $y_{\mathrm{cl}}^2 = 2Rx + \phi^2 x^2$, and *(ii)* approximating the cross-section of the corner by a parabola. The quality of the former approximation can be inferred from the dashed line of Fig. 8.1(*d*), while the latter has been justified in detail in [21]. With this, the interface is parameterized as (cf. inset Fig. 8.4)

$$h(x,y) = h_0(x)\left(1 - \frac{y^2}{y_{\mathrm{cl}}^2}\right), \tag{8.4}$$

containing R and ϕ, the opening angle of the hyperbola, as parameters. In addition, we still need to solve the centerline profile $h_0(x)$. To close the problem we evaluate the curvature at the centerline $y = 0$,

$$\kappa = h_0'' - \frac{2h_0}{2Rx + \phi^2 x^2}, \tag{8.5}$$

which together with (8.3) provides an ordinary differential equation for $h_0(x)$. This equation was previously studied with vanishing tip radius $R = 0$ [21, 22], here representing the limit $x \gg R$. This regime admits solutions with a well-defined corner angle $h_0'(\infty) = \Omega = (3Ca\phi^2/2)^{1/3}$, obtained by combining (8.3) and (8.5).

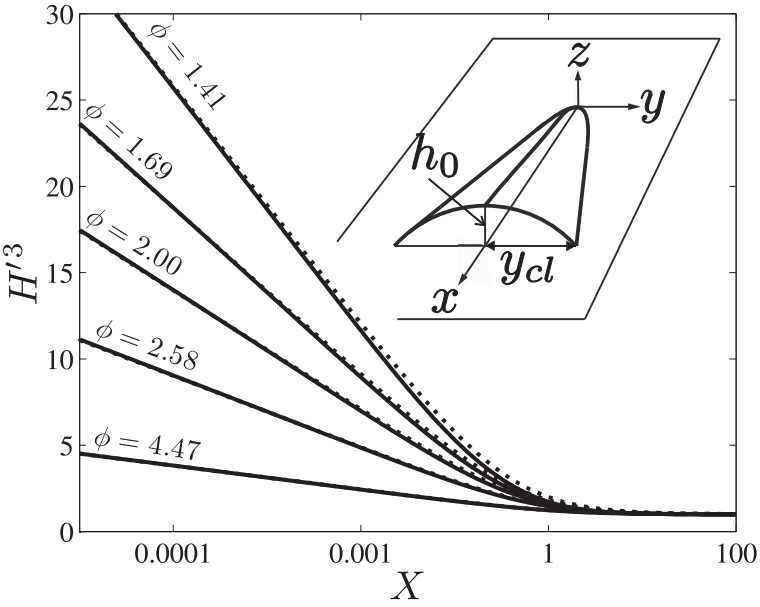

Figure 8.4: Rescaled slope H'^3 obtained from numerical solution of (8.6) with boundary conditions $H'(\infty) = 1$, $H(0) = 0$ (solid lines). The Cox-Voinov logarithmic variation saturates at a distance $X \sim 1$, corresponding to the tip radius. Dotted lines represent (8.7) using β as fit parameter. Inset: the drop shape is modeled by a hyperbolic contact line shape $y_{\mathrm{cl}}(x)$ and parabolic cross section. The centerline profile $h_0(x)$ can then be computed from (8.6).

It is convenient to introduce dimensionless variables $X = x\phi^2/R$ and $H = h_0\phi^2/R\Omega$, so that from (8.3) and (8.5) we obtain the equation on the centerline

$$\frac{\phi^2}{2}H''' - \left(\frac{H}{X(X+2)}\right)' = \frac{1}{H^2}. \tag{8.6}$$

The only remaining parameter is the opening angle ϕ[†]. We have the asymptotic boundary conditions $H'(\infty) \to 1$ (corner solution) and $H(0) \to 0$ towards the contact line. Figure 8.4 displays the solutions obtained from numerical integration, for various ϕ. At small X one recovers the Cox-Voinov logarithmic variation of the slope H', showing up as a straight line on this plot. However, this trend saturates at large X, when the two-dimensional nature of the curvature becomes apparent. All solutions are very accurately represented by the form

$$H'^3 = 1 + \frac{6}{\phi^2}\ln\left(1 + \frac{\beta}{X}\right), \tag{8.7}$$

as can be seen from Fig. 8.4 (dotted lines). We used β as a fit parameter that turns out to depend weakly on ϕ. A perturbation expansion shows that (8.7) is in fact the exact solution for $\phi \gg 1$, with $\beta = 2$.

To solve for the tip radius, the final step is to match (8.2) to the small scale asymptote of (8.7), which in original variables reads $h'^3 \simeq \Omega^3 + 9Ca\ln\frac{\beta R}{x\phi^2}$. Equating the two expressions one finds

$$\Omega^3 = \theta_e^3 - 9Ca\ln\frac{\beta R}{\phi^2\ell_\theta}, \tag{8.8}$$

which is the sought for relation between R, $Ca$and the contact angles. Since in practice $\Omega \ll \theta_e$, it can be recast as (8.1) with $\ell = \ell_\theta\phi^2/\beta$. Strictly speaking this length contains a dependence on drop speed through the opening angle ϕ that also induces a variation of β. This variation, however, is subdominant with respect to the exponential dependence in (8.1).

Let us emphasize that the structure (8.7) is robust with respect to the choice of parametrization of the interface shape and the "planar flow approximation", since these only affect the cross-over to the corner regime. On the other hand, the numerical value of β is determined from the second term in (8.5) and will certainly be model dependent. One should bear in mind that these details fall within the experimental uncertainty on ℓ and ℓ_θ.

[†]Experimentally, the angle ϕ decreases with drop speed, in order to reduce the normal velocity of the inclined contact lines [16, 17]; its value remains of order unity.

8.4 Conclusions and outlook

We have identified a new kind of singularity in free surface flows for which the regularization involves a microscopic (inner) scale instead of a macroscopic (outer) scale. In fact, the corner is obtained by sharply bending the line singularity associated to the viscous divergence near the contact line. This is very specific for wetting flows and differs qualitatively from other free surface singularities. Our findings also emphasize that the dynamic contact angle is strongly affected by the corner. This gives a departure of the Cox-Voinov behavior when the tip size becomes comparable to the scale of measurement. It would be interesting to compare these results to advancing contact lines, where bubble entrainment occurs through sharp corners as well [8–10].

In the experiment, the minimum tip size that can be achieved is limited by the onset of the pearling instability. This instability can possibly be incorporated in the model by matching the cross sections to the inclined contact lines, along the lines of Ref. [22]. In that study, however, the tip radius was neglected and incorrectly predicted a vanishing size of emitted drops at threshold. In practice these drops are of the order of 100 μm, which we speculate to be related to the finite radius of the tip.

References

[1] J. Eggers, *Nonlinear dynamics and breakup of free-surface flows*, Rev. Mod. Phys. **69**, 865–930 (1997).

[2] R. F. Day, E. J. Hinch, and J. R. Lister, *Self-Similar Capillary Pinchoff of an Inviscid Fluid*, Phys. Rev. Lett. **80**, 704–707 (1998).

[3] J.-T. Jeong and H. K. Moffatt, *Free-surface cusps associated with flow at low Reynolds number*, J. Fluid Mech. **241**, 1–22 (1992).

[4] J. Eggers, *Air Entrainment through Free-Surface Cusps*, Phys. Rev. Lett. **86**, 4290–4293 (2001).

[5] I. Cohen and S. R. Nagel, *Scaling at the Selective Withdrawal Transition through a Tube Suspended above the Fluid Surface*, Phys. Rev. Lett. **88**, 074501 (2002).

[6] W. W. Zhang, *Viscous Entrainment from a Nozzle: Singular Liquid Spouts*, Phys. Rev. Lett. **93**, 184502 (2004).

[7] S. Courrech du Pont and J. Eggers, *Sink Flow Deforms the Interface Between a Viscous Liquid and Air into a Tip Singularity*, Phys. Rev. Lett. **96**, 034501 (2005).

[8] R. Burley and B. S. Kennedy, *An experimental study of air entrainment at a solid/liquid/gas interface*, Chem. Eng. Sci. **31**, 901–911 (1976).

[9] T. D. Blake and K. J. Ruschak, *A maximum speed of wetting*, Nature **282**, 489–491 (1979).

[10] H. Benkreira and M. I. Khan, *Air entrainment in dip coating under reduced air pressures*, Chem. Eng. Sci. **63**, 448–459 (2008).

[11] E. Lorenceau, D. Quéré, and J. Eggers, *Air Entrainment by a Viscous Jet Plunging into a Bath*, Phys. Rev. Lett **93**, 254501 (2004).

[12] E. Lorenceau, F. Restagno, and D. Quéré, *Fracture of a Viscous Liquid*, Phys. Rev. Lett **90**, 184501 (2003).

[13] A. M. Gañán-Calvo, *Cone-Jet Analytical Extension of Taylor's Electrostatic Solution and the Asymptotic Universal Scaling Laws in Electrospraying*, Phys. Rev. Lett **79**, 217–220 (1997).

[14] J. Eggers and E. Villermaux, *Physics of liquid jets*, Rep. Prog. Phys. **71**, 036601 (2008).

[15] S. Kistler and P. Schweizer, *Liquid Film CoatingScientific Principles and Their Technological Implications*, volume 169 (Kluwer Academic) (1997).

[16] T. Podgorski, J.-M. Flesselles, and L. Limat, *Corners, Cusps, and Pearls in Running Drops*, Phys. Rev. Lett. **87**, 036102 (2001).

[17] N. Le Grand, A. Daerr, and L. Limat, *Shape and motion of drops sliding down an inclined plane*, J. Fluid Mech. **541**, 293–315 (2005).

[18] C. Duez, C. Ybert, C. Clanet, and L. Bocquet, *Making a splash with water repellency*, Nature Phys. **3**, 180–183 (2007).

[19] C. Huh and L. E. Scriven, *Hydrodynamic model of steady movement of a solid/liquid/fluid contact line*, J. Colloid Interface Sci. **35**, 85–101 (1971).

[20] E. B. Dussan V and S. H. Davis, *On the motion of a fluid-fluid interface along a solid surface*, J. Fluid Mech. **65**, 71–95 (1974).

[21] L. Limat and H. A. Stone, *Three-dimensional lubrication model of a contact line corner singularity*, Europhys. Lett. **65**, 365 (2004).

[22] J. H. Snoeijer, N. Le Grand-Piteira, L. Limat, H. A. Stone, and J. Eggers, *Cornered drops and rivulets*, Phys. Fluids **19**, 042104 (2007).

[23] O. V. Voinov, *Hydrodynamics of wetting*, Fluid Dyn. **11**, 714–721 (1976).

[24] R. G. Cox, *The dynamics of the spreading of liquids on a solid surface. Part 1. Viscous flow*, J. Fluid Mech. **168**, 169–194 (1986).

[25] P. G. de Gennes, *Deposition of Langmuir-Blodgett layers*, Colloid Polym. Sci. **264**, 463–465 (1986).

[26] Y. Pomeau, *Reaction diffusion in fast steady flow*, C. R. Acad. Sci., Ser. IIb: Mech., Phys., Astron. **328**, 255–262 (2000).

[27] J. Eggers, *Hydrodynamic Theory of Forced Dewetting*, Phys. Rev. Lett. **93**, 094502 (2004).

[28] U. Thiele, K. John, and M. Bär, *Dynamical Model for Chemically Driven Running Droplets*, Phys. Rev. Lett. **93**, 027802 (2004).

[29] L. W. Schwartz, D. Roux, and J. J. Cooper-White, *On the shapes of droplets that are sliding on a vertical wall*, Physica D: Nonlinear Phenomena **209**, 236–244 (2005).

[30] E. Rolley and C. Guthman, *Dynamics and Hysteresis of the Contact Line between Liquid Hydrogen and Cesium Substrates*, Phys. Rev. Lett. **98**, 166105 (2007).

[31] J. De Coninck and T. D. Blake, *Wetting and Molecular Dynamics Simulations of Simple Liquids*, Ann. Rev. Mater. Res. **38**, 1–22 (2008).

[32] A. Oron, S. H. Davis, and S. G. Bankoff, *Long-scale evolution of thin liquid films*, Rev. Mod. Phys. **69**, 931–980 (1997).

[33] B. R. Duffy and S. K. Wilson, *A third-order differential equation arising in thin-film flows and relevant to Tanner's Law*, Appl. Math. Lett. **10**, 63–68 (1997).

[34] J. H. Snoeijer, E. Rio, N. Le Grand, and L. Limat, *Self-similar flow and contact line geometry at the rear of cornered drops*, Phys. Fluids **17**, 072101 (2005).

9 Conclusions and Outlook

In this thesis a wide variety of free surface flow focusing experiments have been investigated. The free surface has acted either as a boundary to focus a gas flow, has been the subject of flow focusing due to its shape, or a combination of both. For each chapter, we summarize here the main conclusions, followed by suggestions for further research.

In Chapter 2 and Chapter 3 we have investigated the air flow inside a collapsing cavity created by disc impact on a water surface. We have used two different experimental methods to determine the air flow. We combined the advantages of both which together with numerical simulation provided valuable information. The first experimental method that we employed was measuring the volume of the cavity. The main advantage of this method is that the cavity volume is experimentally easy accessible, and that it can be applied during the full experiment from the moment of impact until the collapse. The disadvantage is that we can only indirectly measure the air flow, which means that we have to assume a simple one-dimensional flow structure, and we can only calculate the air velocity if compressibility can be neglected. Our second experimental method relies on flow visualization by laser-sheet illumination of smoke particles inside the cavity, from which we were able to directly measure the velocity of the air. Although the latter method is not reliable close to the pinch-off, it does show that for moderate velocities of the air, the indirect volume method can be used. For higher velocities we used numerical simulations in three settings: (i) a single incompressible phase, (ii) two-phase with incompressible gas, and (iii) two-phase with compressible gas. By comparing these three different simulations with the experimental results, we showed that to fully describe the dynamic shape of the cavity

compressibility of the air needs to be taken into account. A striking consequence of the compressibility is that the air obtains supersonic speeds and a shock in the neck region develops just before the pinch-off.

We have shown that the air plays an important role in the collapse of a cavity close to the moment of pinch-off by comparing experiments with simulations. It would however also be possible to show the influence of air by experiments only. For this, experiments could be done under reduced or increased air pressure, or using a heavier gas (for example SF_6). This should have a pronounced effect on the evolution of the cavity volume when the moment of pinch-off is approached.

With regard to the jet formation right after the pinch-off, it would be very interesting to find out if the jet is influenced by the air flow. Especially the initial part of the jet can be rather irregular and behaves more like a spray of small droplets than like a coherent jet, which might be due to large air velocities. This effect would also be more visible at higher air pressures or using a heavier gas.

In Chapter 4 we have performed an experimental study of the collapse of non-axisymmetric cavities. We have provided convincing experimental evidence for the oscillations at a wide range of mode numbers that were predicted by the theory of Schmidt *et al.* [1]. In the linear regime there is excellent agreement between the experiments and the theory. We have pushed the non-axisymmetric perturbations far beyond the linear regime by increasing the amplitude, which resulted in a wide variety of complex shapes.

The non-linear phenomena in non-axisymmetric collapses have very recently been studied numerically by Lai [2] with a two-dimensional potential flow numerical scheme, which for some cases resulted in shapes very similar to the ones that we have found. Direct comparison to these simulations will provide better understanding of the mechanisms behind the complex observed behavior, and maybe tell whether a three-dimensional non-axisymmetric numerical simulation is needed to reproduce the shapes that we observed.

A regime that has not been covered experimentally is the collapse of cavities that have perturbations of multiple superimposed modes. This could also involve perturbations that are not rotationally symmetric.

In Chapter 5 we have used experiments, numerical simulations and theoretical analysis to better understand the formation of splashes and droplet ejection after disc impact. We have derived the existence of self-similar solutions for the shape of the splash for any value of the Weber number, which we confirmed with simulations and experiments. To elucidate the transition to droplet ejection from the splash, we determined the local Bond number at the tip of the splash to be of order unity at the transition. We showed that this condition for the transition to droplet ejection, related to the local Bond number, leads to a critical Weber number which we determined experimentally.

It remains unclear what sets the size of the ejected droplets. Possible explanations could be found in the initial size of the rim that develops around the disc. This initial (or minimum) size could be determined by the lubricating air layer between the disc and the water surface (this situation could be implemented in the boundary-integral simulations), the viscous boundary layer in the liquid close to the disc, or a combination of both.

A very fruitful combination would be to use discs with a very small amplitude perturbation (comparable to those used in Chapter 4) to see if there is a preferred mode number that decreases the critical Weber number the most. Finding a preferred mode number for the ejection of droplets may clarify the relation between the very regular pattern of droplets found after the drop impact on a shallow layer of liquid [3], and the more irregular droplet ejection after the impact of a circular disc. For this, one would need to find out what the best method is to make a fair comparison between different mode numbers. This could possibly be done by using the maximum curvature on the disc as a measure for the perturbation instead of the amplitude of the harmonic perturbation.

By impacting a disc on an oil layer floating on a water surface in Chapter 6, we have found experimental evidence for the jet model proposed by Gekle *et al.* [4]. We found that the jet is formed only from liquid on the surface of the collapsing cavity, and that there is no persisting stagnation point flow after the collapse. By starting the disc from an oil/water interface of two deep liquid layers, we found that universal profiles can be observed for large Froude numbers. We were able to show that deviations of the universal profiles depend on the effective Froude number Fr^*.

For the impact on a thin layer of oil, we observed capillary ripples on the cavity which are not observed in experiments without oil. The origin of these ripples can be investigated by changing experimental parameters like the oil layer thickness, impact speed, disc radius and viscosity of the oil. The experimental conditions are expected to have an influence on the moment of appearance, the wavelength, or amplitude of the capillary ripples, and shed more light on their origin.

The experiments where the disc is pulled down from the oil/water interface could be supplemented by experiments where the density difference is bigger. By making the density difference larger and larger, the shapes should eventually resemble again the cavity shapes that we find after the impact on a water surface with air. A possible method to understand the origin of the universal shapes can be to perform the experiment in the bulk of a water bath and generate a line of hydrogen bubbles parallel to the disc just before setting the disc in motion [5]. In that case the corrected Froude number is infinite by definition, regardless of how slow the disc is displaced. The shapes described by the hydrogen bubbles should then be compared to the universal shapes that we found. Since no significant dependence on density difference is found in our experiments, we expect those to be quite similar.

In Chapter 7 we numerically and theoretically investigated the formation of microjets. We found that after a short time, where compressibility of the liquid plays a role, the system can be described accurately using potential flow, considering the good agreement between the numerical simulations and the experiments. We found that the shape of the meniscus plays a key role by focusing the liquid into a thin jet. We developed a simple model that accurately predicts the velocity that the jet obtains due to the pressure impulse and the flow focusing.

In the experiments by Tagawa *et al.* [6], there is a strong dependence of the jet velocity on the tube radius. Using our boundary-integral simulations we have shown that the flow focusing is *not* responsible for this dependence in spite of the curvature of the meniscus, which does depend on the tube radius. The dependence found in the experiments probably is due to the volume that is exposed to the laser energy, but this needs to be investigated further.

More experimental research can be done to the initial stages right after the laser has fired, where compressibility is important. This includes visualization and determining the velocity of the shock wave in the capillary between the bubble and the free surface. Numerically, axisymmetric compressible simulations could be used and compared to experimental findings. This could lead to an explanation for the pressure gradient that ultimately develops and is responsible for accelerating the liquid between the bubble and the free surface.

In Chapter 8 we investigated the sharp corner that appears at the tail of a sliding droplet under partial wetting conditions. We experimentally find an exponential increase of the curvature at the tail for increasing sliding velocity. Using a lubrication approximation we show that the curvature of this corner depends on the molecular cutoff length, associated with the viscous singularity at the contact line of dewetting flows.

When the velocity of the droplet is increased further, the tail of the droplet becomes longer, leading eventually to the deposition of small droplets [7]. It remains however unclear which mechanism is responsible for the detachment of droplets from the tail of a sliding drop, and what sets the size of these droplets.

Our findings can be relevant in geometrical focusing of plasmas for nuclear fusion reactions. Since the highest energy density is achieved when a singularity is approached, it is desirable to focus a plasma into a single point. However, as we have shown in Chapter 4, especially in that case the development of asymmetries becomes very important. Instead of spherical focussing into a single point, it could also be possible to cylindrically focus a plasma into a line. One could intentionally impose asymmetries which would prevent the focusing into a single point, but could create singularities at multiple points around the center, which may lead to controlled jetting phenomena. The development of asymmetries is relevant for the gravitational collapse of stars, where material is accelerated towards the center of mass. Again, the

highest densities could be found outside the center of mass and jetting phenomena could become very important.

Knowledge about the formation of jets and the structures inside them, as we provided in Chapter 6, can be very useful in understanding stellar jets. Information about the origin of material that is found in these jets can tell more about the history of stellar systems that produce them: "But the structures of these jets are often too complex to determine which features arise at the source and which are the result of subsequent interactions with the surrounding gas." [8].

References

[1] L. E. Schmidt, N. C. Keim, W. W. Zhang, and S. R. Nagel, *Memory-encoding vibrations in a disconnecting air bubble*, Nature Phys. **5**, 343–346 (2009).

[2] L. Lai, *Curvature Singularity in the Asymmetric Breakup of an Underwater Air Bubble* 34 (2012), 1203.0014.

[3] L. V. Zhang, P. Brunet, J. Eggers, and R. D. Deegan, *Wavelength selection in the crown splash*, Phys. Fluids **22**, 122105 (2010).

[4] S. Gekle, J. H. Snoeijer, D. Lohse, and D. van der Meer, *Approach to universality in axisymmetric bubble pinch-off*, Phys. Rev. E **80**, 036305 (2009).

[5] Q.-X. Lian and Z. Huang, *Starting flow and structures of the starting vortex behind bluff bodies with sharp edges*, Exp. Fluids **8**, 95–103 (1989).

[6] Y. Tagawa, N. Oudalov, C. W. Visser, I. R. Peters, D. van der Meer, C. Sun, A. Prosperetti, and D. Lohse, *Highly focused supersonic microjets* (2012), 1112.2517.

[7] T. Podgorski, J.-M. Flesselles, and L. Limat, *Corners, Cusps, and Pearls in Running Drops*, Phys. Rev. Lett. **87**, 036102 (2001).

[8] H. Zinnecker, M. J. McCaughrean, and J. T. Rayner, *A symmetrically pulsed jet of gas from an invisible protostar in Orion.*, Nature **394**, 862–865 (1998).

Summary

Reaching a high energy density is of importance for many physical and chemical processes. An efficient way to generate high energy densities is to use a lower available energy density and to focus this into a small volume. In this thesis we investigate several experiments where focusing flows account for reaching higher energy densities.

In Chapter 2 and 3 we investigate the air flow induced by a collapsing cavity. We create a surface cavity by impacting a round disc onto a water surface at a constant speed. The downwards moving disc pushes the water outwards, while the hydrostatic pressure pushes the water back inwards. The cavity eventually closes at a single point (the *pinch-off*), after which two jets are formed: one shooting upwards, and one shooting downwards. During the closure of the cavity (before the pinch-off), air is pushed out of the bubble below the pinch-off depth. By combining several experimental techniques and numerical simulations we show that compressibility of the air becomes important close to the moment of pinch-off. The influence of the air has a pronounced effect on the evolution of the volume of the bubble as well as on the shape of the bubble. Moreover, we show that the air reaches supersonic speeds as it is flowing out of the cavity.

In Chapter 4 we use the same main experimental setup as in the previous two chapters; only we replace the round disc by one with non-axisymmetric perturbations (like the petals on a flower). In this experiment we precisely follow the evolution of the shape of the free surface on the inside of the cavity. Initially, very close to the disc, the water surface has the same shape as the disc (just as a round disc results in a cavity with a circular cross-section), but during the expansion and subsequent collapse, the cavity wall continuously changes its shape, in an oscillating manner. If the perturbation is small enough, we find an excellent agreement with theoretical predictions based on linear stability analysis. For larger perturbations, we observe spectacular non-linear effects like the formation of sub-cavities and sheet-like jets.

In Chapter 5 we return to the experiment with the round disc. We now however focus on the splash, the sheet of water that is thrown upwards right after the disc has hit the undisturbed water surface. At first, there is a very thin sheet surrounding the disc, which becomes thicker and higher as time progresses. We show that for any value of the Weber number the shape of this sheet can be described by scaling laws. By combining these scaling laws with experimental observations and numerical

simulations we show that the detachment of droplets from the sheet is a result of a Rayleigh-Taylor instability.

In Chapter 6 we add a new liquid to the experiment. We start with a layer of sunflower-oil floating on a water surface, and let the disc impact on this layer of oil. The experiment mainly evolves the same way as described in Chapter 2 and 3, except that the jet initially consists of only oil. Only at a later time the water joins into the jet. However, even at times at which the jet mainly consists of water, there always remains a stable core of oil in the center of the jet. This core extends all the way down into the bulk, past the point where the pinch-off initially took place. From the structure of the jet we are able to deduce how the jet is formed.

We perform a second set of experiments by preparing a deep layer of oil on top of the water surface and positioning the disc at the oil/water interface. When we then pull down the disc at a constant speed, a part of the oil is dragged down along with the disc. The entrained oil column obtains a specific shape which depends on the speed of the disc due to a competition between inertia and gravity: Due to the density difference, the oil is pushed upwards during the experiments. If the disc is moving fast enough we can neglect gravity, and the shape is determined by inertia only. We show that in this inertial regime the column shape becomes independent of the disc speed.

In Chapter 7 we investigate the formation of microjets using boundary-integral simulations. In the experiment, a jet is created by focusing a laser pulse inside a capillary, which is partially filled with a liquid. The laser pulse generates a vapor bubble which is accompanied by a pressure wave that travels through the capillary. The pressure wave reflects on the free surface and generates a fast microjet. Our numerical simulations accurately reproduce the shape and the evolution of the speed of these jets. We investigate how the curvature is responsible for increasing the speed and focusing the liquid into a symmetric jet. We use the insight obtained from the numerical simulations to construct a simple theoretical model that accurately predicts the speed of the jets.

In Chapter 8 we investigate silicone oil drops that are sliding down an inclined coated glass plate. The coating provides partial wetting conditions for the silicone oil. The shape of the droplets that are sliding down the plate depends on the sliding velocity of the drops. At very low speeds the drops remain nearly circular, but with increasing velocity a cornered tail is formed. A close look at the tail reveals that there never is a true corner, but there is always a finite radius of curvature. We experimentally show that the curvature at the tail increases exponentially with sliding speed. Using a lubrication approximation and matching the two-dimensional structure very close to the contact line to the three-dimensional structure of the tail further away from the contact line, we are able to give a theoretical explanation for the observed behavior.

Samenvatting

Het bereiken van een hoge energiedichtheid is een belangrijke voorwaarde voor veel fysische en chemische processen. Een efficiënte manier om hoge energiedichtheden te bereiken is om gebruik te maken van een reeds aanwezige lage energiedichtheid en deze vervolgens te concentreren in een klein volume. In dit proefschrift onderzoeken we diverse experimenten waarbij convergerende vloeistofstromingen zorgen voor hogere energiedichtheden.

In Hoofdstuk 2 en 3 onderzoeken we de luchtstroming die ontstaat tijdens het samenklappen van een luchtholte onder water. We creëren een luchtholte door een ronde metalen schijf met een diameter van enkele centimeters loodrecht op een wateroppervlak in te laten slaan. De schijf duwt het water naar buiten terwijl deze naar beneden beweegt, en de hydrostatische druk duwt het water vervolgens weer naar binnen. De holte sluit uiteindelijk in één enkel punt (de *pinch-off*), vanwaar vervolgens twee dunne vloeistofstralen (*jets*) wegschieten: één recht omhoog en één recht naar beneden, richting de schijf. Door gebruik te maken van een combinatie van verschillende experimentele technieken en numerieke simulaties tonen we aan dat de compressibiliteit van de lucht een belangrijke rol speelt vlak voor de pinch-off. Deze invloed van de lucht is terug te zien in zowel het volume als de vorm van de luchtholte. Daarnaast tonen we aan dat de lucht met supersone snelheid uit deze luchtholte stroomt.

In Hoofdstuk 4 voeren we hetzelfde experiment uit als in de twee voorgaande hoofdstukken, alleen vervangen we hier de ronde schijf door een schijf met niet-axisymmetrische verstoringen (vergelijkbaar met de blaadjes van een bloem). In dit experiment volgen we heel nauwkeurig de vorm van het wateroppervlak aan de binnenkant van de luchtholte. Vlak nadat het water door de schijf naar buiten wordt geduwd heeft het wateroppervlak bijna precies dezelfde vorm als de schijf (net zoals een ronde schijf een luchtholte met een cirkelvormige doorsnede veroorzaakt), maar tijdens het verder uitdijen en het daaropvolgende samenklappen verandert het wateroppervlak continu van vorm. Als de verstoring klein genoeg is vinden we een excellente overeenkomst met de voorspelling van een linear model. Voor grotere verstoringen observeren we spectaculaire niet-lineaire effecten zoals het afsnoeren van secundaire holtes en de vorming van plaatvormige jets die gelijkenis vertonen met de rugvin van een vis.

In Hoofdstuk 5 keren we weer terug naar het experiment met de ronde schijf. In dit geval kijken we echter niet naar de luchtholte die onder water ontstaat, maar naar de zogenoemde splash, de vloeistof die aan de rand van de schijf omhoog wordt geworpen op het moment dat de schijf het stilstaande wateroppervlak raakt. In eerste instantie beweegt het water als een dun gordijn rondom de schijf omhoog, maar al snel wordt het wateroppervlak steeds breder. We tonen aan dat de vorm van het wateroppervlak (het breder worden en omhoog bewegen) voor elke waarde van het Weber-getal beschreven wordt door een schalingswet. Door deze schalingswet te combineren met experimenten en numerieke simulaties hebben we aangetoond dat het loslaten van druppels aan de bovenrand van het watergordijn het gevolg is van een *Rayleigh-Taylor* instabiliteit.

In Hoofdstuk 6 voegen we een tweede vloeistof toe aan het experiment. We beginnen met een laag zonnebloemolie die drijft op het water, en we laten de schijf vanuit de lucht inslaan op deze olielaag. Het verloop van het experiment is in grote lijnen hetzelfde als beschreven in Hoofdstuk 2 en 3, alleen is er iets opvallends aan de jets die ontstaan: Het begin van de jet bestaat puur uit olie en pas op een later moment komt er ook water bij in de jet. Echter, zelfs op een tijdstip waarop de jet voor het grootste deel uit water bestaat vinden we in het midden van de jet een stabiele cylindervormige kern van olie. Deze cylinder van olie loopt vanuit de jet door naar beneden tot voorbij het punt waar de jet is ontstaan. Uit de samenstelling van de jet hebben we achterhaald hoe de jet precies gevormd wordt na de pinch-off.

In hetzelfde hoofdstuk voeren we een tweede set experimenten uit waarbij we een diepe laag olie op het water laten drijven, en we de schijf starten vanaf het scheidingsvlak tussen olie en water. De dikte van de laag olie is zo gekozen dat deze als oneindig dik kan worden beschouwd. Vervolgens trekken we de schijf met een constante snelheid naar beneden, waarbij de schijf een deel van de olie mee naar beneden het water in trekt. De vorm van de oliekolom die met de schijf naar beneden beweegt is afhankelijk van de snelheid van de schijf vanwege een competitie tussen de traagheid van de vloeistof en de zwaartekracht: Omdat de olie lichter is dan water zal de zwaartekracht ervoor zorgen dat de olie tijdens het experiment weer omhoog geduwd wordt. Echter, als we de schijf snel genoeg bewegen is de zwaartekracht verwaarloosbaar. We tonen aan dat bij deze hoge snelheden de vorm van de oliekolom niet meer afhankelijk is van de snelheid van de schijf.

In Hoofdstuk 7 onderzoeken we de vorming van een microscopische jet met behulp van numerieke simulaties. In experimenten wordt de jet gevormd door met een laser in een microscopisch dun buisje te schieten dat gedeeltelijk gevuld is met vloeistof. De laserpuls zorgt ervoor dat er een bel ontstaat in het buisje en, nog belangrijker, dat er een drukgolf door het buisje beweegt. Deze drukgolf reflecteert op het vrije oppervlak en geeft de vloeistof in een zeer korte tijd een hoge snelheid. Omdat het buisje heel dun is heeft het vloeistofoppervlak in het begin de vorm van een deel

van een perfecte bol. Het korte tijdsinterval waarin de vloeistof in beweging wordt gezet zorgt ervoor dat de vloeistof aan het oppervlak richting het middelpunt van deze (deels virtuele) bol beweegt. Deze convergerende stroming zorgt ervoor dat de snelheid nog hoger wordt en dat er een mooie axisymmetrische jet ontstaat. We simuleren dit proces numeriek met behulp van een *Boundary Integral* methode, en we vinden een perfecte overeenstemming met de experimenten. We gebruiken het inzicht dat we hebben verkregen uit de numerieke simulaties om een simpel theoretisch model op te stellen dat de snelheid van de jet goed kan voorspellen.

In Hoofdstuk 8 laten we druppels siliconenolie van een glazen plaat glijden. De glazen plaat heeft een coating die ervoor zorgt dat de druppel olie zich niet uitspreidt over de glazen plaat. Hierdoor glijden de druppels olie over de plaat op een vergelijkbare manier als druppels water die over een ruit glijden. De vorm van deze druppels is afhankelijk van de snelheid waarmee de druppels over de plaat glijden. Bij hele lage snelheden blijven de druppels vrijwel volledig rond, maar bij hogere snelheden krijgen de druppels een puntige staart. Als we deze puntige staart sterk vergroten zien we dat deze geen echte punt is, maar altijd een beetje rond blijft. Uit onze experimenten blijkt dat de kromming van de contactlijn in het puntje van de staart exponentieel toeneemt met de snelheid van de druppel. We verklaren dit verband met behulp van een lubricatie-benadering waarbij we de twee-dimensionale vorm van de druppel helemaal aan het tipje van de staart laten aansluiten aan de drie-dimensionale vorm van de staart verder weg van de punt.

Acknowledgements

Dear reader, we're almost there. I am certain that if you are reading this, you have carefully and critically read all the previous chapters, and maybe read some chapters even twice because you did not immediately understand every detail. Or, let's be a tiny bit more realistic: You quickly looked through this little book and maybe some nice pictures caught your attention. Whether it is the former or the latter, I first would like to thank you very much for showing interest in my work.

The work presented in this thesis is obviously something I could never do on my own. I would therefore like to thank all the people who contributed to this work.

I would like start by thanking my promotor Detlef for giving me the opportunity to work in this excellent research group, where anything you wish to do seems possible. This is for sure how good research is generated. Devaraj, as my direct supervisor you certainly have been the most important person for me during my work. Not only have you been able to patiently explain things I did not understand or came up with suggestions when we both did not understand what we were observing, you are also always able to improve anything that I write or present, from which I absolutely learned a lot.

I have had the privilege of working with many different people on different subjects. First I want to thank Stephan, especially your inclusion of a compressible gas phase in the boundary integral code has been and still is a valuable contribution. Oscar, you have done an amazing job as my master student: The pictures that we present Chapter 4 are becoming more and more famous; winning the Gallery of Fluid Motion twice and finally ending up on the cover of the Journal of Fluid Mechanics is quite amazing! This must have something to do with good artistic influence coming from Daniela. Laura, thanks to you we not only have nice pictures of non-axisymmetric cavities, but we even understand a lot of the things that we are seeing. My first numerical Boundary-Integral setup was the microjet, which benefited strongly from the comparisons to the experimental data and theoretical contributions from the "microjet-crew": Yoshi, Nikolai, Claas-Willem, Rory, Chao, and Andrea. Thank you all very much. Thanks to Gerben and Alexander for discussions and comparisons between your experiments and my simulations on the shock-tube jet. For the experiments with sunflower-oil I have to thank my bachelor student Matteo for exploring what is possible with this terribly messy experiment (imagine the "Ik zei

nog zo, geen bommetje!" scene with an oil-filled bath to get a rough idea). Jacco, thanks to you the sliding droplet experiments that I did during my internship in Paris have become worth much more. I am very grateful to Laurent and Adrian for what I have learned in less than four months in Paris. Koen, thanks for showing that the results from the sliding droplets are also useful for other setups and applications. I wish to thank Pascal, Diederik, Mathijs, and Michiel for performing some PIV experiments for the course Experimental Techniques without complaining too much that I had given them an impossible task which they had to finish within a week. Wilco, I believe you are a true and good successor as a BIM (Boundary-Integral-Man). As my master student I have the feeling that you have learned me more about the code than I have learned you, by asking me many critical questions and always finding something in the numerical results that may not be correct.

José, I remember the first time we were talking about the splash, and we agreed that it was a very difficult problem to solve. Looking back at it now, I think we have definitely proved that indeed it is a very difficult problem. Many Skype calls together with Devaraj (looking at a big question mark instead of your photograph "That stands for all the questions that I am unable to answer"), a visit to Sevilla and many e-mails later we still haven't answered all our questions, but thanks to your incredible drive we certainly have made a lot of progress.

Many thanks to Gert-Wim, Martin and Bas for fixing all kinds of problems with the setup and my computer. Joanita, I am sure that our group would not survive a single week if you weren't there to keep everything in order.

Not all our time at the Physics of Fluids group is spent on research; the other activities are varying from teaching to just having fun together. Teaching Heat and Mass Transfer was a lot of work, but together with Rory and Hanneke this task was made much lighter. Organizing the Primary School Days was a delight together with Dennis and Hanneke, thank you both. I want to thank my office mates Bram, Rajaram and Ceyda for all the small talks and discussions. I enjoyed all kinds of discussions during the coffee breaks with colleagues and the master students (especially the students from student room A always seem to have an enormous amount of fun). I had the pleasure of making music together with Dennis and Rodolfo, play indoor soccer matches thanks to the team captains Arjan and Stefan, play beach-volleyball, go swimming, watch movies, have dinners, and drink beers together.

Life does not end when you walk out of the world of fluid physicists. There are many people who don't know the least about the Navier Stokes equations, but who do mean the more to me.

Claudia, you have been in my life for a large part of my study and my PhD. We had a very good time together and I could always count on you, for which I want to thank you.

I would like to thank the friends I know from the MSG: Whether we are sitting

in the pouring rain or snow trying to keep warm near a campfire, or simply drinking beers in a bar, thanks to you it is always great fun. Many thanks to Anne, Ineke (thanks for designing the cover!), Albert, Vincent, Simon, Thea, Roger, Ellen, Liesbeth, Vincent, Anne, Niels, Iris, Egbert, Dimitri, and Saara-Maarit.

A special word for my dear friends Thijs, Bart, Sander, Mijke, and Natalie. Thijs and Bart, I could not imagine defending my thesis with more confidence than with you guys as my paranimfs.

I would never have gotten where I am now without the endless support of my parents Gonny and Guido and my sister Susan. Susan, I am very happy that you can be here in the Netherlands during my defence, before going back again surfing down under with Marc. Gonny and Guido, thanks to you your children will soon both be very far away. Not because they don't like you, but because you encouraged them to take opportunities when they occur. I could recommend a pair of parents like you to anyone!

Ivo Peters
Enschede, June 2012

About the author

Ivo Peters was born on Februari 10th, 1984 in Zevenaar, the Netherlands. He grew up in Ulft, and went to high school at the Isala College in Silvolde where he graduated in 2002. That same year he started his study Applied Physics at the University of Twente. He did a minor in Civil Engineering on the subject of Water Management. During his studies, he undertook a number of other activities, among other things playing guitar and being lead singer in the band W.I.T., playing drums in the band Agitated and participating in the boards of the thespian organization Nest and the motor sports organization MSG. He joined the study tour Ke Ji to China and did his internship in Paris at the Laboratoire Matière et Systèmes Complexes of the Université Paris 7 under the supervision of Laurent Limat. In 2008 he obtained his MSc. degree at the Physics of Fluids Group, after which he started his PhD research in the same group under the supervision of Devaraj van der Meer and Detlef Lohse.

Stellingen

Behorende bij het proefschrift van Ivo Peters

Free surface flow focusing

29 juni 2012

1. Om de vorm van een sluitende luchtholte aan een wateroppervlak correct te beschrijven moet er rekening worden gehouden met de compressibiliteit van lucht.
   Dit proefschrift, hoofdstuk 2

2. Het mechanisme waarmee de natuur het optreden van singulariteiten voorkomt, kan nog veel spectaculairder zijn dan de singulariteit zelf
   Dit proefschrift, hoofdstuk 3 en 4

3. Het wegschieten van druppeltjes na een plons is het gevolg van een Rayleigh-Taylor instabiliteit.
   Dit proefschrift, hoofdstuk 5

4. De hoge kwaliteit van de jets die met capillairen gemaakt kunnen worden, zijn te danken aan de perfectionist die door het leven gaat onder de naam Oppervlaktespanning.
   Dit proefschrift, hoofdstuk 7

5. Voor je gemoedsrust kun je zonnebloemolie beter alleen gebruiken bij het bakken van pannenkoeken.
   Dit proefschrift, hoofdstuk 6

6. Het altijd onverwachte gedrag van vloeistoffen zorgt voor vele frustraties tijdens het uitvoeren van experimenten. Dit weerspiegelt tegelijkertijd ook de rijkdom van dit fascinerende vakgebied.

7. "Target fixation" kan levensgevaarlijk zijn tijdens het motorrijden; kijk daarom nooit naar een boom als je iets te hard een bocht in gaat. In wetenschappelijk onderzoek hoef je hier niet voor te vrezen: hoe goed je je doel ook voor ogen hebt, je gaat waarschijnlijk toch een compleet andere richting op.

8. Het maken van een vergelijking is een sterk middel om iets ingewikkelds begrijpelijk uit te leggen, maar is juist ontzettend zwak als bewijsmiddel.

Propositions

Beloning to the thesis of Ivo Peters

Free surface flow focusing

June 29, 2012

1. In order to properly describe the shape of a closing surface cavity, the compressibility of the gas phase needs to be taken into account.
   This thesis, Chapter 2

2. The mechanisms by which nature prevents the occurrence of singularities are often even more spectacular than the singularity itself.
   This thesis, Chapter 3 and 4

3. The ejection of droplets after a splash is the result of a Rayleigh-Taylor instability.
   This thesis, Chapter 5

4. The high quality of the jets that can be produced from capillaries, are due to the perfectionist that we call Surface Tension.
   This thesis, Chapter 7

5. For one's peace of mind, one should exclusively restrict the use of sunflower oil for baking pancakes.
   This thesis, Chapter 6

6. The ever unexpected behavior of fluids is a source for many frustrations during experimental work. This however immediately reflects the richness of this fascinating field of research.

7. "Target fixation" can be extremely dangerous when riding a motorbike. Therefore one should never look to a tree in a fast corner. These risks are not to be feared in scientific research: no matter how well you fixate on your target, you are bound to end up going a completely different direction.

8. The use of comparisons is a powerful tool to explain difficult matter. It is however an extremely weak way to prove your point.